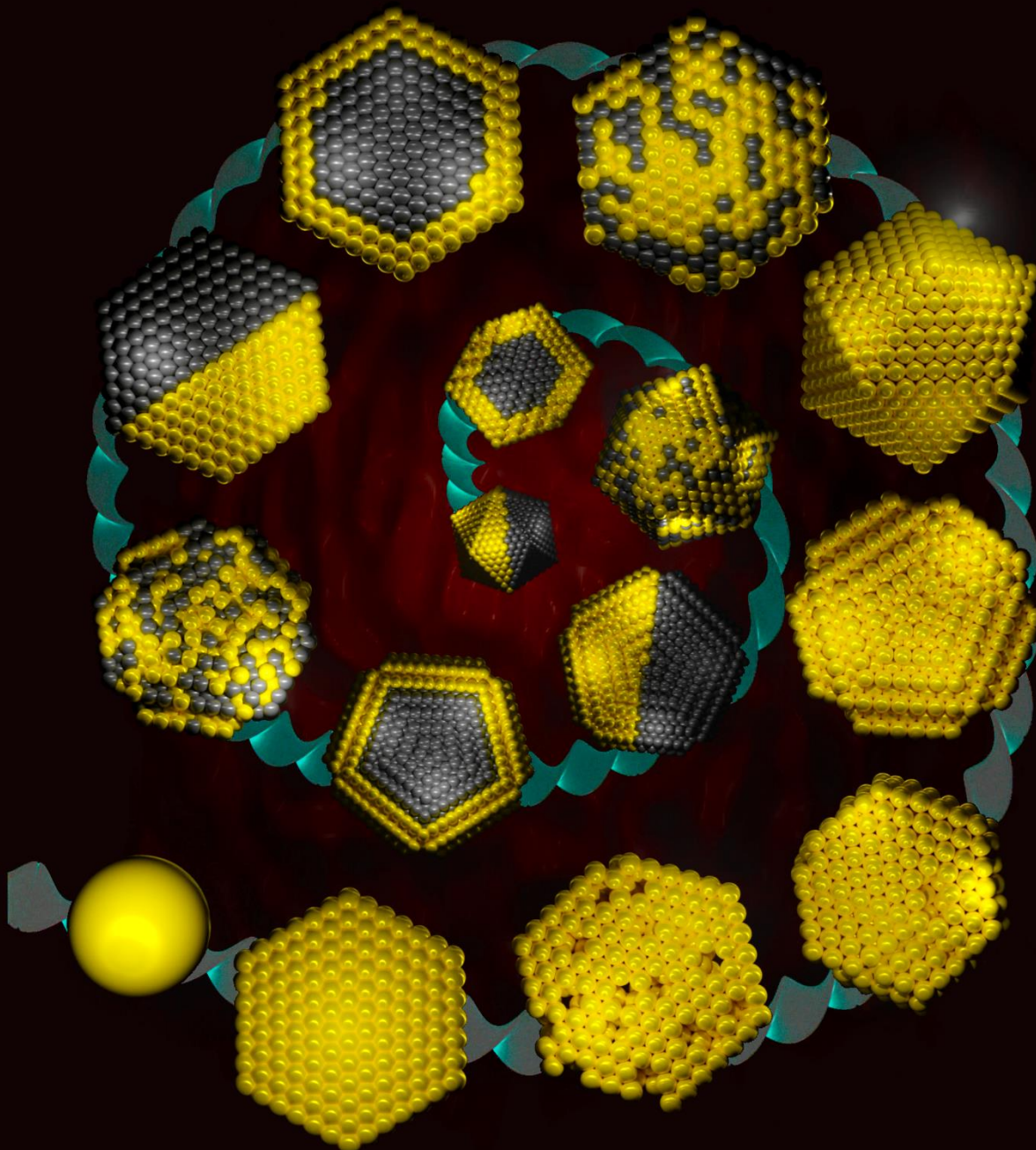


Morphology evolution in mono- and bimetallic FCC nanoparticles



ICChF

PhD Thesis

Ilia Smirnov



INSTITUTE OF PHYSICAL CHEMISTRY
POLISH ACADEMY OF SCIENCES

PhD Thesis

Morphology evolution in mono- and bimetallic FCC nanoparticles

Ilia Smirnov

Supervisor:
Prof. dr hab. Zbigniew Kaszukur

Doctoral dissertation prepared within International Doctoral Studies
of the Institute of Physical Chemistry Polish Academy of Sciences
Kasprzaka 44/52, 01-224 Warszawa, Poland

May 2023
WARSZAWA

Acknowledgments

The development of any project requires the efforts of many people playing their individual, irreplaceable roles. This holds true for my PhD studies as well. Throughout this journey, I have been fortunate to have the constant support and help from people around me. Their contributions have been invaluable, and I am pleased to report that their efforts were not in vain and led to the writing of this work.

I am deeply indebted to my Ph.D. supervisor Professor **Zbigniew Kaszkur**: It was an honor to be a part of our small, cozy group and work under your supervision! It would not be enough to acknowledge you for your guidance, teaching, patience, and support. I especially appreciate that you shared your passion for XRD, synchrotron radiation, computational simulation studies, and science in general with me. Thank you for your assistance with the many bureaucratic issues that constantly arose in my life. I will never forget our discussions, during which you acted as “The Devil's Advocate” to identify the weak points in our interpretations. Thank you for allowing me to work independently while always being close to assist and support me. Without you, this journey would not have been possible.

I want to express my appreciation to Dr. **Armin Hoell**: It was a pleasure to meet you at the Joint Polish-German Crystallographic Meeting 2020. I am grateful for your introduction and proposal of the tool that became crucial for my projects. Thanks to you, I discovered the synchrotron SAXS technique and had the great pleasure of visiting DESY. Our cooperation is especially important to me because it gave me a taste of international science. Even though our joint projects were not that big, they were one of the most essential parts of my academic life.

Special thanks to Ph.D. **Wojciech Juszczyk**: Thanks to you, I never had problems with the technical aspects of my experiments. Moreover, I always felt safe and confident that you would be there to help and settle any accidents or issues. I am deeply grateful for your patience and permanent comprehensive support!

I would like to express my deepest appreciation to Ph.D. **Maciej Zielinski**: Thank you for your assistance with programming, synthesis, fruitful discussions, sharing of samples, and maintaining order in the laboratory and its surroundings. I am grateful for all your valuable advice, and patient answers to my endless questions!

I am grateful to Ph.D. **Dmytro Lisovytskiy**: Thank you for your help with everyday matters in Poland, especially at the beginning of my Ph.D. studies, when I did not know Polish and bureaucrats did not know English. Additionally, I would like to express my appreciation for our fruitful conversations regarding XRD technique and our fun ping-pong matches.

Many thanks to Ph.D. **Bogusław Mierzwa**: A significant part of my thesis is based on the computational simulations performed using the Cluster program, which was essential to my research. I am grateful to you for creating and supporting Cluster software. Additionally, I would like to acknowledge your kind help and support in arranging my residence permit card during the beginning of my Ph.D. studies.

I would like to acknowledge Dr. **Silvio Haas** and Ph.D. **Marion Flatken** for their invaluable technical assistance and support during the synchrotron SAXS measurements at the P62 SAXSMAT beamline at DESY.

Finally, I would like to express my deepest and sincere appreciation to my lovely family: my wife and parents.

Dear **Katya**, I cannot express how much I am indebted to you. You have always shared with me all challenges of my Ph.D. life: low work-life balance, sleepless nights, low salary, and full self-dedication to work. I have been telling you about my research on the structure and properties of nanoparticles every day since the beginning of my Ph.D. (2016). Two years later, in 2018, you finally asked me, "What are nanoparticles?". After that question, I realized how comprehensive and absolute your support and love are. Thank you for being the source of my confidence and strength!

Dear **Natalia** and **Sergei Smirnov**, I don't know how to express my deepest and most sincere gratitude for all that you have done for me. My Ph.D. studies have been very challenging for our family. We have not seen each other in years, and our conversations have been limited to WhatsApp. However, despite the distance, I always felt that we were undertaking this journey together. You have been always aware of my scientific progress, including my articles, presentations, and posters, and shared in my struggles with thesis writing. You are familiar with all my colleagues and friends in Poland (in absentia). I'm incredibly grateful for everything you done for me!

Funding

This work was supported by:

- National Science Centre of Poland :
within the framework of OPUS 15 grant, no.: 2018/29/B/ST4/00710;
- Erasmus+ :
Mobility grant;
- The Deutsches Elektronen-Synchrotron (DESY) :
by granting the beamtime under proposal number: I-20210744 EC;
- European Synchrotron Radiation Facility (ESRF) :
by granting the beamtime under proposal number: HC-5301

Declaration of originality

I, **Ilia Smirnov**, hereby declare that the research included within this thesis was carried out by myself or with support by others included in acknowledgments.

I state that I have exercised care to ensure that the work is original and contains no previously published material or written by another person, except where citations have been made in the text.

To the best of my knowledge, the content provided here does not violate any copyrights.

I accept that the Polish Academy of Sciences has the right to use plagiarism detection software to ensure the thesis's legitimacy.

I certify that no part of my thesis has been or will be submitted for obtaining a degree or diploma by the Institute of Physical Chemistry, Polish Academy of Science, or any other educational institution.

This thesis's copyright rests with the author, and no information derived from it may be published without the author's consent.

Place, Date

Signature

List of publications

Publications related to the thesis:

- 1) **Smirnov Ilya**, Zbigniew Kaszukur, and Armin Hoell. "Development of nanoparticles bulk morphology analysis: Multidomain XRD approach." *Nanoscale* (2023). *Nanoscale* featured our research on the **Front cover**.
- 2) Kaszukur, Zbigniew, and **Ilya Smirnov**. "Nanopowder Diffraction." arXiv preprint arXiv:2212.06926 (2022).
- 3) **Ilya Smirnov**, Zbigniew Kaszukur, Armin Hoell, Maciej Jankowski. "Vacancies driven twinning in FCC metals: theory and experimental observation," *in preparation*.
- 4) **Ilya Smirnov**, Zbigniew Kaszukur, Armin Hoell. "Temperature-induced phase separation and segregation in Au-Pt nanoparticles" *in preparation*.

Other publications:

- 5) Nemygina, N. A., Nikoshvili, L. Z., Tiamina, I. Y., Bykov, A. V., Smirnov, I. S., LaGrange, T., ... & Kiwi-Minsker, L. (2018). Au Core–Pd shell bimetallic nanoparticles immobilized within hyper-cross-linked polystyrene for mechanistic study of Suzuki cross-coupling: homogeneous or heterogeneous catalysis?. *Organic Process Research & Development*, 22(12), 1606-1613.

Abstract

The main objective of the thesis is to explore elementary mechanisms of structural and morphological evolutions in mono and bimetallic Face-Centered Cubic (FCC) nanoparticles. Comparison of X-ray diffraction (XRD) measurements with atomistic simulations strongly suggests that most of synthesized FCC nanoparticles has internal multidomain structure with domains connected in 3D via stacking fault or twin (111) planes. To get insight into this structure three tasks were set: a) development of a tool for bulk morphology analysis, b) understanding of stacking defects formation mechanisms, and c) analysis of temperature-induced evolution of structure and morphology in mono and bimetallic samples. To complete each task, extensive computational simulations involving energy minimization and molecular dynamics calculations were used. After that, the obtained theoretical predictions were verified by experimental observations.

Noble metal nanoparticles (NPs) are promising materials in a wide range of fields: catalysis, medicine, fuel cells, sensors, and so on. Researchers often consider nanoparticle properties as a function of their size and size distribution; meantime NPs interior is neglected. Although several theoretical and experimental studies indicate that the appearance of structural defects can affect resulting properties. So far, the bulk morphology analysis was mainly studied by high-resolution microscopy techniques, which has drawbacks making it not applicable as a routine tool and unavailable for many scientists.

The first part of the thesis is devoted to the development of a bulk morphology analysis method based on X-ray diffraction (XRD). It's known that cuboctahedron (CUB), decahedron (DEC), and icosahedron (ICO) XRD patterns are different. The differences resemble 1D effect of small stacking and twinning probabilities described by Warren in 1960s. However for 2D stacking (DEC) or 3D (ICO), the appearance of a local 5-fold rotation symmetry axis, non-compatible with FCC lattice, causes additional strain. Using computational simulations, one can disassemble a decahedron into segments (domains) and meticulously explore the 3D twinning effect on XRD patterns. This approach allowed development of the multidomain XRD (MDXRD) method to perform improved mean size and bulk morphology analysis of noble metal NPs. MDXRD approach was verified on various mono – and bimetallic samples and showed a good agreement with a reference techniques.

The thesis's second part focused on mechanisms of the formation of a stacking defects. The existing concepts describe them mainly on the level of elementary processes and cannot describe the formation of DEC or ICO. During the development of MDXRD, it was found that vacancies inside NPs may cause twinning. Once the vacancy concentration in the perfect FCC lattice exceeds a critical concentration, the cluster structure becomes unstable, causing the formation of stacking defects. This approach, when one adds vacancies to the existing cluster, allows computational simulations of the appearance of various multiply twinned particles. Even more, the vacancy driven twinning approach allows obtaining locally a hexagonal close packed (HCP) gold!

The last part of the work explores the structural and morphological evolution of immiscible bimetallic Au-Pt samples during heating. Au-Pt phase diagram predicts the formation of alloy, core-shell, and Janus particles, wherein one structure may transform to another. Despite great

interest to the material (in particular Au-Pt), elementary processes of these structural transitions are not well explored. The effect of morphology was only theoretically considered. The development of MDXRD and vacancy driven twinning allowed unrevealing new trends and elementary steps in phase separation and segregation processes.

Streszczenie

Głównym celem pracy jest poznanie struktury mono- i bi-metalicznych FCC (sieć regularna ściennie centrowana) nanocząstek i wnikięcie w podstawowe mechanizmy jej ewolucji. Analiza wyników pomiarów dyfrakcji rentgenowskiej (XRD) sugeruje, że nanocząstki FCC uzyskane na drodze chemicznej najczęściej mają złożoną strukturę wielozbliźniaczonych domen o perfekcyjnej strukturze FCC i ta złożoność może mieć wpływ na ich właściwości, np. katalityczne czy optyczne. Wpływa ona również na ewolucję temperaturową struktury. Dyfrakcyjny wgląd w te elementy nanostruktury jest nowym wynikiem pracy. Osiągnięcie tego celu w pracy jest realizowane przez trzy podstawowe zadania: (a) zbudowanie metody analizy wielozbliźniaczonych struktur FCC, (b) wnikięcie w mechanizmy powstawania błędów ułożenia w trzech wymiarach, i (c) analiza ewolucji temperaturowej tych elementów struktury w mono- i bi-metalicznych nanokrystalicznych próbkach. Zadania te były realizowane przez szerokie wprowadzenie do analizy dyfraktogramów nanoproszkowych, wyników symulacji atomistycznych nanocząstek FCC, obejmujących budowę złożonych nanostruktur, ich relaksację energetyczną i ewolucję temperaturową w toku symulacji dynamiki molekularnej oraz analizę ewolucji obliczanych dyfraktogramów proszkowych.

W literaturze naukowej rolę nanocząstek metali szlachetnych w katalizie, medycynie, ogniwach paliwowych, sensorach etc. najczęściej analizuje się zwracając uwagę na średni rozmiar cząstek FCC, kształt i rozkład rozmiarów tych cząstek. Subtelna struktura nanodomenowa w objętości nanocząstek jest zwykle zanedbywana. Częściowy w nią wgląd może oferować wysokorozdzielcza transmisyjna mikroskopia elektronowa, choć mająca własne, istotne problemy związane z transportem energii i ładunku. Odziaływanie wiązki rentgenowskiej (choć z założenia słabsze) ma wpływ na ewolucję tej nanostruktury analizowaną w pracy. Zaproponowaną w pracy metodę można stosować jako rutynowe i łatwo dostępne narzędzie analizy.

Podstawom metodologicznym analizy wielozbliźniaczonych struktur FCC poświęcona jest część pierwsza pracy. Analizuje ona wpływ na proszkowy dyfraktogram rtg. zbliźniaczeń idealnych nanokryształów (przez wprowadzenie płaszczyzny odbicia zwierciadlanego), jak i lokalnych zbliźniaczeń obecnych w znanych idealnych i zrelaksowanych energetycznie nanostrukturach jak dekaedry czy ikozaedry lub w ich fragmentach. Można w ten sposób analizować zarówno efekty zaburzenia symetrii jak i pojawienia się mikronaprężeń związanych z przesunięciami atomów z węzłów sieci idealnej na skutek relaksacji energetycznej, np. w pobliżu pięciokrotnej osi symetrii. Wyniki rozszerzają formalną analizę Warrena z lat 60-tych ub. wieku na struktury bardziej zdefektowane i o błędach ułożenia rozłożonych w trzech wymiarach. Zaproponowano praktyczną metodę wyznaczania średniego rozmiaru nanodomeny oraz średniej liczby takich nanodomen w typowej nanocząstce FCC. Metodę zweryfikowano na próbkach szeregu mono- i bi-metalicznych materiałów porównując jej wyniki z wynikami pomiarów mikroskopowych i rozpraszania niskokątowego promieniowania rtg.

Druga część pracy poświęcona jest mechanizmom powstawania błędów ułożenia w strukturach FCC. Obok analizy literaturowej, zaproponowano metodę generowania takich struktur w symulacjach atomistycznych poprzez usunięcie przypadkowych atomów struktury (tworzenie wakancji sieciowych) w zadanym stężeniu i relaksację energetyczną całej struktury. Powyżej pewnego progowego stężenia wakancji struktura przechodzi w wielozbliźniaczoną i podlega

charakterystycznej ewolucji temperaturowej. Dyfraktogramy takich struktur są podobne do dyfraktogramu dekaedru a struktury oferują realny model, w którym można analizować zarówno efekt pojawienia się nowych odległości międzyatomowych jak i ich rozrzutu związanego z naprężeniami. Struktury takie mogą np. ilustrować powstawanie lokalnych obszarów o ułożeniu płaszczyzn (111) w sekwencji struktury heksagonalnej ciasnego upakowania (HCP).

Ostatnia, trzecia część pracy skupiona jest na analizie temperaturowej ewolucji struktury fazowej i nanodomenowej bimetalicznych nanostopów Au-Pt, makroskopowo niemieszalnych. Znane z literatury diagramy fazowe przewidują rozkład termiczny stopu i ewolucję struktury fazowej do układów typu rdzeń-powłoka (ang. core-shell) czy typu Janus. Jednak elementarne mechanizmy są w literaturze słabo opisane a wpływ struktury nanodomenowej dotychczas nie był analizowany. Zastosowanie opracowanej metody analizy pozwala wnikać w mechanizmy atomistyczne ewolucji temperaturowej i zmian struktury fazowej.

Table of Contents

Acknowledgments	iii
Funding.....	v
Declaration of originality	vi
List of publications.....	vii
Abstract	viii
Streszczenie.....	x
1 Introduction	1
1.1 Monometallic Gold NPs	3
1.1.1 Morphology analysis	3
1.1.2 Strains / microstrains	6
1.1.3 Vacancies in bulk	7
1.2 Bimetallic Gold - Platinum NPs	8
1.2.1 Immiscible alloy structures	8
1.2.2 Mechanisms of diffusion.....	11
1.3 Basics of measurement tools	12
1.3.1 XRD	12
1.3.2 SAXS.....	16
1.3.3 XRF	17
1.3.4 TEM	18
1.3.5 Basics of computational simulations:.....	18
2 Experimental and methodology section	20
2.1 NPs synthesis	20
2.1.1 Group 1 Au@PVP.....	20
2.1.2 Group 2 Au@PVP@SiO ₂	20
2.1.3 Group 3 Au ₅₅ Pt ₄₅ @SiO ₂	21
2.1.4 Group 4 Au@C	22
2.1.5 Group 5 Au ₅₅ Pt ₄₅ @C.....	22
2.2 Experimental setups.....	23
2.2.1 XRD	23
2.2.2 TEM	23
2.2.3 XRF	23
2.2.4 Ex-situ measurements	23

2.2.5	In-situ measurements.....	25
2.2.6	Synchrotron X-ray exposure	28
3	Results and discussion.....	29
3.1	MDXRD	29
3.1.1	Twinning effect	29
3.1.2	Domain approach	33
3.1.3	Experimental application.....	43
3.1.4	Corrections and limitations	46
3.1.5	Summary of MDXRD	48
3.2	Vacancy driven twinning.....	50
3.2.1	Vacancy driven twinning	51
3.2.2	Experimental observations: ex-situ heating	65
3.2.3	Experimental observations: effect of X-ray	67
3.3	Phase segregation and separation in bimetallic NPs	79
3.3.1	Alloyed, Core-shell, and Janus models	79
3.3.2	Measurement strategy	82
3.3.3	Au ₅₅ Pt ₄₅ @C.....	83
3.3.4	Au ₅₅ Pt ₄₄ @SiO ₂	89
3.3.5	Au-Pt segregation concept	93
4	Conclusions	96
5	List of abbreviations.....	99
6	References	100

1 Introduction

For a long time, nanoparticles (NPs) have been the subject of intensive studies. Among almost infinite variety of ceramic, polymeric, semiconductor, organic, and hybrid nanoparticles, special attention is paid to monometallic gold and bimetallic gold-platinum NPs.

Colloidal gold solutions have been in use since at least 4th century [1]. However, scientific investigations of nanoparticle properties were initiated by Michael Faraday in the middle of 19th century [2]. He discovered that reducing a gold chloride solution creates “activated gold” with a “ruby” color. With the development of analytical tools in the 20th century, interest in nanoparticles only grew. Nowadays, gold NPs play essential roles in electronics [3], photodynamic therapy of cancer [4], therapeutic agent delivery [5], sensors [6,7], biological imaging [8, 9], a variety of diagnostics [10,11], and a wide range of catalytic reactions [12, 13]. Gold-platinum NPs are less versatile; they can be used as antibiotic agents [14], catalysts in different reactions [15], and sensors [16], but the most critical application is as electrocatalyst in fuel cells [17, 18].

It is known that such unique physical and chemical properties arise because of specific electronic structures, large surface-to-volume ratio, the surface itself, and shape of the nanoparticles. However, these explanations do not consider another critical aspect – interior of the nanoparticles. Various twin planes and stacking faults can likely appear inside face-centered cubic (FCC) metals. Structural defects appearance leads to various strains forming [19, 20]. The problem is that their influence on NP properties is poorly explored. In many cases, the existence of defects is simply neglected.

Several works point to this problem. It was experimentally shown that elastic (micro)strains can modify the properties of a catalyst [21, 22, 23]. Not only catalytic but also electronic and optical properties can be affected by microstrains [24, 25, 26]. Nevertheless, there is still a significant gap in understanding the correlations between FCC NPs structures and their properties. One of the main reasons is lack of experimental tools for the bulk morphology analysis of NPs.

At present, there is only one tool allowing analysis of twin plans and stacking fault: transmission electron microscopy (TEM) [27, 28, 29]. However, TEM analysis has a number of fundamental issues. The first one is the effect of the electron beam on the sample. The focused electron beam can change a native structure of clusters [30, 31]. Secondly, all analyzed particles are chosen arbitrarily and obtaining a statistically meaningful number of snapshots is difficult. The TEM-based numerical characterization of twinning is provided only in exceptional studies [32, 33]. Besides the abovementioned issues, one must remember that high resolution microscopy analysis is time-consuming, expensive, and requires specific environmental conditions (e.g. vacuum).

The first part of the current work aims to develop an alternative to TEM, X-ray diffraction (XRD) method for the numerical characterization of FCC NP morphology [34]. As was indirectly predicted

by Warren [35], twin and stacking faults affect the height of diffraction peaks. Knowing the height ratio of non-affected to affected peaks, one can find a mean number of domains in the average cluster. The domain – is an ideal FCC fragment of the cluster without stacking or twin faults. The method allowing calculation of the number of domains is called the multidomain XRD (MDXRD). The first part of the thesis is devoted to development and experimental verification of the method.

Another essential aspect of twinning is a complex twin/stacking faults formation mechanism. There are three basic concepts describing appearance of the stacking faults: as a result of coalescence [36, 37]; as chaotic condensation of atoms from the gas phase [33]; or as stepwise nucleation with formation of nucleation seeds [38]. During the development of MDXRD, another mechanism was found – vacancy driven twinning. It is known that FCC solids contain some equilibrium concentration of vacancies [39]. However, it was found that once the density of vacancies exceeds ~13%, a complex three-dimensional twinning may occur. The second part of the thesis is focused on describing the concept; attempts to detect vacancies and observe twinning by in-situ XRD.

One crucial difference must be highlighted in comparing the vacancy driven concept with other mechanisms. The first three mechanisms do not consider appearance of a hexagonal closed-packed (HCP) gold [40]. Even though they theoretically allow the HCP structure to be formed, their principles can not be used in practice in computational simulations. Meantime, the vacancy driven twinning approach can be used and already allowed to obtain the HCP gold phase from the ideal FCC cluster!

By adding the second metal (platinum) to gold, the resulting properties and structure of obtained NPs can dramatically differ from the corresponding pure metals. The Au-Pt mixture is considered non-miscible and within its miscibility gap, various configurations are possible: alloy, core-shell [41,42], onion-like [43], and Janus [44] structures. The appearance of one or another structure depends on the temperature, composition, and size of NPs. Wherein one structure may transform into another as were experimentally observed [45, 46]. These transformations are controlled by thermodynamics, namely by reduction in the Gibbs free energy.

The problem is that the nanoalloys ordering is mainly studied by computational simulations [47, 48], which suffer several limitations. First, the analyzed models are small and their structure is oversimplified: the twinning is neglected; in core-shell and Janus particles, Au-rich and Pt-rich phases consist of pure metals, which contradicts the experimental observations. Secondly, the potential parameters used were obtained from a limited experimental basis. Lastly, the elementary process of phase segregation and transport phenomena are not fully known.

The last part of the thesis addresses these issues and focuses on temperature-induced phase separation and segregation in bimetallic gold-platinum nanoparticles. Combined X-ray diffraction and microscopy techniques allowed to monitor stepwise evolution of alloyed AuPt particles and significantly extended the current understanding of these processes.

1.1 Monometallic Gold NPs

Gold belongs to the face-centered cubic structures with the first coordination number equal to 12. When a central atom is surrounded by a shell consisting of 12 other atoms, it creates a 13-atom cluster. This configuration is the first member of the so-called “magic number” cluster series, described by van Hardeveld and Hartog in 1969 [49]. As additional shells are added to the cluster, the number of atoms increases as 13, 55, 147, 561, and so on. Nanoparticles built up according to this series have the shapes of Platonic solids. In the case of the ideal FCC cluster, the magic number series result in NPs with a cuboctahedron (CUB) shape. Alternatively, in the special case of multiply twinned structure, the same series may form an icosahedron shape (ICO). Despite the fact the ICO cluster is highly strained, all bulk ICO atoms have the coordination number equal to 12. Therefore, both ICO and CUB allow the atoms to pack efficiently and minimize their surface energy, which makes these morphologies stable.

Besides ICO and CUB, another Platonic solid can be used to build FCC NPs – decahedron (DEC). The DEC bulk atoms also have the first coordination number equal to 12. However, because of this solid's specific shape, the previous “magic number” is no longer applicable [50]. Moreover, extensive theoretical simulations showed [51] that the DEC built shell by-shell is not the most energetically favorable configuration. The most stable type of DEC is the truncated (Marks [52]) DEC with particular truncations along twin planes. This type of decahedron was observed experimentally many times [53, 54, 55].

Despite the fact that there are other types of FCC cluster shapes, CUB, DEC, and ICO are widely accepted as the most stable ones. Some researchers do not consider other morphologies at all, assuming that FCC NPs may only exist as CUB, DEC, or ICO [32, 33].

1.1.1 Morphology analysis

The appearance of one or another FCC morphology is usually justified by its minimum potential energy per atom or its derivatives [56, 57]. The lower the energy of a given morphology, the more likely it can be found. Here is the result of the potential energy analysis of CUBs, ICOs, and Marks DEC series, which were calculated using Sutton–Chen n -body potential [58] implemented in the CLUSTER software [59].

As seen from Figure 1 **a**, for small clusters (< 600 atoms), the difference between the curves is very subtle and provides no clear indication of the dominant morphology. This can explain why experimentally observed \sim same-size NPs may have different morphology [33]. Figure 1 **b** shows that for the big clusters (>600 atoms), the decahedron shape is the most stable, while the formation of the icosahedron configuration is less favorable.

The problem with this approach is that NPs surface atoms make a strong contribution to the total energy. Since these structures have different shapes, they expose different facets (ratio of facets) with different surface energy; therefore, their total surface energies differ. This effect is better

visible for CUB, DEC, and ICO having a spherical shape. The non-relaxed large CUB / DEC / ICO models were cut in the form of a sphere to obtain the same size models (“ball cutoff” option in Cluster), followed by relaxation.

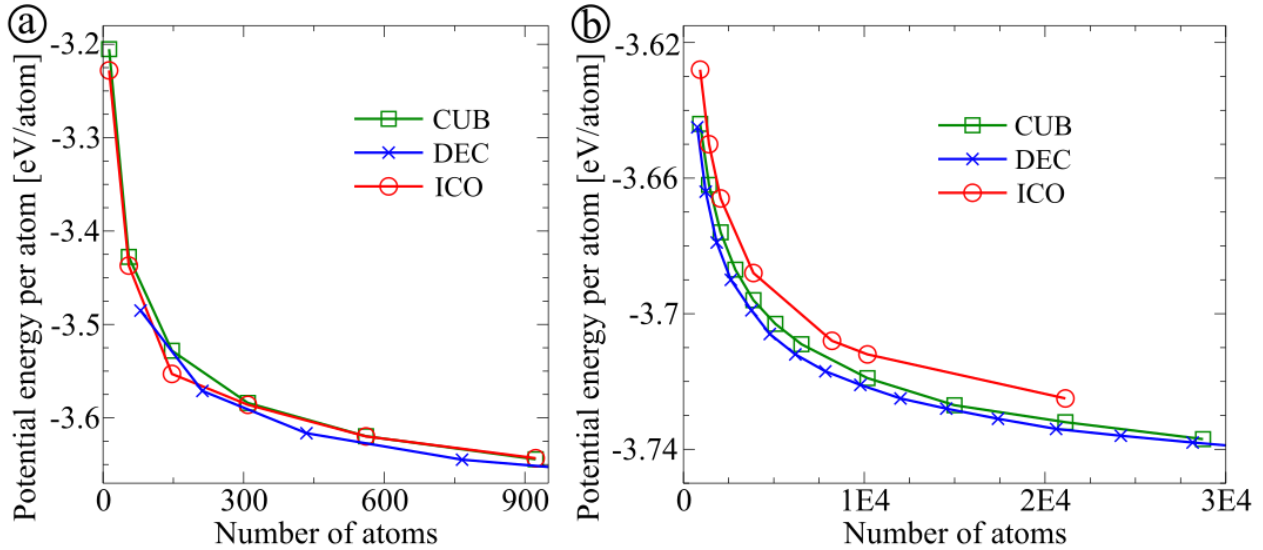


Figure 1 The minimum potential energy per atom calculated for different size cuboctahedrons, decahedrons, and icosahedrons: a) for small size clusters; b) for bigger clusters. All DEC's have the shape of Mark's DEC with configuration $n=m$; $p=3$ [51], corresponding to the most stable state.

As can be seen from Figure 2 a, the difference between potential energy per atom of spherical CUB, DEC, and ICO is negligibly small. Considering the original shapes, the difference was remarkable (Figure 1 b). Despite the similarity of spherical models, their interiors are different. Using OVITO [60], one can calculate volumetric strain distribution in the relaxed models. It is calculated locally (from 12 neighbors displacements) for atoms having local structure sufficiently well resembling the perfect crystal lattice [60].

The exact strain distribution inside clusters is better visible, when the radial distribution of strains is considered. Figure 2 b shows that inside the single-domain cuboctahedron structure, the strains are uniformly distributed in bulk and the cluster contracts close to the surface (Figure 2 b green line). The DEC strain distribution looks similar (Figure 2 b blue line). However, the compressing forces in bulk are stronger than in CUB, what is surprising. It's known that five domains of DEC cannot be perfectly merged because of the 7.35° angle deficiency in the decahedron stacking. Therefore one can expect to see the expansion of the lattice, which cannot be seen.

The DEC expansion is hindered because of the algorithm of volumetric strain analysis. This algorithm calculates strains along three directions (X, Y, Z) and averages all values. As a result, the expansion is overridden by the radial contraction forces. Nevertheless, the expansion can be seen by running an elastic strain calculator along only one (X, Y, or Z) direction.

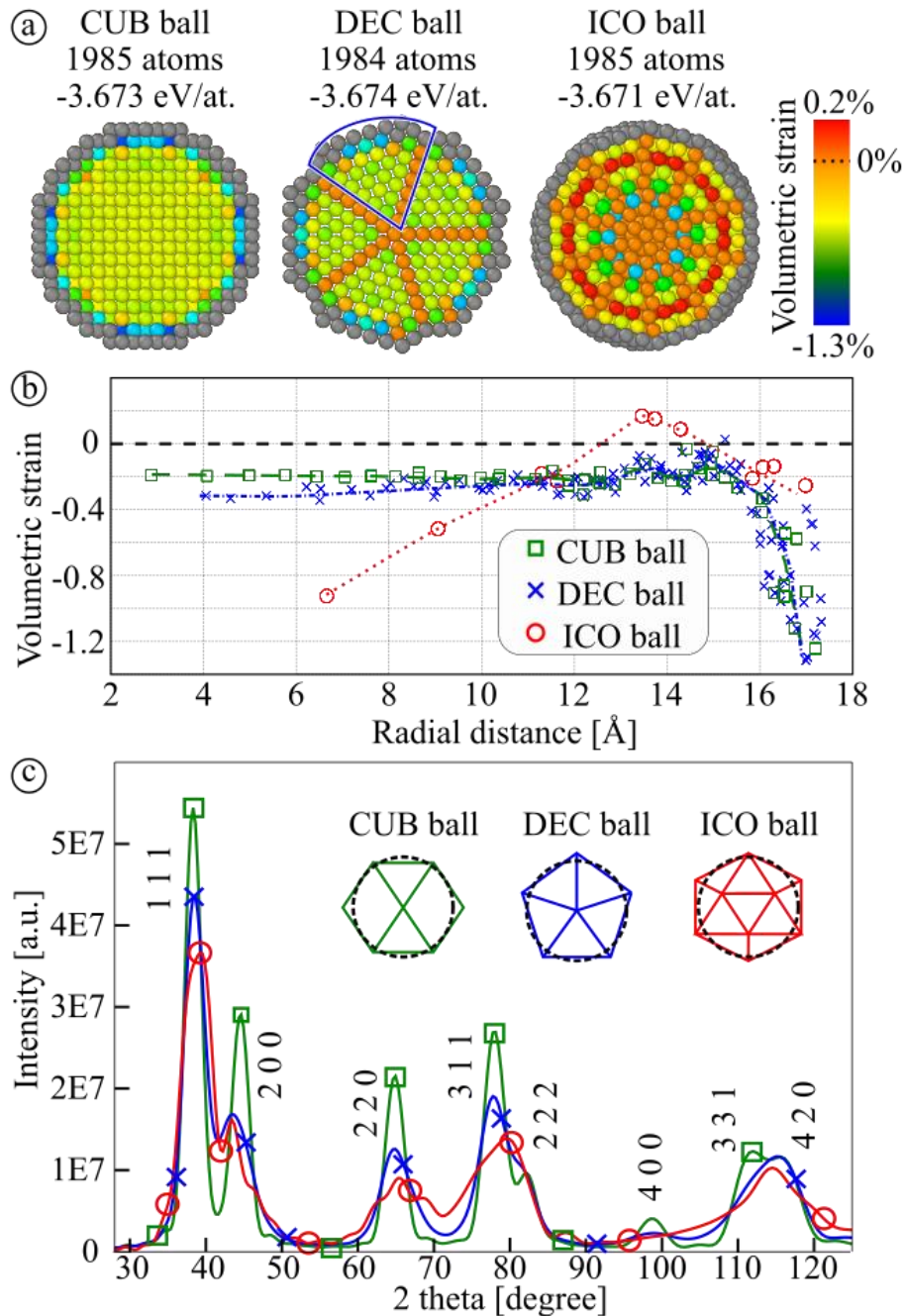


Figure 2 a) Strain distribution maps (by OVITO) of nearly spherical models having cuboctahedron, decahedron (blue line shows one domain of decahedron), and icosahedron morphology; d) the volumetric strains distribution for each atom as a function of radial distance (only FCC-like strained atoms are shown: for CUB – 1277 atoms; for DEC – 985 atoms; for ICO – 700 atoms); c) calculated XRD diffraction patterns of the analyzed CUB, DEC, and ICO models. It should be noted that surface atoms (shown in grey) are more susceptible to deformation and were excluded from the volumetric strain analysis. Nevertheless, since any deformation of a nanoparticle structure leads to a change in potential energy, the considerations of potential energy per atom values always include the effect of the surface deformation.

Figure 2 **b** shows that the strain distribution of ICO is different from those of CUB/DEC: close to the center, it is strongly negative (contraction); closer to the surface, it is positive (expansion). These features are caused by a unique arrangement of 20 domains of the ICO. Each ICO domain can be considered as part of three neighboring decahedron-like structures (Chapter 3.1.2.2). Therefore each segment is affected by “triple” angle deficiency (because there are three DEC-like structures) from each side of the domain.

Figure 2 **c** illustrates the calculated XRD patterns of the spherical CUB, DEC, and ICO models. One can see the morphology of NPs strongly affects diffraction patterns. If the one-domain CUB has narrow, regular peaks, the multidomain ICO has broad, narrow, and asymmetric peaks. All these features indicate the sensitivity of XRD to the morphology of NPs. Using extensive computational simulations, it was shown that the height ratio of 220 to 111 peaks directly indicates a mean number of domains in the cluster [34]. The method allowing the calculation of a number of domains is called multidomain XRD and is described in Chapter 3.1.

1.1.2 Strains / microstrains

The morphology of NPs determines the appearance of various strains (Chapter 3.1.2), which affect the material's properties, such as its mechanical, electrical, and magnetic properties. Therefore, it is crucial to have control over strains. However, only few techniques allow strain analysis of nanoparticles: TEM [61, 62] and Williamson – Hall (W-H) analysis of X-ray diffraction patterns.

The width of the diffraction peaks is determined by instrumental broadening and properties of the sample: strains and size of nanoparticles. By analyzing the slope of the linear fit between the peak width multiplied by cosine of the Bragg's angle and the sinus of Bragg's angle, the W-H method allows distinguishing between strains and size contributions. The method's simplicity and indispensability made W-H analysis the most wide spread technique for strain analysis.

As can be seen from Figure 3 **a**, the W-H analysis can adequately describe only the one-domain CUB model. The more complex structure, the less accurate the method. Besides, it isn't easy to interpret the physical meaning of a slope value. Once a structure is affected by microstrains, it can be understood as a contraction or expansion of a lattice. However, peak broadening also appears because of twin planes and stacking faults (Figure 3 **b**). Therefore, considering slope value as a direct indication of contraction or expansion is a vast oversimplification.

The problem of interpreting the W-H results is highlighted by comparing the Marks DEC and multidomain DEC-like particle (Figure 3 **a** right-hand side graph). The W-H slope values are - 0.0025 and 0.0023, respectively. These values suggest that these two structures should be different. Ideal DEC consists of 5 domains, while the considered multidomain particles are made of ~4.3 domains, so their morphologies are similar. The main difference between these particles is the distribution of twin planes. In the case of the multidomain particle, they are randomly oriented. It seems that the W-H slope value cannot be adequately interpreted because it is difficult to distinguish between different strains and microstrains effects.

The issue of the strains analysis was considered by Warren [63], Longo and Martorana [64]. Some details of their approach are discussed in Chapter 3.1.

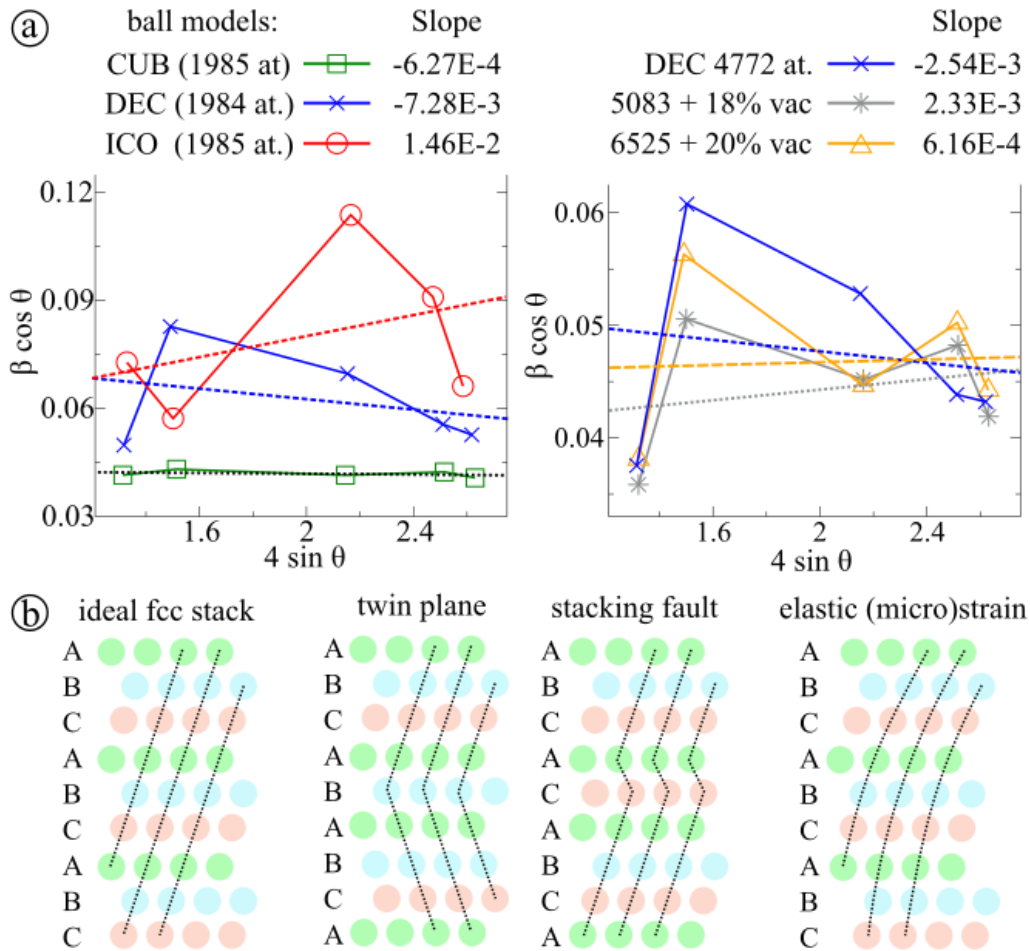


Figure 3 a) The left-hand side graph shows the Williamson-Hall plot analysis for the CUB (1985 atoms), DEC (1984 atoms), and ICO (1985 atoms) ball models. The right-hand side graph shows the Williamson-Hall plot analysis for the DEC ($m=n$, $p=3$; 4772 atoms) and multidomain nanoparticles made of CUB 5083+18% of vacancies and CUB 6525+20% of vacancies after energy minimization (Figure 25); b) the scheme showing different types of strains: twin planes, stacking faults, and elastic (micro) strains.

1.1.3 Vacancies in bulk

Another type of defect in FCC solids is a vacancy. One of the very first experimental observations of vacancies was done by Simmons and Balluffi in the early 60s. The proposed scheme of measurements allowed to determine their equilibrium concentrations in silver [65], gold [66], and copper [67]. The idea was very simple: to compare the thermal expansion of materials in two different size scales: the macro level and the lattice parameter level.

Here is the scheme of measurements on a gold bar (Figure 4 a). A 50 cm long gold specimen (99.999% Au) was obtained by melting followed by a special cooling procedure. Next to the sides of the bar, there were placed reference marks. A filar micrometer microscope monitored the distance change (ΔL) between these marks. Meanwhile, single-crystal X-ray diffraction controlled the lattice parameter change (Δa).

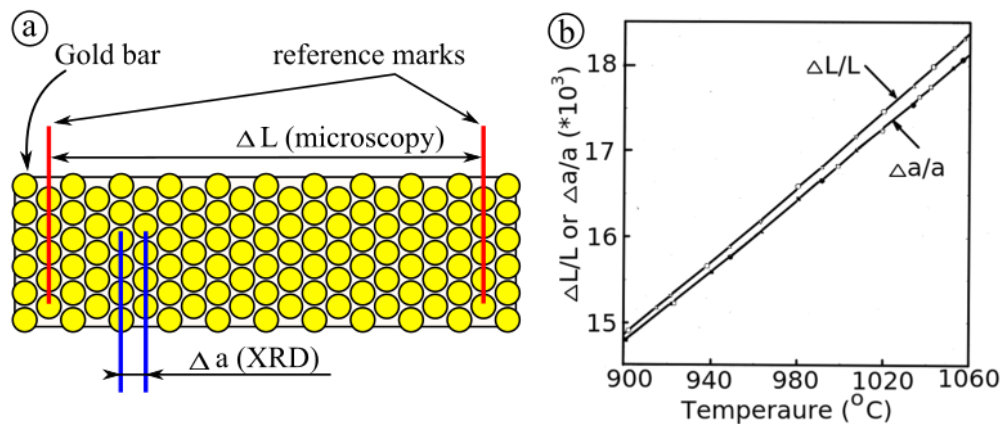


Figure 4 Scheme of the Simmons and Balluffi experiment for measuring the equilibrium concentration of vacancies inside a gold bar; b) thermal expansion coefficients of the lattice constant ($\Delta a/a$) and of the estimated distance between reference marks ($\Delta L/L$) [66].

Figure 4 b shows the result of the thermal expansion coefficient measurements. At relatively low temperatures (room temperature – 340 $^{\circ}\text{C}$) the difference between ΔL and Δa was negligibly small. However, at high temperatures (900 – 1000 $^{\circ}\text{C}$) it becomes well visible, which indicates the appearance of thermally generated effects. Simmons and Balluffi suggested that before the melting temperature, 80% of defects are single vacancies; the rest are di – and trivacancies.

1.2 Bimetallic Gold - Platinum NPs

1.2.1 Immiscible alloy structures

The Au-Pt mixture is considered non-miscible (Figure 5 a) and various structures are possible within its miscibility gap. As a first approximation, these structures` stability can be determined by analyzing the potential energy per atom of various relaxed models. As can be seen from Figure 5 b, the most energetically favorable structure is a core-shell and the most stable morphology is DEC shape.

The potential energy of DEC is optimal for both mono – and bimetallic particles because it exposes facets with significantly lower surface energy than CUB and ICO morphologies. A similar principle explains the stability of the core-shell configuration (regardless of morphology). The surface

energies of Au and Pt are 1.5 and 2.48 J/m², respectively [68]. Therefore, thermodynamic analysis indicates that the core-shell structure is the most energetically favorable [47].

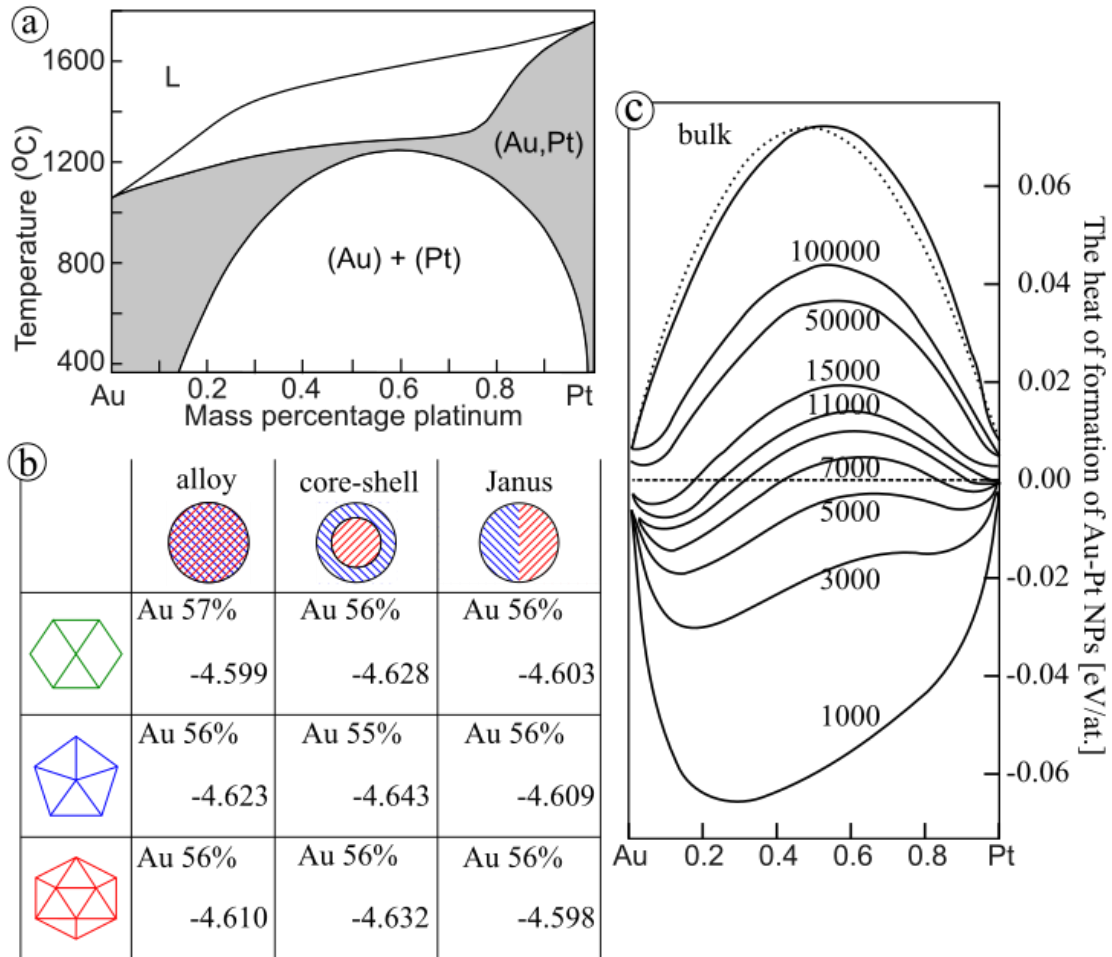


Figure 5 a) Au-Pt phase diagram [69]; b) Analysis of potential energy per atom for various relaxed models (Sutton–Chen n–body potential; Cluster software). The DEC models have m=13, n=9, p=1 structure and consist of 4957 atoms. This configuration of DEC is not the most energetically favorable one. It was chosen to have a similar number of atoms with CUB and ICO models (5083 atoms); c) The dependence of the heat of formation of Au-Pt alloy structure on the number of atoms in a cluster [19].

However, such an approach does not consider the cluster's size. Qi et al. [70] described the dependence of cohesive energy on the particle size (D). If a given particle is large enough, its cohesive energy approaches the bulk value. The proposed size dependency can be described as follows:

$$E_c^p = E_c^b \left(1 - \frac{d}{D}\right)$$

where E_c^b and E_c^p are cohesive energy of the bulk material and of the analyzed nanoparticle, d is a diameter of a single atom of a given material. Based on equation 1 Xiao et al. [71] analyzed alloying of Au-Pt in small clusters. They found that the heat of formation of NPs with size below 6 nm is negative (Figure 5 c). In other words, the appearance of small, alloyed particles is thermodynamically favorable and such structures are stable. This conclusion seems realistic because of numerous experimental observations of small and alloyed nanoparticles [72, 73].

The processes described above are even more complex. Analysis of short-range order parameters at different temperatures and ratios of metals [48] allowed to determine conditions for appearance of Janus NPs. Previous models were oversimplified and considered only symmetrical models with pure Au and Pt phases. Meantime, the full description of the bimetallic structure should consider morphology and chemical ordering (arrangement of metals in the structure).

The core-shell structure is stable when symmetrical and the core part resembles a magic number cluster. However, it was shown [74, 75, 76] that breaking core symmetry can result in the appearance of so-called quasi-Janus particles. These particles have no clear straight-plane border between phases. It resembles a core-shell structure with a core close to the surface. This off-center configuration was found to be effective in the release of strains. Besides, the quasi-Janus particles were observed experimentally multiple times [77, 76, 78].

Parsina and Baletto [79] theoretically described the change of NP asymmetry during the growth process. They continuously added single atoms one by one to already existing core-shell or Janus structures. Therefore, the overall shape and the ratio of metals were modified. After running the molecular dynamics simulation, the possibility of transforming core-shell into quasi-Janus (and reverse) was clearly demonstrated. These simulations extend the original concept of Wang and Hou [48], who considered the appearance of the bimetallic structure as a function of the ratio of metals (Figure 6 b).

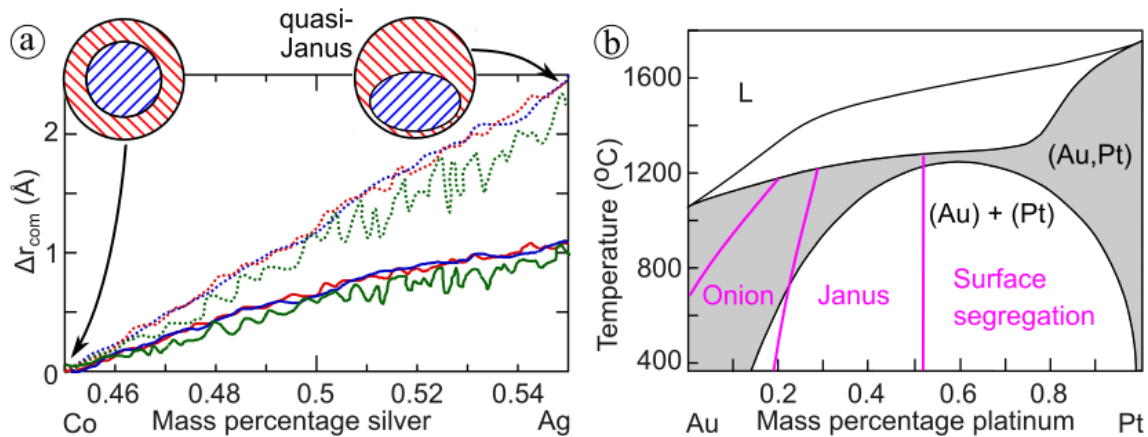


Figure 6 a) Supply of silver atoms to core-shell $Ag_{146}Co_{178}$ cluster leads to transformation into Janus structure at 450 K (blue), 550 K (red), 650 K (green). Δr_{COMCo} is the distance between the center of mass (COM) of the Co-only subcluster (solid line) and Co subcluster (dotted line). b) AuPt phase diagram showing the dependence of bimetallic NP structures on the concentration of metals [48].

1.2.2 Mechanisms of diffusion

The discussed computational simulations do not consider the mechanism of diffusion. For simplicity, let's consider self-diffusion in monometallic copper. There are three proposed mechanisms: direct exchange, ring exchange, and vacancy (Kirkendall) exchange (Figure 7) [80]. Huntington and Seitz [81] calculated the activation energy for the corresponding exchange processes. The Kirkendall (vacancy) mechanism requires much less energy than others, making it the dominant diffusion mechanism.

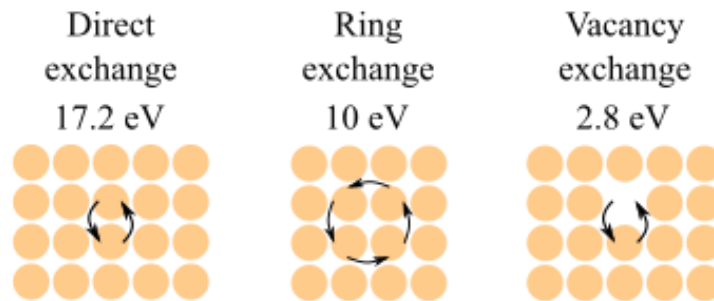


Figure 7 Atomic diffusion mechanisms in monometallic copper

Since there is no gradient of concentrations in monometallic samples, the self-diffusion is a random process, while in bimetallic samples, it is controlled by thermodynamics. However, in exceptional cases, diffusion can proceed against thermodynamic predictions. If one of the bimetallic particle constituents (with a higher surface energy) is being kept at the surface, another element will be forced to occupy the core space.

Such configuration leads to “freezing” of the surface. As a result, the new vacancy generation driven by surface mobility became limited, making direct and ring exchange mechanisms dominant over the Kirkendall exchange. This approach can be used for better understanding and experimental measuring of the diffusion coefficients.

In practice, this approach was used by Kaszukur et al. [82] to measure the diffusion coefficients of Pd and Ag. Subsequently exposing PdAg nanoparticles to CO and He, the selective segregation of Pd and Ag (respectively) was triggered (Figure 8). Strong chemisorption of CO molecules on Pd atoms allows immobilizing the captured palladium atoms on the surface, creating Ag core – Pd shell structure. When vacancy generation is suppressed, the segregation rate becomes slower. Once NPs get exposed to He, the thermal generation of vacancies becomes active, leading to a quick rearrangement of the previous structure into Pd core – Ag shell configuration.

It was successfully shown that the (in-situ) XRD technique allows to follow even such a slow and subtle process. During the Pd segregation, the diffraction peak position is determined by the core material's properties (as discussed in detail in Chapter 3.3.1). In this case, the core material is silver (Pd – shell), resulting in a left-hand side shift of peaks. If Ag segregation is triggered, diffraction peaks will move to the right-hand side (because the core gets enriched with Pd).

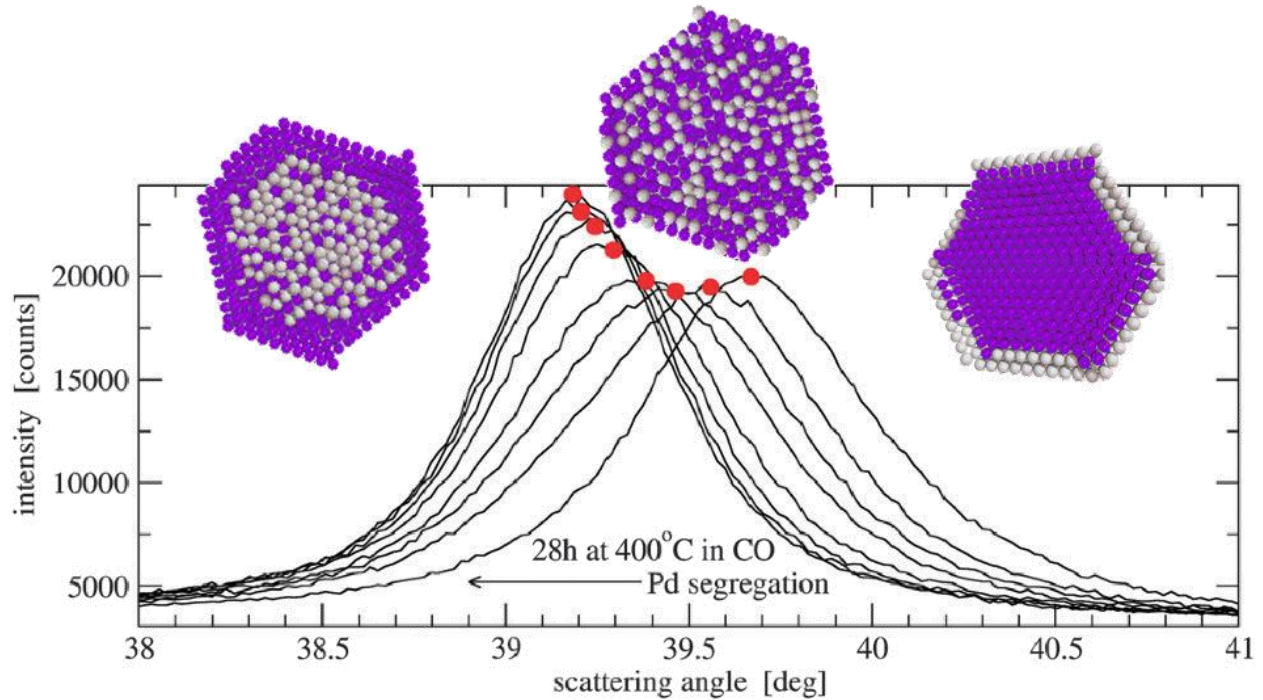


Figure 8 Evolution of the 111 peak position during CO exposure. Reprinted with permission from the authors [82]

1.3 Basics of measurement tools

1.3.1 XRD

X-rays were discovered in 1895 by Wilhelm Röntgen and later understood as electromagnetic radiation with a wavelength of 0.01 – 10 nm. In 1912 Max Laue [83] theoretically described the possibility of diffraction on crystals. One year later, together with Walter Friedrich and Paul Knipping, he published the first photographs of the X-ray diffraction pattern of ZnS crystal [84]. In 1914 Max von Laue was awarded the Nobel Prize “for the discovery of the diffraction of X-rays by crystals”.

The X-ray diffraction phenomenon is based on Rayleigh (elastic) scattering. When the incoming photon interacts with an electron, the latter re-emits radiation of the same frequency and phase. The secondary emitted photons are propagated in all directions, what allows to consider individual atoms as a source of secondary radiation.

In an ideal crystal, atoms are arranged periodically, forming rows of atoms with distance \mathbf{a} in between (Figure 9). The constructive interference is only possible when the path difference (OK-PT) is equal to integer multiplicity of wavelength (λ):

$$(OK - PT) = \mathbf{a} (\cos \alpha_n - \cos \alpha_0) = n_x \lambda \quad 2$$

where n_x – is the diffraction order (must be an integer number).

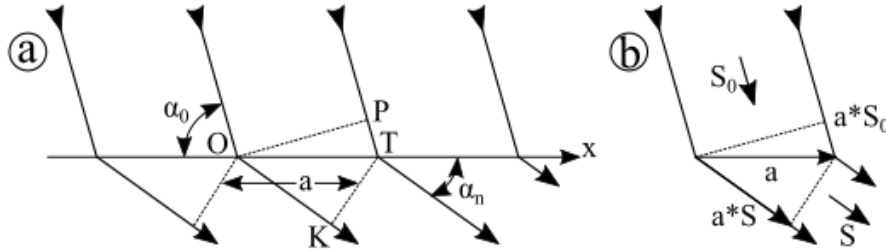


Figure 9 a) Scheme of incident X-ray (with angle α_0) diffraction from the row of atoms along x-axis, α_n – is the angle of the diffracted beam, (OK-PT) is a path difference; b) Scheme of diffraction principle shown in the vector notation.

Equation 1 is known as the first Laue equation. It can be expressed in a vector form (Figure 9 b), where S_0 and S are incident and diffracted angles, respectively. If \mathbf{a} is a translation vector from one lattice node to another, the path difference can be simplified and written as a scalar product:

$$\mathbf{a} (\cos \alpha_n - \cos \alpha_0) = \mathbf{a} * (S - S_0) = n_x \lambda \quad 3$$

Equation 3 describes the one-dimensional case. In order to consider diffraction in three dimensions, one has to include rows of atoms along \mathbf{y} and \mathbf{z} – axes:

$$\mathbf{b} (\cos \beta_n - \cos \beta_0) = \mathbf{b} * (S - S_0) = n_y \lambda \quad 4$$

$$\mathbf{c} (\cos \gamma_n - \cos \gamma_0) = \mathbf{c} * (S - S_0) = n_z \lambda \quad 5$$

where \mathbf{b} and \mathbf{c} – are distances from one lattice node to another along \mathbf{y} and \mathbf{z} – axis; β_0 and γ_0 are incident angles with respect to the \mathbf{y} and \mathbf{z} – axes; β_n and γ_n are scattered angles with respect to the \mathbf{y} and \mathbf{z} – axes. Equations 3-5 are called three Laue equations. These equations describe conditions at which an incident X-ray beam scattered by a crystal lattice forms a diffraction pattern.

A special case of Laue equations is Bragg's law, named after William Henry Bragg and his son, Lawrence Bragg, in 1913 [85]. They simplified three Laue equations into one, which directly indicates the angle at which constructive interference occurs:

$$2 d_{hkl} \sin \theta = n\lambda \quad 6$$

where d is interplanar spacing, θ is the Bragg's angle equal to half of the scattering angle, and n is the reflection order.

Interplanar spacing d_{hkl} value depends on the crystal's elementary unit cell and is considered as a function of hkl – Miller indices. For FCC structure, this dependence can be easily found because all angles in the cubic structure are $\alpha = \beta = \gamma = 90$, and the edges of the cube are equal in all directions ($a=b=c$):

$$\frac{1}{d_{hkl}^2} = \frac{h^2 + k^2 + l^2}{a^2} \quad 7$$

where a is the lattice constant.

1.3.1.1 Powder XRD

The original Laue method considered passing the broad X-ray beam through the single crystal. The problem is that this crystal should be properly oriented to observe a diffraction pattern, which requires special adjustments.

Peter Debye and Paul Scherrer proposed an alternative approach – powder diffraction (pXRD). Fine powder samples consist of many single crystals, which are randomly oriented. If the number of crystals is high enough, there will always be a fraction that will be oriented to satisfy the Laue condition. Each set of (hkl) planes will be presented by one or another fraction of particles, and they all will form their own diffraction cone, creating a set of cones. These sets are also called Debye-Scherrer rings.

To fulfill the requirements for a good quality powder diffraction, the analyzed powder should be fine and have a high number of crystals. If pXRD requirements are not satisfied, then the Debye rings may suffer from discontinuity, which can negatively affect the resulting XRD pattern measured as a 1D section of the rings.

1.3.1.2 Analysis of diffraction patterns

Peak shape function:

In the thesis, the analysis of all diffraction patterns was done by using the Pearson VII function:

$$I(2\theta) = I_{\max} \frac{w^{2m}}{[w^2 + (2^{1/m} - 1)(2\theta - 2\theta_0)^2]^m} \quad 8$$

where m is the shape parameter, w is the peak width. Modification of m parameter value allows to adjust the profile of the function. For $m > 10$, it has a profile of a Gaussian-like function; if $m = 1$, it has a profile of the Lorentzian function. This feature is essential for the description of NPs diffraction patterns. Samples with a broad size distribution have diffraction peaks with a Lorentzian-like shape.

Analysis of peak width:

As the Laue equations show, the smaller number of scattering centers, the broader the corresponding diffraction peak. In 1918 Paul Scherrer [86] proposed a simple formula for the description of peak broadening depending (peak width – β_L) on crystalline size (L):

$$\beta_L = \frac{K\lambda}{L \cos \theta} \quad 9$$

where K – is a shape factor. The main subject of the current studies are nearly spherical NPs with a size below 10 nm. In all cases, the shape factor was assumed to be equal 0.94.

It's known that the Scherrer equation is applicable exclusively to nanoscale objects. Even though some studies mention the effect of “coherently scattering domains” on the applicability of Scherrer equation, there was no strict definition of the domain itself [87]. For example, in some studies [88] “domains” were equivalent to grains.

The current work considers the domain (in terms of FCC structure) as an ideal FCC segment that contains no twin or stacking faults. The fundamental applicability of the Scherrer equation is described in Chapter 3.1.

Immiscible alloys:

The wide miscibility gap of Au and Pt assumes that these metals can be mixed in a different ratio. In the case of alloy, the obtained clusters can be considered as uniform one-phase structures. According to Vegard's law [89], the resulting lattice constant (a_{AB}) of such a system is a weighted mean of lattice constants of pure elements (a_A and a_B):

$$a_{(A_{(1-x)}B_x)} = a_A * (1 - x) + a_B * x \quad 10$$

where x is concentration of the pure component B. Vegard's law is an empirical formula; therefore, some deviations are possible. However, this is the only tool allowing interpretation of lattice constant in bimetallic NPs providing information about composition. In the current work, Vegard's law analysis was accompanied by XRF and TEM Energy dispersive X-ray spectroscopy analysis.

1.3.2 SAXS

The discussed above XRD technique typically analyzes scattering signals in the range of $2 - 140$ two theta degrees, allowing focus on the internal structure of crystals. Measurements in this range are often called wide-angle scattering (WAXS). Meanwhile, measures at lower angles ($\sim 0.1 - 2$ two theta degree) allow focus on the outer properties of materials: shape, density, size, and so on. Scattering signals at low angles are called Small-Angle X-ray Scattering (SAXS). Even though Krishnamurti and Warren showed the first experimental usage of SAXS [90, 91], the fundamental development of SAXS theory is firmly associated with André Guinier [92].

In SAXS measurements, any distance is calculated with respect to the wavelength λ . Therefore, instead of two theta angles (like WAXS), the "length of the scattering vector" or "momentum transfer" q is commonly used:

$$q = \frac{4\pi}{\lambda} * \sin(\theta) \quad 11$$

Typical SAXS pattern can be divided into three regions of interest: Porod, Central part, and Guinier (Figure 10). The Guinier region [92] is dependent on the radius of gyration (R_G , gyradius) of a sample; at small angles, the form factor $P(q)$ is equal to:

$$P(q) \approx a_0 * e^{(-\frac{R_G^2 * q^2}{3})} \quad 12$$

where a_0 is zero-angle intensity, which is proportional to the material properties. R_G shows a radial distance to the point where the moment of inertia is the same as for the body assuming its all mass placed at this point. Gyradius does not provide information on the shape or internal structure of particles.

Information about the shape of a particle can be obtained from the Fourier region (Figure 10 green area). One can calculate the pair-distance distribution function $\rho(r)$ by applying Fourier-transformation to the central oscillating part. This function allows to determine the shape of the analyzed particle. The Porod region is essential for obtaining information about various surface parameters.

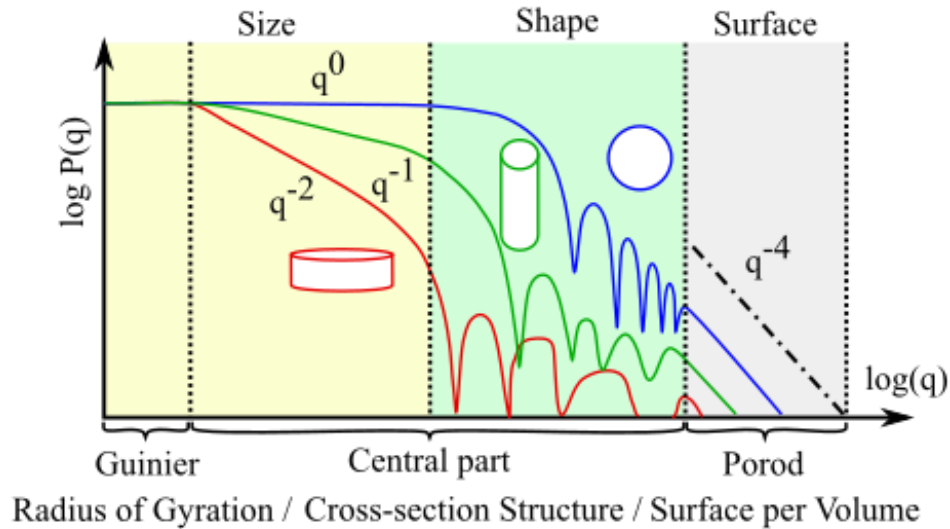


Figure 10 illustration of different regions of SAXS pattern

Despite the difficulties described above, the analysis of spherical nanoparticles is relatively simple. According to Guinier's approximation, the intensity scattered on spherical particles (Figure 10 blue line) is equal:

$$I_{\text{sphere}}(q) = \Delta \rho^2 V_{\text{sphere}}^2 \left[\frac{3}{(qR)^3} (\sin(qR) - qR \cos(qR)) \right]^2 \quad 13$$

where V_{sphere} , R , $\Delta \rho$ are the particle's volume, radius and homogeneous scattering length density.

For a real sample's analysis, one must consider the particle size distribution. Since SAXS is an X-ray diffraction technique, it is sensitive to the volume-weighted mean size of particles. In other words, the contribution of big particles will be greater than that of small ones.

To avoid ambiguity in the interpretation of the data, the SAXS measurements considered within the current thesis were accompanied by TEM analysis. Microscopy analysis confirmed that a model of spherical particles can be applied and provided information about particle size distributions.

1.3.3 XRF

If XRD and SAXS techniques are based on the elastic scattering of X-rays, X-ray Fluorescence (XRF) spectroscopy deals with the fluorescent (or "secondary") characteristic radiation. Each chemical element has its own set of discrete levels of electron energy. Emitted secondary X-rays create a spectrum with a unique "fingerprint" of a given element, which makes XRF attractive for chemical composition analysis.

When a primary X-ray beam with high energy strikes the material, there is a chance that an electron from the inner orbital will be ejected (photoelectron). Electron removal creates an initial vacancy (aka “hole”), making the whole atom excited and unstable. To recover the initial configuration, an electron from an outer shell is “falling” to the inner orbital. Since the electron is transferring from a higher to a lower orbital, it has excess energy that will be emitted as a secondary X-ray photon.

The structure of an atom consists of multiple atomic levels (K,L,M ...), which have their own subshells. During fluorescence, electrons from different inner subshells can be ejected and create vacancies recovered by different high orbital electrons. This variability leads to the appearance of a series of secondary X-rays with well-defined energies. These series create unique for each chemical element spectra. Each peak of such spectra corresponds to a specific transition and is designated according to Siegbahn notation.

1.3.4 TEM

Transmission electron microscopy is an indispensable technique in NPs studies. TEM's applicability range is extraordinarily wide: size, strain morphology analysis, in-situ studies of various phenomena: aggregation, coalescence, catalysis, melting, etc. The resolution of some TEM achieves a subatomic level, allowing the determination of positions (in 3D space) of individual atoms in the cluster.

The first transmission electron microscope was built by Ruska and Knoll in 1931 [93]. TEM microscope applies the same principle as the convenient optical microscope, but instead of light, it uses electrons. Using electrons allows obtaining smaller de Broglie wavelength (compared to the light) that results in a higher resolution. During TEM analysis, a high-energy electron beam penetrates a very thin “electron transparent” specimen. The electrons that pass through the sample are focused to form an image, registered on an imaging detector.

TEM is often accompanied by an energy-dispersive X-ray (EDX) spectroscope. The principle of EDX spectroscopy is similar to XRF. The only difference is in the case of EDX, the electron ejection is caused by the electron beam used (instead of X-rays).

1.3.5 Basics of computational simulations:

Computational simulations and calculated diffraction patterns described in the thesis were obtained using Cluster software [59] available for download at <http://kaszkur.net.pl/program-cluster/>. This program allows creation of mono- and bimetallic FCC clusters with different morphology (cuboctahedrons, decahedrons and icosahedrons) and structure (alloys, core-shells and Janus particles).

Although Cluster creates classical shape DEC (built up shell by shell), this configuration does not correspond to the most stable shape [51]. To convert classical decahedron into Marks DEC, 3D graphical software was used. The initial DEC's were created in Cluster, then were exported, and

modified in Blender, followed by sending them back to Cluster (as “xyz” files) for further calculations. The same approach was used to separate DECs into domains and merge CUBs into one cluster (Chapter 3.1).

Cluster was originally designed to assist pXRD simulations of metal clusters, consisting of (tens of) thousands of atoms. Therefore, the interaction between particles is characterized by n-body Sutton-Chen potential [58]: the attractive part is proportional to the square root of the sum of power functions, and the repulsive interaction is proportional to a sum of power functions of interatomic distances. The potential parameters are tuned to closely fit cohesive energy, surface tension, elastic constants etc. of the bulk material. This potential scheme follows the tight binding methods and offers realistic results for metals that may be relatively quickly computed. The results are comparable to other semi-empirical schemes like Embedded Atom Method [94], Gupta potentials [95] or Rosato, Guillope, Legrand (RGL) potentials [96].

For the atomic simulations, two approaches were applied: energy minimization and molecular dynamics (MD). Typically the energy relaxation was performed until the total energy gradient reached $\sim 10E-6$. The duration and conditions of MD are specified in each case separately.

The calculation of pXRD and SAXS patterns was based on the Debye summation formula [97]:

$$I = \sum_m \sum_n f_m f_n \frac{\sin qr_{mn}}{qr_{mn}} \quad 14$$

where I is the resulting scattered intensity; f_m and f_n are atomic scattering factors; r_{mn} is interatomic distance.

Elastic strain analysis (Figure 16 and Figure 18) of simulated models was performed by OVITO software [60]. This analysis determines the imaginary strain-free vector of the ideal FCC crystal structure and compares it with the elastically strained model. The transformation tensor (from ideal to strained models) represents information about deformations.

2 Experimental and methodology section

2.1 NPs synthesis

The thesis describes three concepts: multidomain XRD approach, vacancy driven twinning, and phase separation / segregation in bimetallic samples. Each concept requires specific samples and experiments. Therefore, in order to make the distinction between the samples clearer, they were divided into groups. Each group corresponds to one specific sample that has either been treated at high temperature in various gas environments or has been exposed to ex-situ/in-situ laboratory/synchrotron X-rays.

2.1.1 Group 1 Au@PVP

This group of NPs was synthesized based on the Tsunoyama and Amri recipes [98, 99].

The following reagents and materials were used: HAuCl₄*3 H₂O (99.9%, Alfa Aesar), PVP K 30 (40 kDa, Carl Roth), NaBH₄ (99%, Sigma-Aldrich), the dialysis bag with a cut-off size of 100–500 g.mol⁻¹ (spectra/Por® Biotech); Milli-Q Advantage system from Merck (Poland) to obtain Milli-Q water (resistivity 18.2 MΩ x cm at 25°C)

Before the synthesis, the dialysis bag was filled with 2 g of PVP K 30 dissolved in 20 ml of Milli-Q water. Then the bag was placed in a glass beaker filled with Milli-Q water and kept under the moderate stirring for 8 days. The water was exchanged eleven times, approximately every 17 hours.

Two identical PVP aqueous solutions were prepared: 7.17 ml of dialyzed PVP was diluted in 22.8 ml of H₂O and cooled in an ice bath for 30 min. Then the first PVP solution was mixed with 9.25 ml of HAuCl₄ (25.4 mM) and kept under moderate stirring in an ice bath for another 30 min. Five minutes before the reduction reaction, the second PVP solution was mixed with 40 mg of NaBH₄ and cooled in an ice bath.

The reduction agent was quickly injected into the precursor solution. To get rid of sodium and chloride ions, the solution was placed in the dialysis bag immersed into Milli-Q water (buffer to sample volume ratio was 100:1). The buffer was exchanged three times after 3, 5 and 24 hours of cleaning. Then, the sample was dried at <30°C at pressure <90 k Pa.

The completeness of ions removal was monitored by XRF and XRD (no NaCl peaks).

2.1.2 Group 2 Au@PVP@SiO₂

This group of NPs was synthesized based on the Tsunoyama and Dahlberg recipes [98, 100].

The following reagents and materials were used: HAuCl₄*3 H₂O (99.9%, Alfa Aesar), PVP K 30 (40 kDa, Carl Roth), NaBH₄ (99%, Sigma-Aldrich), NH₄OH (reagent grade, 25%, Chempur), 2-

propanol (99.7%, p.p.a. basic, POCH Basic), TEOS (reagent grade, 98%, Sigma-Aldrich), Magna Nylon membrane filter (0.22 μm), water was filtered and demineralized with ELIX system (Milipore).

To prepare the precursor solution, 0.717 g of PVP K 30 was dissolved in 21.6 ml of Demi water, mixed with 9.25 ml of 25.4 mM HAuCl_4 and stirred for half an hour in an ice bath.

To prepare the reduction agent, 0.717 g of PVP K 30 was dissolved in 32 ml of Demi water and placed in an ice bath for 30 min. Then, 5 min before the reduction reaction, it was mixed with 55 mg of NaBH_4 and placed in an ice bath. After that, the reduction solution was quickly injected into the precursor solution.

To form SiO_2 stabilizing agent, the nanoparticles containing solution was mixed with 6.88 ml of NH_4OH and 100 ml of 2-propanol. After that, it was mixed with 3.72 ml of TEOS, which was dissolved in 87.72 ml of 2-propanol. To ensure the completion of silica polymerization the resulting solution was stirred for ~ 2 hours. Then, NPs were filtered, washed with water, and dried at $<30^\circ\text{C}$ at pressure <90 k Pa.

2.1.3 Group 3 $\text{Au}_{55}\text{Pt}_{45}@\text{SiO}_2$

This group of NPs was synthesized based on the Zhang and Dahlberg recipes [101, 102, 100].

The following reagents and materials were used: $\text{HAuCl}_4 \cdot 3\text{H}_2\text{O}$ (99.9%, Alfa Aesar), $\text{H}_2\text{PtCl}_6 \cdot 6\text{H}_2\text{O}$ (99.9%, Alfa Aesar), PVP K 30 (40 kDa, Carl Roth), NaBH_4 (99%, Sigma-Aldrich), NH_4OH (reagent grade, 25%, Chempur), 2-propanol (99.7%, p.p.a. basic, POCH Basic), TEOS (reagent grade, 98%, Sigma-Aldrich), double-distilled (redistilled) water, Magna Nylon membrane filter (0.22 μm).

The precursor solution was prepared according to the following procedure: 548 ml of 0.396 mM H_2PtCl_6 was mixed with 548 ml of 0.484 mM HAuCl_4 and stirred for 5 min. Then, 2200 ml of 22 mM (monomer units) aqueous PVP solution was added and stirred for half an hour in an ice bath.

Then, 363 ml of 33 mM NaBH_4 was prepared 5 min before the reduction reaction and placed in an ice bath. Thereafter, the reduction solution was slowly added to the precursor solution and stirred for one hour. The product was dried in a rotary evaporator.

To form SiO_2 stabilizing agent, the nanoparticles containing solution was mixed with 8.16 ml of NH_4OH and 234 ml of 2-propanol. After that, it was mixed with 4.34 ml TEOS, which was dissolved in 104 ml of 2-propanol and 1742 ml of water. To ensure the completion of silica polymerization, the resulting solution was stirred for ~ 2 hours. The product was dried in a rotary evaporator.

Then the colloidal NPs solution was mixed with 210 ml of 2-propanol, filtered and washed with 2-propanol. The filtered NPs were dried at a temperature below 30°C at pressure below 90 k Pa.

2.1.4 Group 4 Au@C

This group of NPs was synthesized based on the Turkevich and Grabar recipes [103, 104].

The following reagents and materials were used: $\text{HAuCl}_4 \cdot 3\text{H}_2\text{O}$ (99.9%, Alfa Aesar), Vulcan XC 72 (Cabot Corporation), NaBH_4 (99%, Sigma-Aldrich), 2-propanol (99.7%, ppa, Stanlab), trisodium citrate dihydrate ($\text{Na}_3\text{C}_6\text{H}_5\text{O}_7$, ppa, Chempur), double-distilled water, Magna Nylon membrane filter (0.22 μm).

To prepare a solution of the gold precursor 17 ml of 4% wt. $\text{Na}_3\text{C}_6\text{H}_5\text{O}_7$ was diluted in 1725 ml of double-distilled H_2O , then mixed with 20 ml of 25.4 mM HAuCl_4 and vigorously stirred. To prepare the reduction agent solution, 15 mg of NaBH_4 was dissolved in 17 ml of 4% wt. $\text{Na}_3\text{C}_6\text{H}_5\text{O}_7$.

Then, 5 min before the reduction reaction, 400 mg of Vulcan XC 72 was added to 85 ml of 2-propanol and water mixture (3:1 volume ratio) under sonication. After mixing the precursor and reducing solutions, the carbon suspension was added. The resulting solution was stirred for ~2 days in darkness. Then, NPs were filtered, washed with water and dried at $<40^\circ\text{C}$ under vacuum.

2.1.5 Group 5 Au₅₅Pt₄₅@C

This group of NPs was synthesized based on the Wanjala, Luo and Chen recipes [41,72 ,105].

The following reagents and materials were used: $\text{HAuCl}_4 \cdot 3\text{H}_2\text{O}$ (99.9%, Alfa Aesar), $\text{H}_2\text{PtCl}_6 \cdot 6\text{H}_2\text{O}$ (99.9%, Alfa Aesar), Vulcan XC 72 (Cabot Corporation), NaBH_4 (99%, Sigma-Aldrich), Octadecylamine (97.9%, Alfa Aesar), 2-propanol (99.7%, ppa, Stanlab), Chloroform (>98.5%, Chempur), double-distilled water, Magna Nylon membrane filter (0.22 μm).

To prepare the precursor solution, 4.88 ml of 0.126 M HAuCl_4 was mixed with 4.88 ml of 0.0965 M H_2PtCl_6 . Then the precursor solution was mixed with 0.44 g of octadecylamine (ODA) and dissolved in 190 ml of 2-propanol.

Then 0.488 g of NaBH_4 was dissolved in 25 ml of H_2O . The reduction agent was slowly added to the precursor solution under vigorous stirring. The total stirring time was about 1 hour. The NPs solution was dried in a rotary evaporator followed by dissolving in 20 ml of chloroform.

To prepare the carbon supporting material 0.4 g of Vulcan XC 72 was suspended in 100 ml of chloroform and sonicated for ~1 hour at room temperature. After that, the carbon suspension was mixed with NPs solution under sonification, followed by stirring overnight. Then AuPt@C NPs were filtered, washed with water and dried at 60°C under vacuum.

2.2 Experimental setups

2.2.1 XRD

For all XRD measurements (ex-situ and in-situ) a Siemens D5000 diffractometer was used. All diffraction patterns were recorded in Bragg-Brentano θ - 2θ geometry with a continuous scanning rate of 0.02° per second per step for a data acquisition time. Cu lamp (PANalytical[®]) was operated at 40 mA and 40kV and was equipped with a 10-20 μm filter to limit K_β radiation. Scattered X-rays were detected by a Bruker[®] LynxEye strip detector (192 stripes). The sizes of the fixed divergence and anti-scattering slits were 1 and 2 mm, respectively. The Soller slits divergence was equal to 5° . All XRD patterns were analyzed in program Fityk [106].

2.2.2 TEM

For the TEM measurements, a FEI Talos F200X microscope operated at 200 kV was used. Energy dispersive X-ray spectroscopy (EDX) analysis was performed using a Super-X system with four silicon drift detectors. All TEM figures were analyzed in program ImageJ [107].

2.2.3 XRF

The elemental compositions of all samples were analyzed by X-Ray Fluorescence Spectroscopy (XRF). For XRF analysis a PANalytical MiniPal 4 PW4030/45B energy dispersive spectrometer was used.

Rh tube was used as primary X-ray radiation source and operated at a maximum voltage of 30 kV. Scattered X-rays were detected by a semiconductor Silicon Drift Detector.

Powder samples were placed in plastic cylindrical containers with bottom made of Proline[®] 4 μm foil (PANalytical). The spectra include some typical impurities at the PPM level: Ca, P, Fe, Al, Ti, Cu, Zn, and Ni, originating from the scattering background. Therefore, if one of these elements was detected and its amount did not exceed 1%, this element was considered as the background..

XRF spectra analysis was performed using the PANalytical MiniPal software. Samples were characterized using the Minipal standard library and quantification procedure.

2.2.4 Ex-situ measurements

For ex-situ experiments a quartz U-shaped reactor (Volume ~ 12 ml) was used (Figure 11). A thermocouple (CZAKI, TP-201, NiCr-NiAl (K) kl.1) was placed in a quartz capillary, which was immersed into NPs bed. Temperature was controlled with a Cole-Parmer Digi-Sense R/S (Model

89000-10) device. Before each measurement, the thermocouples were calibrated in an ice bath using laboratory thermometers.

After checking the tightness, the quartz reactor was purged with various gases. Gas flow control was carried out by a MKS multi gas controller 647C. The following gases were used: He (99.999%, Multax), O₂ (99.999%, Multax), CO (99.997, Linde), N₂ (99.999%, Multax). Each time before measurements, the actual velocity of the outgoing gas flow was measured.

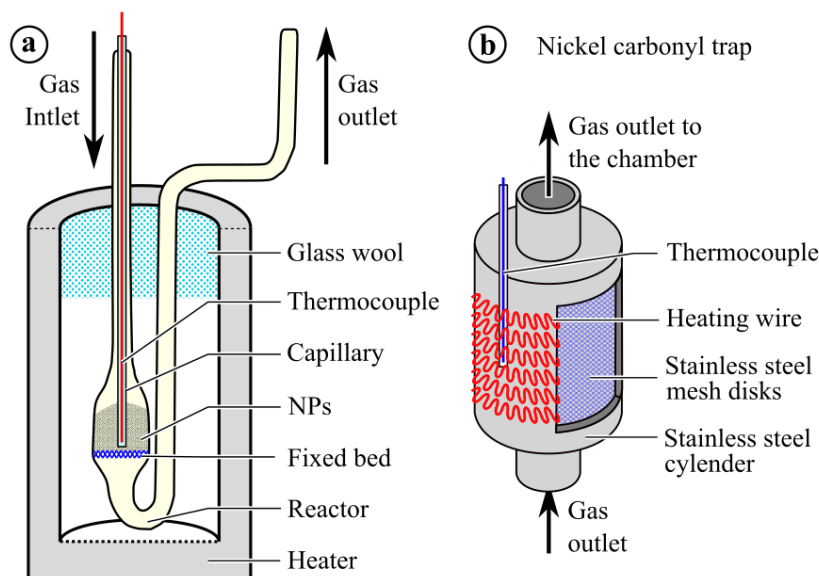


Figure 11 a) Scheme of setup for ex-situ heating experiments b) principle scheme of a nickel carbonyl trap

The biggest disadvantage of ex-situ measurements is that it is not possible to measure kinetic parameters of various diffusion phenomena. In other words, only initial (before heating) and final (after heating) states of the sample can be measured. Meantime, the most attractive advantage of this approach is the straightforwardness of the analysis. After removing the sample from the reactor after a short period of time, its temperature is stabilized at room temperature (RT). Thus, the obtained XRD pattern does not require temperature corrections, in contrast to in-situ tests. In addition, one can be sure that a sample holder is not tilted or/and somehow displaced from its original position (as opposed to in-situ). These features allow a direct comparison of XRD patterns of samples after temperature treatment.

Despite the high purity of CO, during long-time exposure experiments (weeks), the problem of sample contamination becomes important. Additional difficulty arises due to corrosion of stainless steel caused by CO. This corrosion creates iron and nickel carbonyls [108], which decompose relatively easily. As the result, the original sample will be contaminated / poisoned by Ni and Fe. To prevent this, we designed a special carbonyl trap (Figure 11 b). It is a stainless steel cylinder filled out with stainless steel mesh disks. The cylinder was heated up to $\sim 200^{\circ}\text{C}$, to decompose all

carbonyls before they entered the reactor. This trap was used in both ex-situ and in-situ experiments.

To control contamination, all samples after long-time experiments were analyzed by XRF for the presence of Ni and Fe ions. All experiments presented in the Results and discussion chapter showed Ni/Ir contaminations at the level of the background.

2.2.5 In-situ measurements

As mentioned earlier, an in-situ XRD chamber allows to measure kinetic aspects of various phenomena. However, this approach has some difficulties, which will be discussed below. A principal scheme of the in-situ chamber used in all in-situ tests is shown in Figure 12.

2.2.5.1 Setup

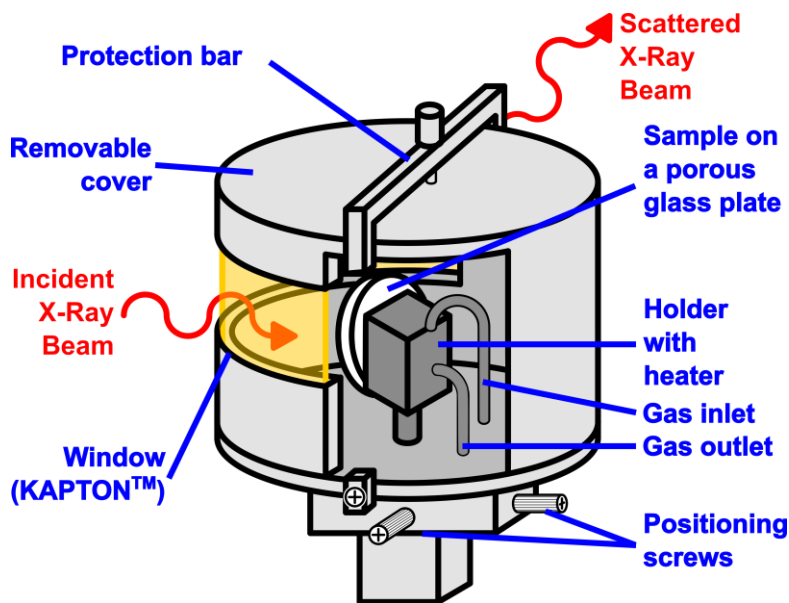


Figure 12 The scheme of the heating chamber for in-situ XRD measurements. Reprinted with permission from the author –Ph.D. Maciej Zieliński

At the center of the in-situ setup there is a heating block with a kanthal heating wire and a thermocouple inside. A built-in thermocouple is used to monitor the actual temperature of the heater. At the top of the heating block there is a spring, that is used to attach a porous glass disk / plate to the heater. Behind the block there are pipes that serve as an inlet and outlet for gases. The described above setup is covered by a removable aluminum cup (cover) with a special window cut in the middle. To avoid gas escape through the window, it was closed by a Kapton foil, which is

transparent for the X-rays. Since the chamber is airtight, this allows for good control of the atmosphere inside the chamber. Prior to each in-situ test, the chamber was checked for leaks.

To prepare a sample for measurements, a certain amount of powder (typically 50 mg) was poured onto a porous glass and then pressed tightly with a glass plate. If obtained bed was uniform, smooth and adhered well to the porous glass, it was mounted on the heating block.

The built-in thermocouple indicates a temperature on the heating block, but not the actual temperature of the sample. The porous glass plate has a thickness of 0.5 – 1 mm, and the thermal conductivity of silica is not high. Therefore, the temperature of the sample (pressed on a porous glass) is always lower than that of the heating block. To compensate for this gradient, additional calibrations were performed. Before each experiment, a separate thermocouple was attached to the porous glass and a growth of the gradient with temperature was measured. Then this difference was taken into account when setting the temperature of the heating block. Since a sample bed thickness is in the order of tenths of a millimeter, we assume that the temperature of the sample is equal to the temperature of a porous glass.

2.2.5.2 Misposition corrections

Assuming that the heating block and porous glass expand evenly (without twisting), the sample bed displacement can simply be considered as a shift of the goniometer axis. In some cases, it can be difficult to accurately determine the magnitude of the specimen displacement. Therefore, another calibration step was carried out: an internal standard (polycrystalline quartz) was added to the sample layer.

Quartz is a highly crystalline material with narrow and intense diffraction peaks and with well-defined parameters. Its coefficient of thermal expansion is known, therefore it is possible to calculate the reference positions of quartz diffraction peaks (θ_{ref}) at a given temperature. Then, by comparing the difference between the observed and reference quartz peaks ($\Delta\theta_{obs}$), one can analyze the displacement of the sample (Δ_R) relative to the goniometer rotation axis:

$$2 \Delta_{2\theta_{obs}} = 2 * \frac{\Delta_R}{R} * \cos \theta_{obs} * \frac{180}{\pi} \quad 15$$

where R – is a goniometer radius; θ_{obs} – is the quartz peak position in the experimental sample pattern. Once Δ_R was found, the entire diffraction pattern was modified ($\Delta\theta_{mods}$):

$$2\theta_{mod} = 2\theta_{exp} - 2 * \frac{\Delta_R}{R} * \cos \theta_{obs} * \frac{180}{\pi} \quad 16$$

The thermal expansion coefficient of quartz (CTE_{quartz}) was taken from the literature [109]. To obtain the lattice constant (l.c.) of heated quartz (l_{heat}) the following equation was used:

$$l_{heat} = l_{ref} + l_{ref} * CTE_{quartz} * Temperature \quad 17$$

Once the new heated lattice constant has been found, the position of its peak can be calculated from Bragg's law, allowing the sample displacement factor to be determined (equation 15). The procedure described above was performed automatically and applied to each individual scan. This was done with a custom lua script written for Fityk.

2.2.5.3 Temperature expansion corrections

In-situ XRD assumes that measured diffraction patterns are collected at different temperatures, thus they cannot be compared directly, because at different temperature there will be different lattice constants. Therefore, it is necessary to reduce all obtained data to certain common condition– room temperature (RT). In the case of an alloyed bimetallic sample (Au-Pt), it's important to know the ratio (concentration μ) of metals, that can be found by using the Vegard's law:

$$l_{exp} = l_{ref Au} * \mu_{Au} + l_{ref Pt} * \mu_{Pt} \quad 18$$

To use this equation, the effect of thermal expansion must be taken into account. All lattice constants (references and experimental) should be considered at the same temperature. Data on the thermal expansion of Au and Pt were taken from the literature and approximated by polynomial equations [110, 111]:

$$l_{Au} = 9.89922819E-09 * T^2 + 0.0000571646551 * T + 4.07424335 \quad 19$$

$$l_{Pt} = 6.03021978E-09 * T^2 + 0.0000343839835 * T + 3.92366973 \quad 20$$

Using these equations, reference lattice constants at various temperatures can be calculated. The next step is to rearrange equation 18 to obtain the molar fraction of one of the metal, which enables calculation of the ratio between the components:

$$\mu_{Au} = (l_{exp} - l_{ref Pt}) / (l_{ref Au} - l_{ref Pt}) \quad 21$$

Knowing the ratio of metals, one can find the experimental value of the lattice constant at room temperature. The first step is to calculate the reference lattice constants at RT (equations 19 and 20). Then, by applying the Vegard's law (equation 18) the l_{exp} at RT value can be found.

2.2.6 Synchrotron X-ray exposure

Synchrotron measurements were performed at the brand-new beamline P62 SAXSMAT at the synchrotron PETRA III at DESY / Hamburg. Small-angle scattering (SAXS) diffraction signals were recorded using an "Eiger2 X 9M" in-vacuum detector having CdTe sensors, while wide-angle scattering (WAXS) signals were recorded using an "Eiger2 X 4M" detector. Scattering in both ranges was recorded simultaneously. All SAXS patterns were analyzed in program SASfit [112].

A stainless steel metal bar (~1mm thick) with a hole in the center was used as a sample holder. The sample was placed in the hole and fixed with ordinary adhesive tape on both sides so that the powder would not crumble. Then all the metal bars were mounted on a special stage and placed in a sealed chamber with an X-ray transparent window. To reduce air scattering, this chamber was filled with helium.

3 Results and discussion

3.1 MDXRD

It has been known for more than 30 years that the diffraction patterns of CUB, ICO and DEC are different (Figure 2) [35,113]. However, the exact nature of these differences is not well described. The current interpretation of the phenomenon originates from the work of Patterson [114], which was later improved by Warren and Warekois (see Chapter 1.1.2) [115]. According to them, stacking and twinning faults may appear with a certain probability, leading to the creation of new interatomic distances that differ from an ideal FCC structure. This idea was further developed by Longo and Martorana [64]. Assuming a difference in the probabilities of defects appearance, that leads to a change in interatomic distances distributions, various XRD patterns were calculated (using the Debye equation). Interestingly, the calculated XRD diffraction patterns were in good agreement with experimental data.

This approach seems to be universal, however it is only a phenomenological description of the twinning effect and some important aspects are neglected. First of all, while using the Warren approach, researchers usually consider the low probabilities of twinning, which limits the applicability of the method. Secondly, the exact physical meaning of the “probabilities” of twinning is not clear. I.e. if a sample contains 2% of stacking faults and 3% of twin planes, what would be the physical model of a such structure? Finally, the new interatomic distances appear with a certain distribution, which obeys a certain dependence predicted by Warren. This dependence is purely theoretical and is not substantiated by a suitable atomistic model. The extended Longo and Martorana approach seems to be more realistic, but it takes into account twinning along one direction (1D). Meanwhile, in nature, twinning occurs in 3D, when complex cross-twinning (as in ICO) can occur.

Nevertheless, Warren’s approach describes two principal effects of twinning: a change in the ratio of heights and a shift of diffraction peaks [116]. This approach considers the defects at the unit cell level, followed by scaling the changes to macrolevel. However, the twinning effect can also be described by considering a row of atoms at the level of nanoparticle sizes. Using extensive computational modeling of multiply twinned particles, we have developed the multidomain XRD (MDXRD) method. In contrast to the Warren’s approach, the MDXRD can be applied to highly defective structures, and provides a physically meaningful outcome.

3.1.1 Twinning effect

One of the twinning effects is a change in the ratio of diffraction peak heights. This effect can be predicted analytically. The scattering intensity (I) of an unpolarized beam from a single crystal can be described as:

$$I = I_e F_{hkl}^2 \sum_i \frac{\sin^2(N_h x_h)}{\sin^2(x_h)} \frac{\sin^2(N_k x_k)}{\sin^2(x_k)} \frac{\sin^2(N_l x_l)}{\sin^2(x_l)} \quad 22$$

,where I_e is the intensity of X-ray scattering by a single free electron (Thomson scattering equation); F is the structure factor; hkl are Miller indices; N – number of unit cells in a given direction.

The maximum intensity (I_{\max}) of scattering can be observed when the phase angle x equals π (Figure 13) and the Laue equations are simultaneously satisfied (Chapter 1.3.1). The I_{\max} parameter can be considered as the height of the diffraction peak. This assumption allows to transform the intensity I from equation 22 into the height (H). In addition, equation 22 can be simplified by assuming that the Miller indices are equal to 001 (equation 23) and summation in this direction is done over all (not necessarily equal in length) rows of atoms. This equation can be used to analytically describe the origin of the twinning effect:

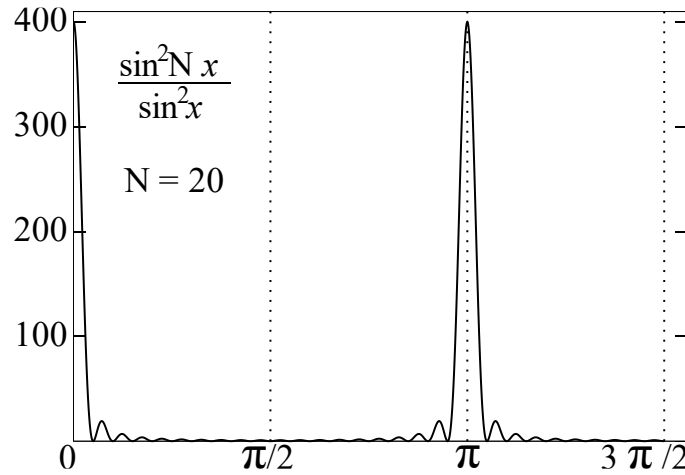


Figure 13 The function $(\sin^2 Nx)/\sin^2 x$ for $N=20$.

$$H = F_{00l}^2 \sum_i \frac{\sin^2(N_i \pi l)}{\sin^2(\pi l)} = F_{00l}^2 \sum_i N_i^2 \propto F_{00l}^2 \sum_i P_i^2 \quad 23$$

where P_i is the length of row i of atoms along $[00l]$ direction. The easiest way to create a twin plane is to merge two CUB by their (111) planes (Figure 14 a). A single CUB has eight equal $[111]$ directions perpendicular to the corresponding (111) planes. Therefore, it is obvious that the merging of CUBs resulted in aligning $[111]^*$ and $[111]^\#$ directions, which led to the creation of one common $[111]^4$ direction. This extended direction has almost twice as many atoms as in the original CUB model (excluding merged (111) plane atoms).

Using the directional XRD pattern function embedded into the CLUSTER program, one can simulate an enhancement of the diffraction peak height because of the twinning. Figure 14 **d** shows that the height of the diffraction peak calculated along $[111]^4$ direction is ~ 3.895 times higher than that of the regular $[111]^{1-3}$ directions. If the original and merged CUBs contain 2057 and 4069 atoms respectively, the calculated by equation 23 enhancement equals 3.913. This calculated value is greater than the result of computational simulation because twinned model contains elastic strains affecting alignment of $[111]^*$ and $[111]^\#$ directions.

The packing of atoms in crystalline structures follows strict rules, whereby the aligned atoms form rows, and the total number of atoms is proportional to the length of the rows of atoms. This assumption allows us to simplify the twinning model and consider not the number of atoms, but only the length of the rows. Since the twin plane atoms are shared by both CUBs (yellow and brown domains), the regular $[111]^*$ and $[111]^\#$ directions have the same column length (Figure 14 **b**; 3 layers), while extended $[111]^4$ length is nearly double of this value. However, because of stacking periodicity and not symmetrical shape of the crystal, is it difficult to predict when this value is doubled, when it is not.

Nevertheless, the height increase due to a twinning can be calculated by looking at the cross-section of the merged model (Figure 14 **e**). For the single CUB with 2057 atoms the average length of $[111]$ direction is 4.55 atoms. The length of the averaged extended row is 8.93. Then, according to equation 23, the enhancement will be equal 3.85, which is close to the previous results. This proves applicability of considering the rows of atoms instead of the number of atoms. The calculated value is less accurate because of complex variation of the length of rows.

To analyze the net twinning effect on powder XRD patterns, all $[111]$ directions must be taken into account. For a regular single CUB the multiplicity of 111 peak equals 8 and all directions are equal. The twinned model of two cuboctahedrons (Figure 14 **a**) is more complicated: it has two extended ($[111]^4 * 2$) and $6 * 2$ initial short column directions ($[111]^{1-3} * 2$). The resulting height of the 111 peak is equal to the sum of intensities in all directions related to multiplicity of the reflection. Therefore, the height of 111 peak of twinned CUBs ($H_{M.CUB}$) will be higher than the same peak in case of two separated CUBs ($H_{2.CUB}$), wherein the number of atoms in both cases is approximately the same! If the length of the extended row (P_{ext}) is $(8.93 / 4.55)$ 1.96 longer than regular rows (P_{reg}):

$$\frac{H_{M.CUB}}{H_{2.CUB}} = \frac{F_{00l}^2 (2 * 6 P_{reg}^2 + 2 P_{ext}^2)}{F_{00l}^2 (2 * 8 P_{reg}^2)} = \frac{12 P_{reg}^2 + 2 * 3.92 P_{reg}^2}{16 P_{reg}^2} = 1.245 \quad 24$$

This result is in a good agreement with the computational simulations (Figure 14 **c**), where the 111 peak height of the twinned model was 1.2 times greater than the height of two separated CUBs. It is likely, that the difference of these two values is caused by the misalignment of $[111]^*$ and $[111]^\#$ rows of atoms (Figure 14 **e**). Shifts of atoms from their nodal positions appeared after the relaxation of the merged CUBs model. This effect is rather weak and does not noticeably affect other reflections.

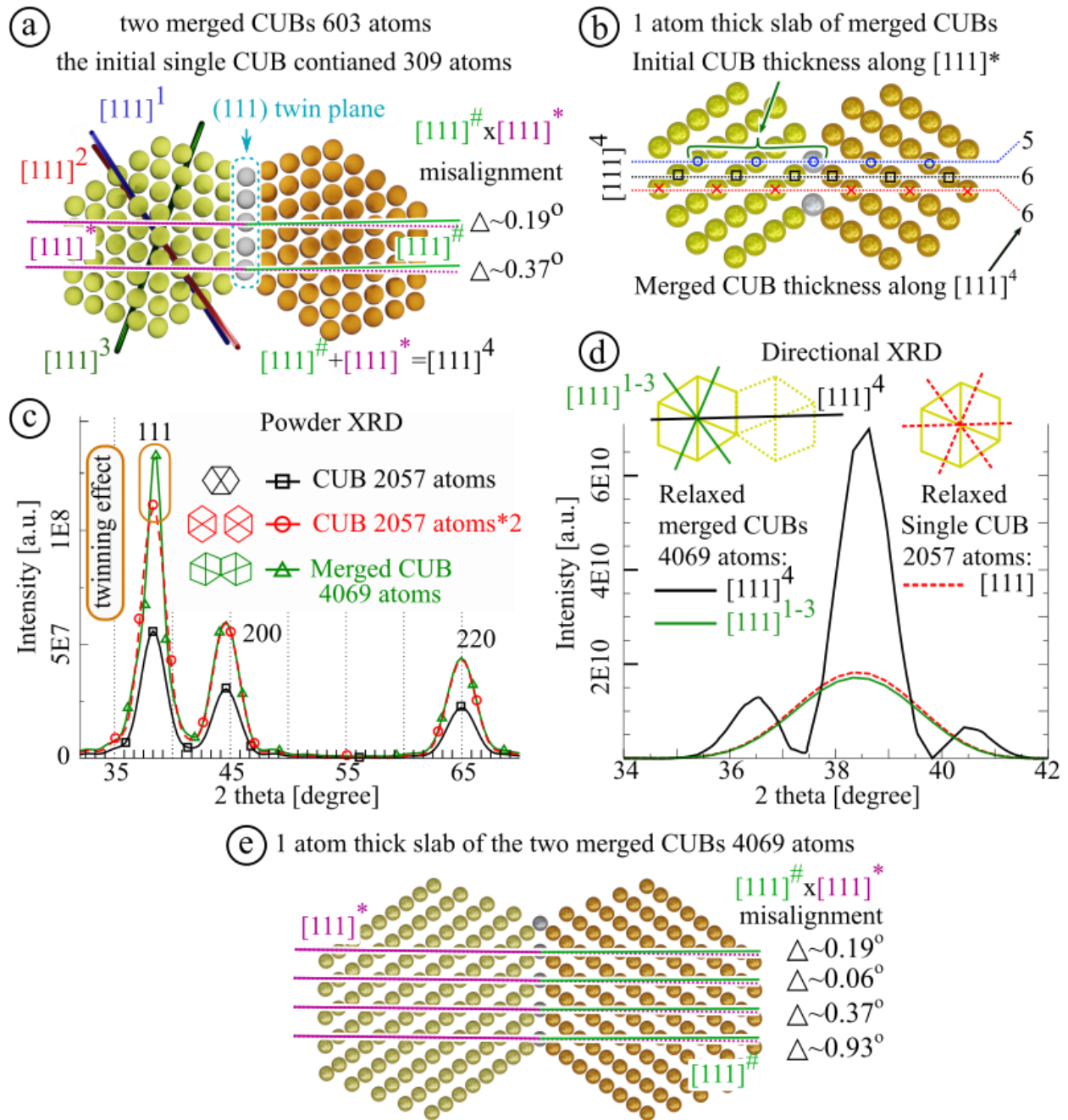


Figure 14 a) Two gold CUBs (shown in yellow and brown colors) joined by a (111) plane, view along $[-110]$. The initial single CUB consisted of 309 atoms. After joining, the resulting twinned model contains 603 atoms (the twin plane consist of 15 atoms); b) Slab of the conjoined CUBs model, demonstrating a change in the length of rows of atoms along the $[111]^4$ direction; c) Comparison of calculated pXRD patterns of the regular Au CUB, the same regular Au CUB multiplied by 2 and conjoined CUBs; d) Calculated directional XRD patterns of twinned CUB model along short $[111]^3$ and extended $[111]^4$ directions (green line and black lines, respectively) and regular CUB along the $[111]$ direction; b) Slab of the merged CUBs containing 4069 atoms.

3.1.2 Domain approach

The analytical prediction of the twinning effect (based on equation 23) is only possible for models with a regular shape and few twin planes. The more complex the model, the less applicable this approach. The appearance of twin planes changes not only the height of the diffraction peak, but also results in formation of elastic strains. Both effects can be visualized by analyzing the decahedron structure.

DEC can be separated into five equal FCC pieces (Figure 15 a) only if the central row of atoms is excluded. The DEC domains were cut off from the relaxed model, therefore they contain elastic strains representative of the entire model.

To focus on the twinning effect alone (neglecting strains), the single DEC domain (ideal FCC structure) XRD pattern was multiplied by 5 and compared with the initial DEC XRD pattern. As can be seen from Figure 15 a, the 111 peak of DEC is 1.43 times higher (and narrower) than the peak of the same size single DEC domain. Some other diffraction peaks (311 and 420) are also affected by twinning. However, these peaks lie at high angles more difficult to analyze. This makes them less attractive for practical use.

One can notice that the enhancement of 111 peak height is more intense for the DEC than for merged CUBs (1.43 vs 1.2). The principal difference between these two models is the number of twin planes: 5 vs 1. This difference arises from the fact that each twin plane contributes to the growth of the 111 peak height. Nevertheless there are peaks whose profile remains constant regardless of twinning (200, 220, 400, 331 ...). Comparison of the affected (111) and not affected (200 or 220) peaks allows estimation of the number of domains in the cluster.

Figure 15 b shows normalized diffraction patterns of the clusters with different number of domains: regular CUB (1 domain); non relaxed 1 – 4 domains structures (cut off from the relaxed DEC) and regular DEC (5 domains). Since all the patterns in Figure 15 b were normalized by scaling the 111 peak height to 100, the twinning effect is considered as a stepwise decrease in the height ratios of the not affected (220 & 200) to the affected 111 peaks. Scaling of 111 peak height is justified by the fact that in all XRD databases the 111 peak amplitude (for FCC metals) is equal to 100%.

All the features of X-ray diffraction patterns described above arise due to the mutual orientation of ideal FCC fragments. Therefore, we propose to use the following terminology: a domain – is an ideal FCC fragment without a twin plane. For XRD pattern, the contribution of atoms inside the domains dominates over the twin planes atoms. Therefore, to emphasize the fact that the analysis of NPs morphology is based on diffraction studies, the term “multidomain” NP is more adequate than “multiply twinned” one.

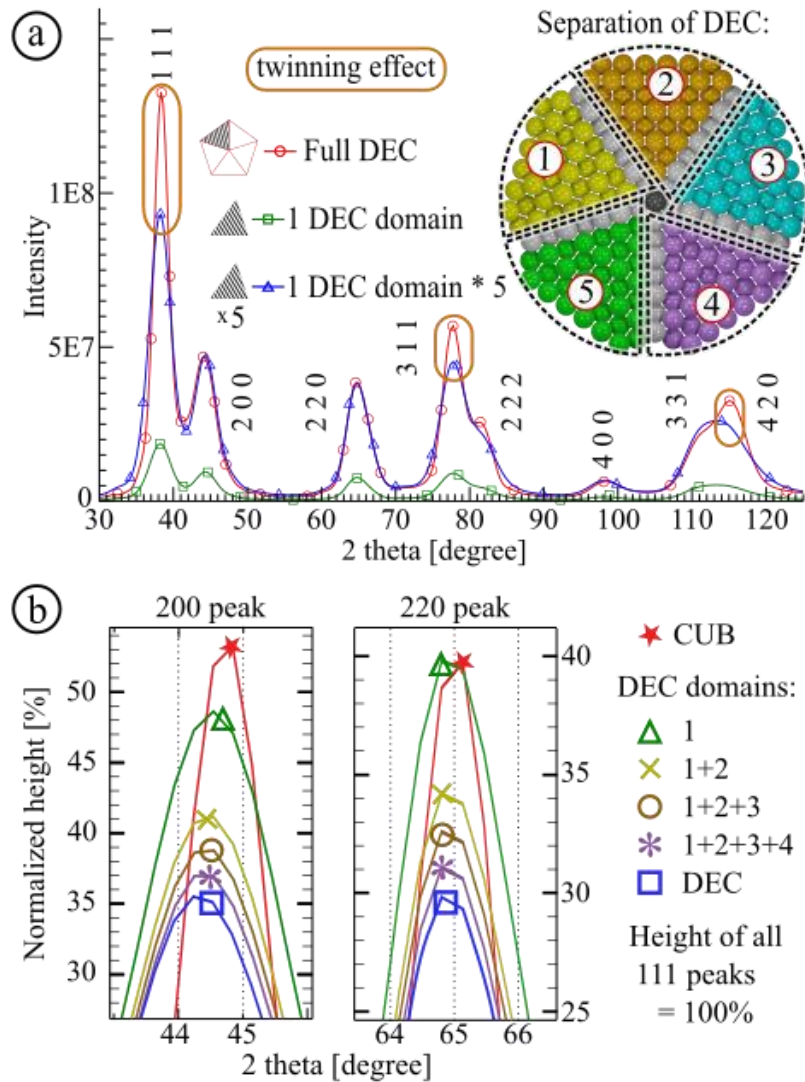


Figure 15) Calculated XRD patterns of the gold DEC domain (single and single * 5) and regular DEC. The initial DEC model (view along principal [220] axis) has 4772 atoms; the central row consists of 17 atoms. Twin plane atoms are shown in grey. b) Evolution of the 200 and 220 peak heights depending on the number of domains. Details of the DEC model and its domains can be found in Table 1.

3.1.2.1 Strain analysis: DEC

In the perfect DEC, the angle between two neighboring (111) planes should be equal 72° , while for ideal FCC domains this angle is only 70.53° [117]. Therefore, when five FCC units form DEC structures, there is always a 7.35° angle deficiency in the structure. It must be compensated by the appearance of defects or the formation of elastic strains (Figure 16 a). Using elastic strain calculator (OVITO program), it can be noticed that inside relatively small DEC, the lattice is mainly affected by contraction forces (negative volumetric strain values).

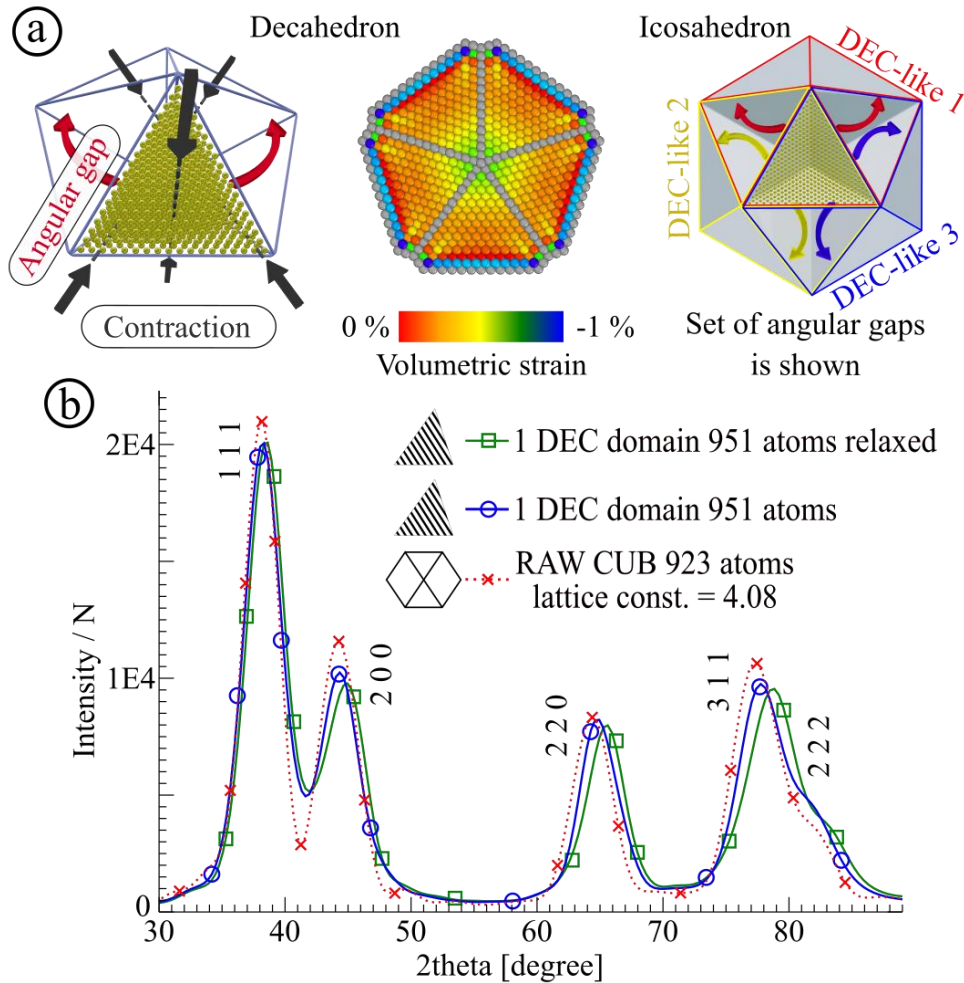


Figure 16 a) Schematic illustration of contraction forces acting on DEC because of the angular gap. The middle figure shows the volume strain distribution in 4772 atoms DEC (by OVITO). The right-hand side figure shows the directions of multiple angular gaps in an ICO; b) Comparison of calculated XRD patterns of the relaxed and non-relaxed single DEC domains with the non-relaxed CUB model having no gradients of the lattice parameter.

The result of the strain distribution analysis performed by OVITO can be independently validated by analyzing the single domain of DEC. Since strains are uniformly distributed in the DEC, each individual DEC domain has a representatively modified lattice. Comparing the diffraction patterns of non-relaxed CUB (the lattice parameter is constant) with that of a single DEC domain, one can evaluate the character of the straining.

As can be seen from Figure 16 b, all diffraction peaks belonging to the raw CUB model are shifted to the left-hand side compared to the single DEC piece. This means that the lattice parameters of the DEC's domain are smaller, what indicates presence of the contraction forces inside the DEC. This confirms the earlier conclusion that only contraction forces can be detected inside regular decahedral structures of small and medium sizes.

Apart from the elastic strains, diffraction techniques are sensitive to strains appearing because of stacking and twin faults (Chapter 1.1.2). This effect can be visualized by considering DEC

disassembly derivatives: one, two, three, four and five domain models. Models were taken as they are, without relaxation, in order to maintain the microstrain effect intact. It allows to focus exclusively on the strain effect (Figure 17 **a**). The more domains were taken, the more 111 peak position is shifted to the right, while 200 peak position is shifted to the left-hand side. These observations are consistent with Warren's description [115]. These shifts are a consequence of the new interatomic distances appearing because of the twinning.

Nevertheless, since DEC must include the angular gap, it can be monitored with the multidomain approach. The disassembly of the DEC with the subsequent relaxation of each structure allows to track down this effect (Figure 17 **b**). Relaxation is necessary to reduce local microstrains and optimize the models according to the number of domains.

Perfect twinning with no strain is impossible; even a simple model of two merged CUBs has a misalignment of rows of atoms (Figure 14). As can be seen from Figure 17 **b**, the increase in the number of domains (building up the DEC structure) leads to consequent lattice expansion, leading to the left-hand side shift of 111 and 220 peaks. Despite the relative expansion, the resulting lattice constant is still smaller than the bulk value (4.08 Å). It is interesting to note that the transition from 4 to 5 domains does not lead to a rapid growth of microstrains. This observation additionally supports the idea that each twinning contributes to the formation of elastic strains.

3.1.2.2 Strain analysis: ICO

A regular ICO consists of 20 spatially oriented domains. Each ICO domain can be considered as a part of three neighboring decahedron-like structures (Figure 16 **a**). Therefore, each segment is affected by “triple” angle deficiency from each side of the domain. As a result, the strains are so strong that the lower part of each domain (closer to the center) is strongly contracted, while the upper part (closer to the surface) gets strongly expanded (Figure 14).

It should be noted that near the central row of each DEC-like structure (central 220 row), the lattice constant is more uniform (“**a**” distances Figure 18 **b**), than in the bulk. Atoms located at the corners of a DEC-like structure are displaced from their nodal position: the lower part is contracted (“0.9 **a**” distance), while the upper part is expanded (“1.1 **a**” distance). Therefore, because of these two types of stains, the intensity of all peaks is decreased compared to the relaxed model. The 200 peak has the same intensity due to overlap with the broadened 111 peak.

A typical ICO XRD pattern (Figure 2) is rarely observed experimentally. This is probably due to the presence of a “double” lattice constant inside the ICO domains, which makes the existence of big ICO crystals (larger than 3-4 nm) unfavorable. The larger the ICO particle, the greater the total difference between contraction and expansion, so the particle becomes less stable.

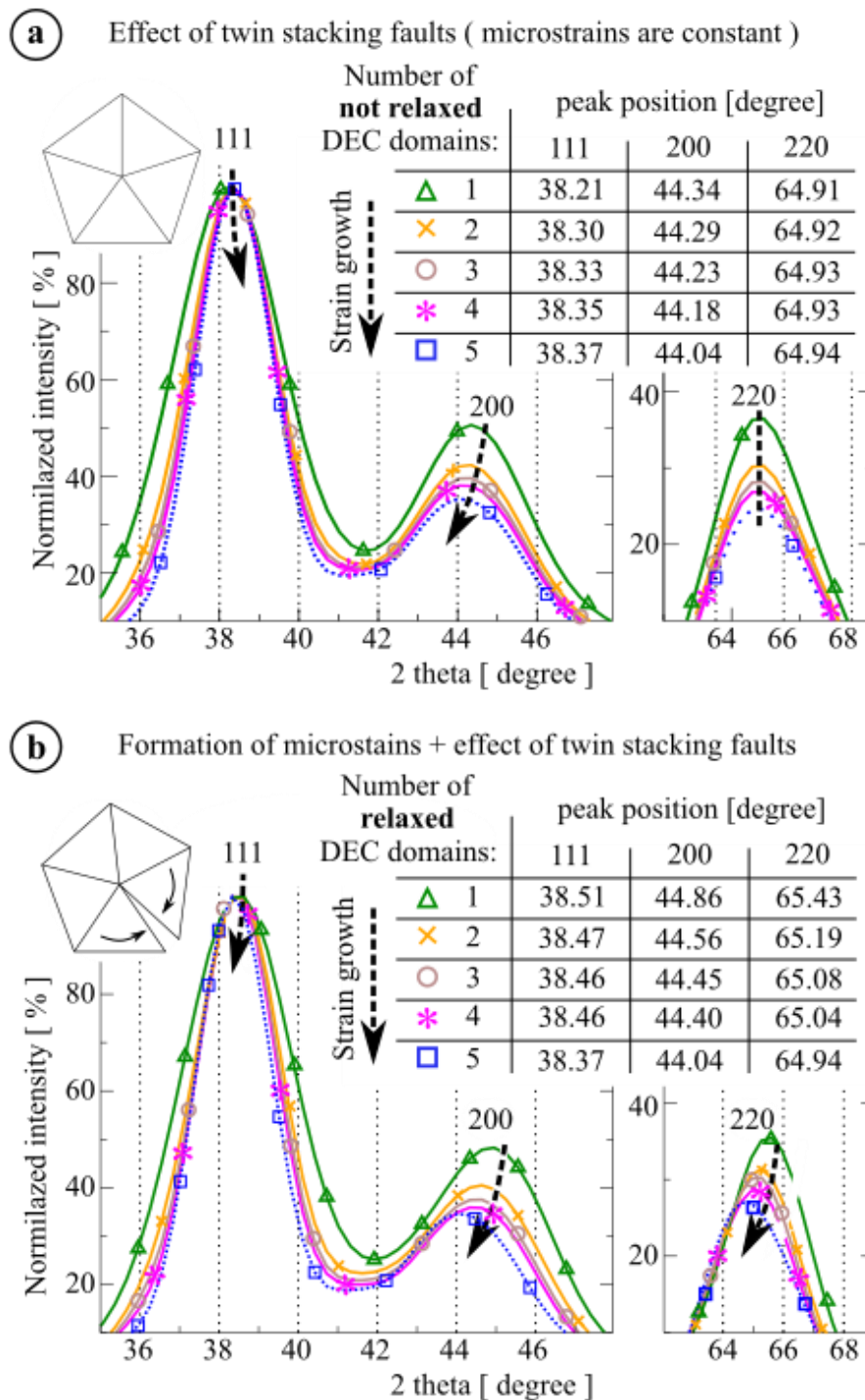


Figure 17 a) Calculated XRD patterns of 1-5 domain models cut off from the regular DEC consisting of 4772 atoms. The models were not relaxed, to preserve original DEC strains; b) Calculated XRD patterns of the same size models, but each model was relaxed, to reduce the microstrains.

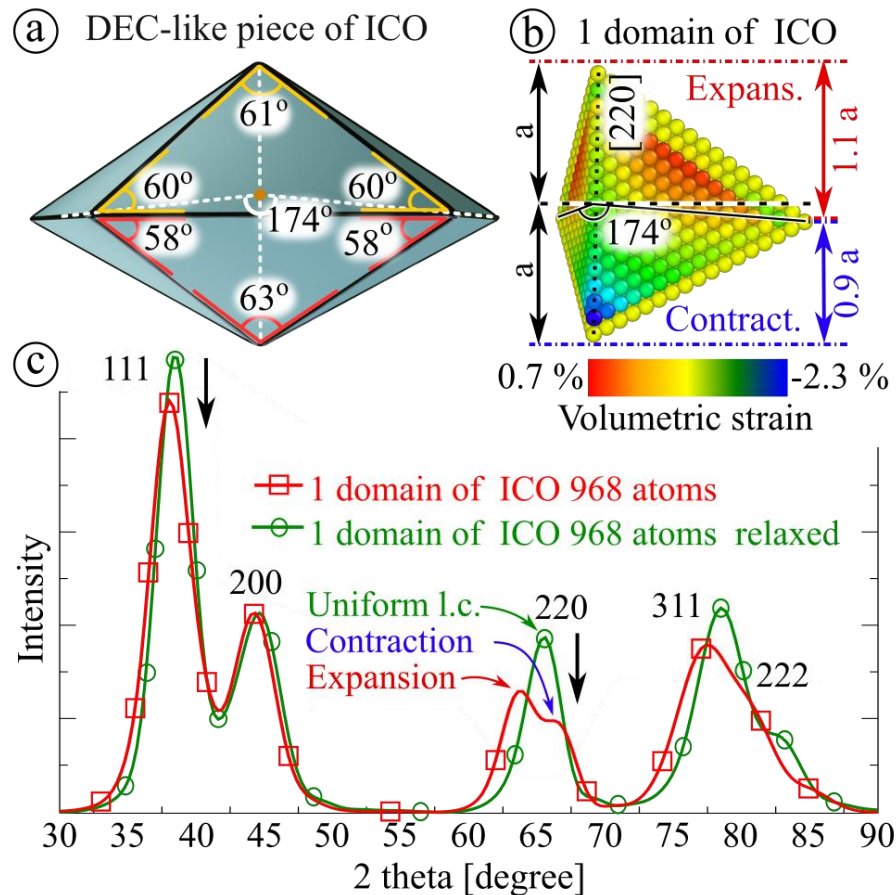


Figure 18 Illustration of the strain distribution in an ICO: a) change of optimal plane angles in DEC-like piece of ICO. The red angles correspond to the lower part of the cluster (close to the center of entire ICO), the yellow angles correspond to the upper part of the cluster; b) the volumetric strain distribution in one domain of ICO; c) comparison of the calculated XRD patterns of the strained and relaxed one domain of ICO (968 atoms). The influence of a “double lattice” parameter on the diffraction pattern can be seen from the 220 double peak.

3.1.2.3 Estimation of a single domain size

The appearance of twinning changes the width of diffraction peaks, which leads to a change in NP size estimation calculated by the Scherrer equation. This effect is shown in detail in Figure 19. The 111 peak width of the CUB (2057 atoms) is similar to the width of the five domain DEC (4776 atoms). Applying the Scherrer equation to these peaks, we obtain similar results: ~ 3.8 nm and ~ 3.9 nm, respectively. In fact, applying the Scherrer equation to any diffraction peak of the CUB model provides a result that is close to the actual value. This shows that the Scherrer size estimation is directly applicable for the analysis of single domain models. However, in case of DEC, the result is not correct. The estimation of the DEC size, according to the Scherrer equation, depends on the peak which was selected for the analysis: for 111 – 3.9 nm., for 220 – 2.7 nm, while the actual size equals 5.1 nm.

Comparing the simulated XRD patterns of the whole DEC and its one domain, one can see that the width of the 220 peaks of these two structures is almost the same and points to the same size. Therefore, one can conclude that 220 peak indicates the size of not the whole cluster, but rather of the single domain. This is probably due to the fact that among the first three diffraction peaks, the 220 peak has the highest multiplicity – 12 (for 111 peak – 8; for 220 – 6) and is not affected by twinning. Additionally, this peak overlaps less with other diffraction peaks, making 220 peak the best candidate for estimating the average domain size.

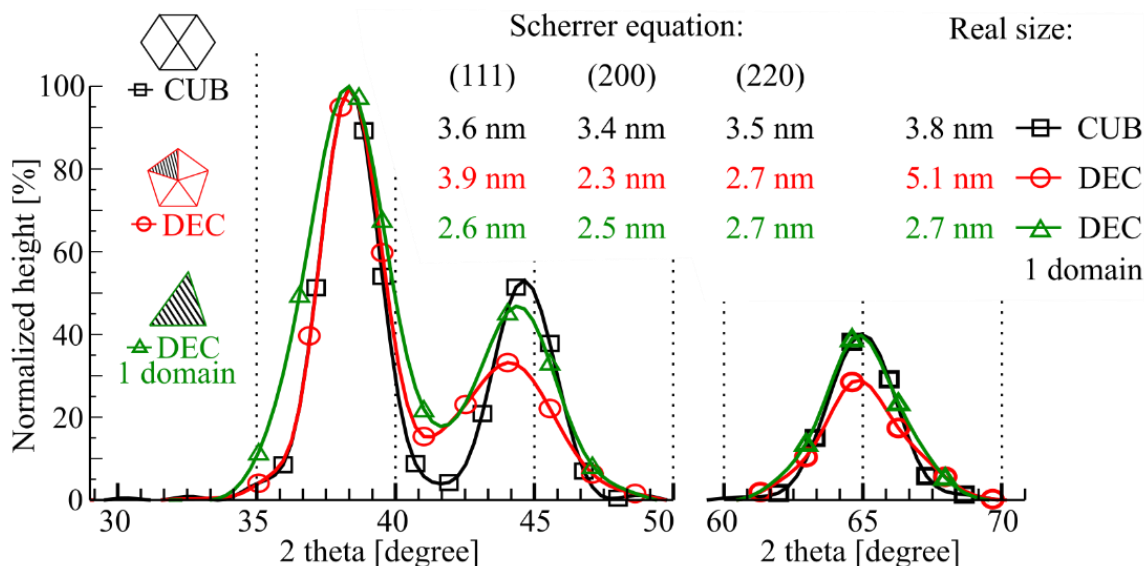


Figure 19 Calculated XRD patterns of the single domain CUB (2057 atoms), the relaxed model of the one domain DEC (951 atoms) and full 5 domain DEC (4776 atoms).

3.1.2.4 Number of domains analysis (MD + REL models)

According to Figure 15, as the number of domains increases, the height ratio of 220 to 111 peak decreases. It seems that this dependence can be predicted analytically using equations 23 and 24, however it is a very complex task. First, the more domain, the more [111] directions should be considered. Secondly, a large number of domains can dramatically change the peak profile (Figure 18), that is difficult to predict. Finally, the obtained dependencies must include the Debye – Waller (DW) factor, which is size dependent, meaning that a simplified equation for XRD patterns modification cannot be used.

To overcome these problems and find a correlation (between $H_{(220)}/H_{(111)}$ and morphology), 13 computational models of DEC were analyzed (Table 1). Each model was equilibrated at 293 K for at least 30 psec using molecular dynamics calculations (Sutton-Chen potential). After that, each DEC was disassembled (as shown in Figure 15) into one, two, three and four domain clusters. Then, for each cluster the powder XRD pattern was calculated, followed by the analysis of full width at half maximum (FWHM) and the height ratio of 220 to 111 peak (Figure 20).

List of CUB models

Number of atoms	Shells	Size, nm
147	3	1.46
309	4	1.87
561	5	2.40
923	6	2.81
1415	7	3.35
2057	8	3.76
2869	9	4.30
3871	10	4.71
5083	11	5.13
6525	12	5.66
8217	13	6.21
10179	14	6.61
12431	15	7.17
14993	16	7.56
17885	17	8.12
21127	18	8.51

List of DEC models

Number of atoms			m=n	p	REL
Total	1 domain	Central row			Size, nm
1228	243	13	5	3	3.15
1840	365	15	6	3	3.62
2622	521	17	7	3	4.13
3594	715	19	8	3	4.62
4776	951	21	9	3	5.10
6188	1233	23	10	3	5.52
7850	1565	25	11	3	6.06
9782	1951	27	12	3	6.54
12004	2395	29	13	3	7.02
14536	2901	31	14	3	7.50
17398	3473	33	15	3	7.98
20610	4115	35	16	3	8.44
24192	4831	37	17	3	8.95

Table 1 List of used decahedron (DEC) and cuboctahedron (CUB) computational models. The "m,n,p" parameters characterize the shape and profile of Marks DEC [51]. For NPs size estimation, the CLUSTER software calculated the volume of the cluster, then, the diameter of the equivalent volume sphere was obtained. Sizes were calculated for the relaxed models.

As shown in Figure 20, dependencies consist of two parts. The first one is a correlation between H_{220}/H_{111} and FWHM of 220 peak (for a constant number of domains), which can be fitted to the linear equation. The second part is a spacing between linear curves. By minimizing the difference between linear dependencies and H_{220}/H_{111} values, the spacing (is given in the braces) can be described by the natural logarithm of the number of domains (Num.dom.²⁹³):

$$\frac{H_{(220)}}{H_{(111)}} = -0.0065 * FWHM_{(220)} + \{-0.06 * \ln(Num. dom.) + 0.368\} \quad 25$$

$$Num. dom._{293} = \exp\left(\frac{0.368 - 0.0065 * FWHM - \frac{H_{(220)}}{H_{(111)}}}{0.06}\right) \quad 26$$

In general form equation 26 can be written as :

$$\frac{H_{(220)}}{H_{(111)}} = \gamma * FWHM_{(220)} + [\alpha * \ln(Num. dom.) + \beta] \quad 27$$

Equation 26 was derived from the computational models equilibrated at RT. In order to consider relaxed models (at ~0 K), it is necessary to reevaluate the dependence. Temperature directly affects the movement of atoms leading to a change in the DW factor. As a result, the H_{220}/H_{111} ratio vs FWHMs of 220 peak of the relaxed models (Figure 21) will look different than Figure 20.

Comparing Figure 20 and Figure 21, one can see the difference in the slope, intersections and spacing between dependencies. Therefore the α , β and γ parameters should always correspond to the actual temperature. Additionally, the shape of the domains should also be taken into account. Even though it has a minor impact, it is still worth to consider. The exact origin of the shape dependence is described in the following chapter 3.1.4. Comparing α , β and γ parameters for the 1 domain DEC and spherical CUB (single domain), one can see the difference (Table 2).

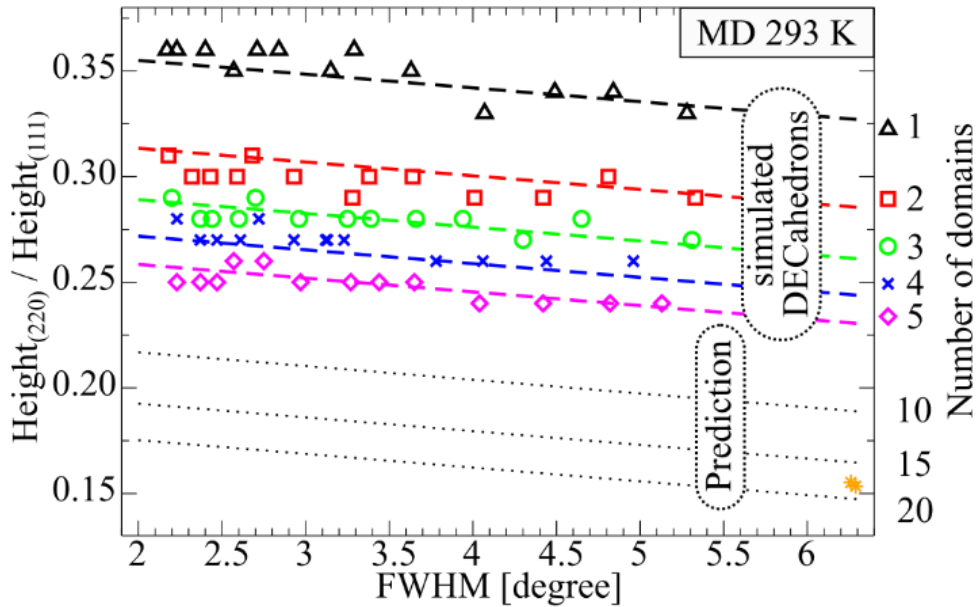


Figure 20 H_{220}/H_{111} ratio as a function of FWHMs of 220 peak. The yellow stars represent two ICO clusters (12431 and 14993 atoms). One can see a poor fit of linear dependencies and ICO models. This is caused by an extraordinary strain distribution in a single ICO domain (Figure 18), which makes FWHM larger. If the Icosahedron contains 14993 atoms, then 1 domain has ~750 atoms with size of ~2.6 nm. According to the Scherrer equation, the FWHM of such 1 ICO domain should be ~ 3.8 degree, which is in good agreement with obtained dependencies.

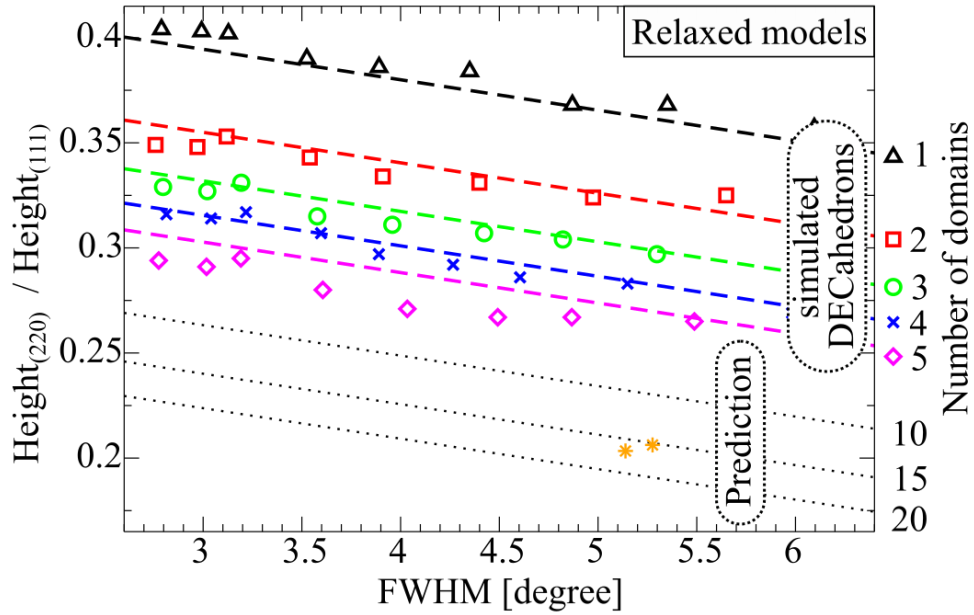


Figure 21 H_{220}/H_{111} ratio as a function of 220 peak FWHM. 10 relaxed gold DEC models were separated into 1-5 domain structures. The yellow stars represent ICO models with 12431 and 14993 atoms.



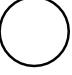
	Shape		α	β	γ
(a)	Derivatives of DEC MD 293 K		-0.06	0.368	-0.0065
(b)	Derivatives of DEC relaxed		-0.057	0.438	-0.0145
(c)	One domain sphere relaxed		-0.054	0.425	-0.015

Table 2 The α , β and γ parameters for different computational models

3.1.2.5 Estimation of the whole cluster size

If a cluster consists of domains, then knowing a number of domains (equation 26) and size of the average domain (Figure 19), one can calculate the size of the whole crystal. Computational simulations allow to find this dependence numerically by plotting the size of the average domain versus the actual particle size (calculated by the CLUSTER software):

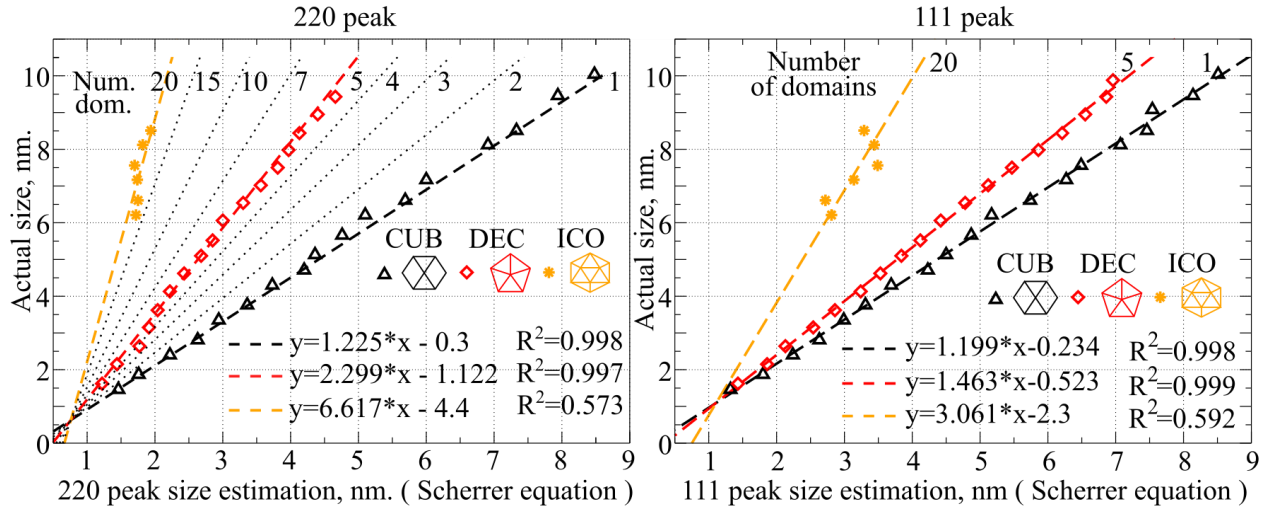


Figure 22 Correlations of average domain sizes (obtained from the Scherrer equation) as a function of actual cluster size depending on the number of domains. The colored dotted lines represent a linear fit of the obtained data with equations shown in the lower right-hand side corner. The left-hand side graph shows the correlation for 220 peaks, the right one shows the size correlation for the 111 peaks.

Figure 22 shows how the slope of the given size dependence is growing as the number of domains increases. Assuming that this slope changes linearly and uniformly, in general form it can be described as:

$$\text{Actual size} = a * \text{Scherrer (220) size} + b \quad 28$$

where a and b are changing linearly and proportional to the number of domains (for 220 peak):

$$a = 0.2489 * \text{Num. dom.} + 0.9118 \quad (R^2=0.99) \quad 29$$

$$b = -0.2165 * \text{Num. dom.} - 0.0639 \quad (R^2=0.99) \quad 30$$

3.1.3 Experimental application

Equations 28 - 30 have been obtained from ideal computational models, therefore it's necessary to verify their applicability for the analysis of experimental samples. For this purpose, eleven samples of Au and AuPt nanoparticles were chosen and analyzed in detail by XRD, TEM, and small-angle X-ray scattering (SAXS) method. These 11 samples were divided into two series: 9 samples demonstrating good efficiency of the multidomain XRD (MDXRD) approach (Table 3) and 2 samples illustrating limitations of the method (Chapter 3.1.4).

Group No.	Sample ID	Mean size, [nm]		
		MDXRD	TEM	SAXS
1	Au_PVP 1	2.2	2.3	2.6
	Au_PVP 2	2.8	2.7	3.0
	Au_PVP 3	2.9	2.9	3.1
2	Au_PVP_SiO ₂ RT	7.1	6.7	7.0
	Au_PVP_SiO ₂ 400 °C	5.8	6.3	6.7
	Au_PVP_SiO ₂ 500 °C	6.9	6.4	6.5
	Au_PVP_SiO ₂ 600 °C	6.9	6.7	6.7
3	Au_Pt_SiO ₂ RT	3.9	4.2	3.5
	Au_Pt_SiO ₂ 450 °C	5.3	5.4	5.0

Table 3 Volume weighted mean sizes of NPs obtained using MDXRD, TEM and SAXS

If one rearranges equations 28 - 30 to calculate the number of domains (*Num.dom.*), two components are required. The first one is the size of the average single domain (*Scherrer(220) size*), which can be found only from XRD method. The second one is the mean size (*Actual size*) which can be found separately using TEM and SAXS (equation 31). This feature can be used to analyze the number of domains by combining XRD with TEM and SAXS:

$$Num. dom. = \frac{0.9118 * Scherrer (220) size - Actual size - 0.0639}{0.2165 - 0.2849 * Scherrer (220) size} \quad 31$$

Figure 23 **a** shows that number of domains analysis of experimental samples using the combined SAXS – XRD (blue triangles) and TEM – XRD (green pluses) provides very similar results. However, the values obtained by the multidomain X-ray diffraction method are systematically and noticeably greater than the results of combined methods. To compensate for this difference, the intercept part (β) of equation 26 should be reduced by ~13% from 0.368 (theoretical calculations) to 0.32. Equation 26 in a general form for FCC NPs at RT can be written as:

$$Num. dom. = \exp \left(\frac{\beta - 0.0065 * FWHM_{(220)} - \frac{H_{(220)}}{H_{(111)}}}{0.06} \right) \quad 32$$

The origin of the β modification is described in chapter 3.1.4 below. Applying the β parameter correction results in good agreement between MDXRD and combined techniques (Figure 23 b). Knowing the number of domains, one can calculate the mean size of NPs in the experimental samples. As can be seen from Table 3 MDXRD, TEM, and SAXS analysis provides remarkably similar estimations of the mean sizes. A correct prediction of mean size can be used as an indicator of applicability of MDXRD method.

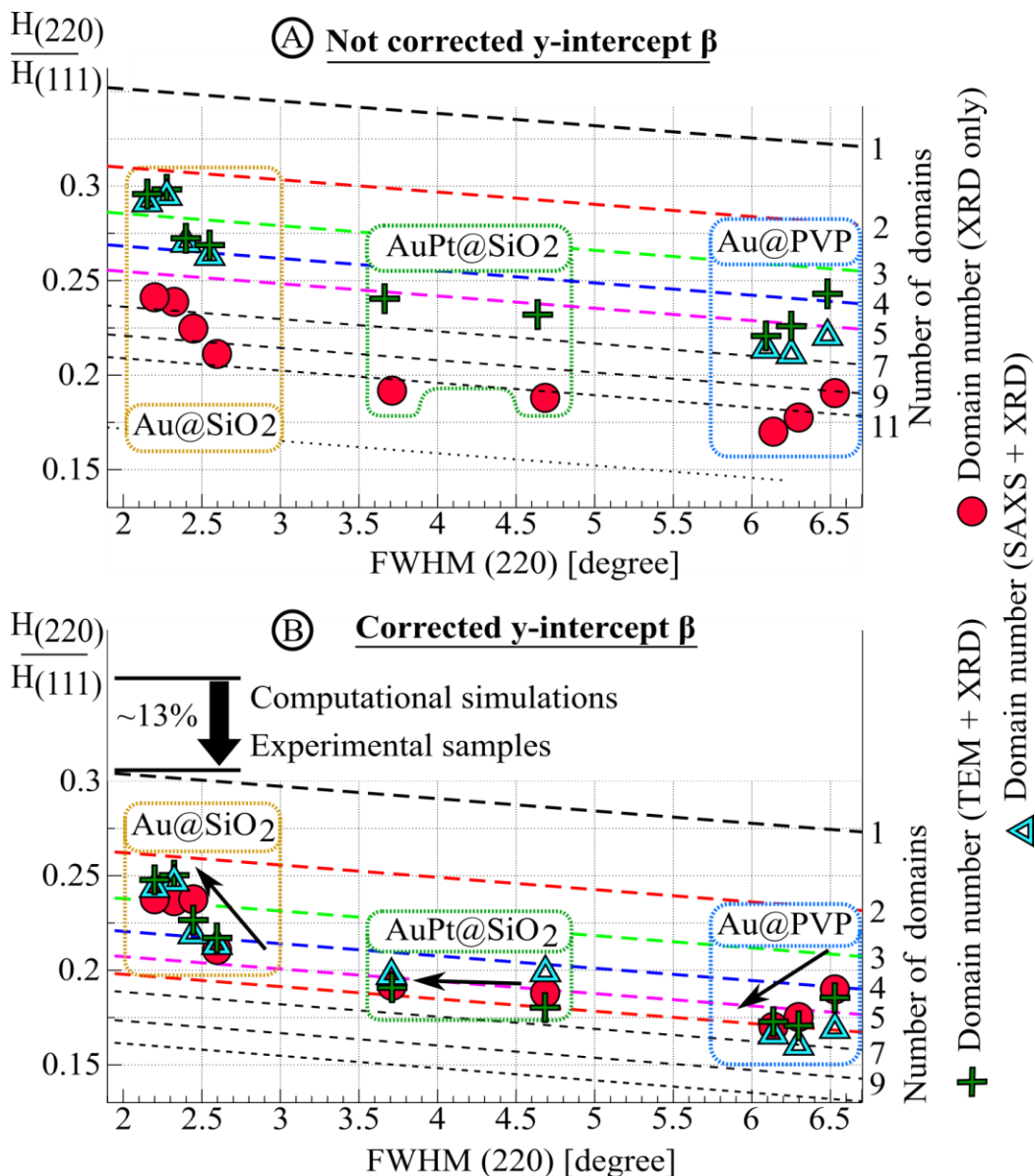


Figure 23 Results of the number domain analysis of Au and AuPT samples obtained by different techniques. The red circles show the results of multidomain XRD alone (based on equation 32). The blue triangles represent combined SAXS – XRD approach (based on equation 31). The green pluses represent the combined TEM – XRD method, where the *actual size* – corresponds to the mean volume-weighted size (based on equation 31).

3.1.4 Corrections and limitations

The 13% modification of the β parameter is necessary because of the shape of the used DEC segments. The analyzed single DEC domains have the shape of an elongated triangular bipyramid, which is asymmetrically elongated. This makes XRD 111 peak broader, but of less height. Therefore, the $H_{(220)}/H_{(111)}$ ratio of 1 DEC domain is greater than for the CUB model (Figure 24). In the case of experimental powder XRD, the resulting scattered X-ray intensities are averaged over billions of domains, leading to the average domain shape of more isotropic character. Therefore, for the experimental samples analysis, one should consider a nearly spherical shape of domains.

In the case of gold, the modification of the β value can be separately justified by the standard X-ray powder diffraction data (e.g. JCPDS no. 04-0784), directly indicating that the $H_{(220)}/H_{(111)}$ ratio is equal 0.32. Therefore, for other FCC metals, the value of β can be taken from a database.

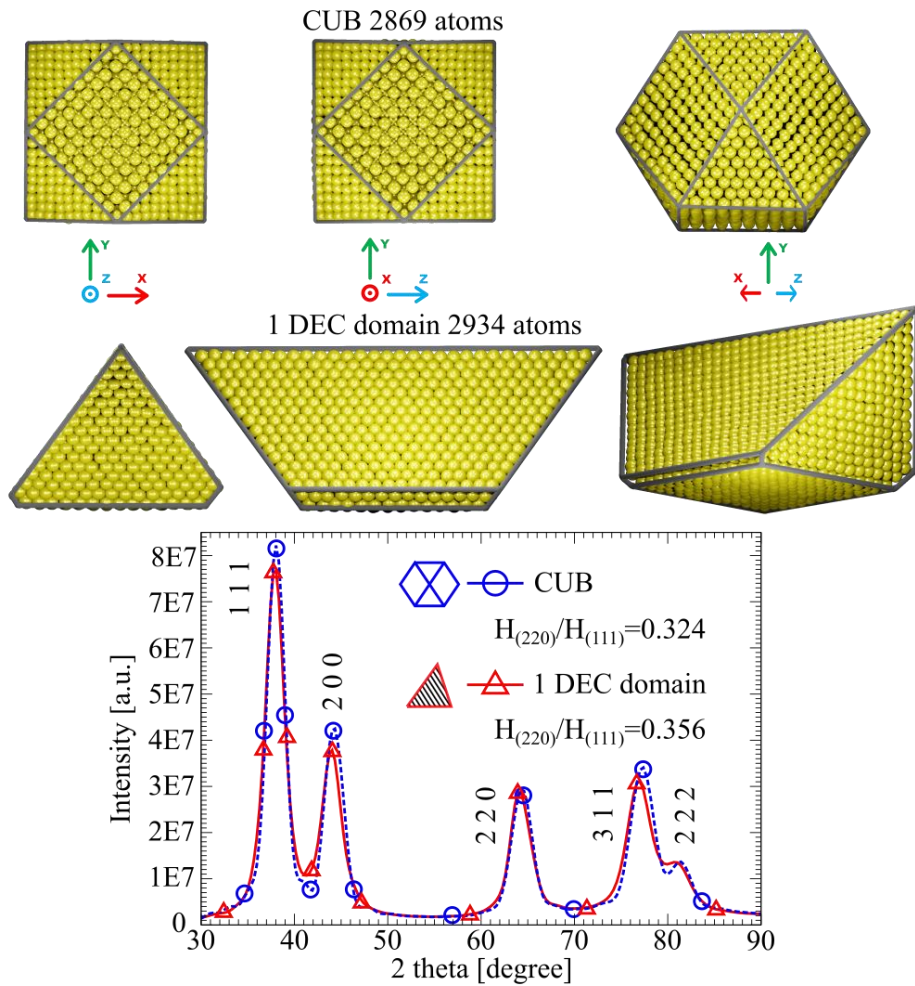


Figure 24 Comparison of the calculated X-ray diffraction patterns of the one domain DEC segment and the regular CUB. Both models were analyzed after MD at 293 K for at least 30 psec.

As can be seen from Table 3 and Figure 23, MDXRD results can demonstrate a good agreement with other techniques. However, as it was mentioned earlier, the multidomain approach has some limitations. It cannot be directly used to analyze samples with a wide NPs size distribution. All diffraction methods, in contrast to microscopy, are sensitive to a volume-weighted size distribution. The intensity of scattered X-rays is proportional to the particle volume. The volume is proportional to the third power of the NP radius, therefore the contribution to intensity of big particles is greater than the contribution of small ones. As a result, the collected patterns will mostly represent a large size fraction, sometimes leading to nonsense results of the MDXRD approach. As it is shown in Table 4, the analysis of Au@C sample estimates the average number of domains to be $\sim 0.6 - 6.45$. The mean size estimations of Au@C NPs are also differ.

Group No.	Sample ID	MDXRD		TEM		SAXS	
		Num. dom.	Mean size, [nm]	Num. dom.	Mean size, [nm]	Num. dom.	Mean size, [nm]
FWHM (no correction)							
4	Au@C	6.45	13.89	0.56	5.79	2.14	7.97
2	Au@PVP@SiO ₂ 800 °C	4.01	19.03	-0.61	7.24	0.17	9.23
Integral Breadth							
4	Au@C	5.70	7.29	3.69	5.79	6.61	7.97
2	Au@PVP@SiO ₂ 800 °C	3.70	10.18	1.58	7.24	3.01	9.23

Table 4 Volume weighted mean sizes of NPs with a wide size distribution calculated by MDXRD, TEM and SAXS

Another example of the non-applicability of MDXRD is Au@PVP@SiO₂ sample after high temperature treatment (800°C in He). The initial sample was heated stepwise (RT => 400 => 500 => 600 => 800 °C) and up to 600°C the MDXRD results were consistent with other techniques (Table 3). However, after treatment at 800 °C, the nanoparticles started to grow more intensively, and the particle size distribution became wider and more extended toward large sizes. Therefore, the MDXRD method overestimated the mean size, while the combined techniques estimated the number of domains as negative (TEM + XRD) or close to zero. The negative value appeared because the average single domain size (calculated from the 220 peak) was larger than the average size obtained from the TEM grain size distribution analysis.

One way to compensate for the peak shape effect due to appearance of the narrow large size contributions is to use integral breadth of a 220 peak, instead of FWHM. Since the broadening changes the peak profile making it closer to Lorentzian profile, the direct use of FWHM is no longer

acceptable. The use of the integral breadth allows to improve the consistency of the obtained results (Table 4).

3.1.5 Summary of MDXRD

Despite the limitation described above, as can be seen from Table 3 the MDXRD method provides nanoparticles size estimations consistent with other techniques. However, the most important aspect of this technique is the ability to explore the bulk morphology evolution. Figure 23 shows different types of morphology evolution. Under a long time exposure to X-ray beam, Au@PVP NPs demonstrate an increase of the average number of domains. This phenomenon is discussed in Chapter 3.2.3. At the same time, during high temperature treatment, gold NPs encapsulated in SiO₂ show decrease in the number of domains. Chapter 3.2.2 is dedicated to description of this phenomena.

Table 3 shows mean size only for Au and Au-Pt samples. The scattering properties of platinum and gold are similar, therefore equation 26 can be applied without modifications. Nevertheless, the use of the MDXRD method is not limited to Au and AuPt, and it can be applied to other FCC metals. The second part of the technique description (equations 28-30) is material independent, so no modification of this part is required. Meantime the first element of the method (equation 32) should be modified. The first element of the equation, the β parameter ($H_{(220)}/H_{(111)}$ ratio) is material dependent and can be taken from the standard XRD databases. The second element of the equation – the distance between lines is a result of special mutual orientation of domains and is material independent. The last element of the equation is the slope, which includes two factors: a size dependent DW factor and the mutual orientation of domains (material independent). The material dependent DW can be included as a β parameter, and its size dependence can be predicted by MD simulations for a given temperature. Thereby in order to apply the MDXRD to other FCC metals (at RT), only one modification is required - the adjustment of the characteristic β parameter.

Besides analysis of the experimental samples, MDXRD is important for the analysis of computational simulation models. In the case of regular DEC and ICO, it is easy to determine the average number of domains: 5 and 20, respectively. However, in the case of irregular structures (Figure 25), it cannot be done visually. Only MDXRD method (equation 32) allows one to characterize the average domain number. These irregular models are of special interest because they can produce XRD patterns like that of regular DEC. Meantime their interiors are completely different.

Another interesting consequence follows from Figure 22, which demonstrates the principal applicability of the Scherrer equation to nanoparticles. It's known that the Scherrer equation can perform well for nanoscale objects, however to the best of our knowledge there was no systematic and consistent explanation e.g. linked domains. Figure 22 illustrates that for small nanoparticles ($\sim 1 - 1.5$ nm), the Scherrer equation is applicable regardless of the number of domains. However, the larger NP size, the stronger the divergence between the Scherrer size estimation and the actual size.

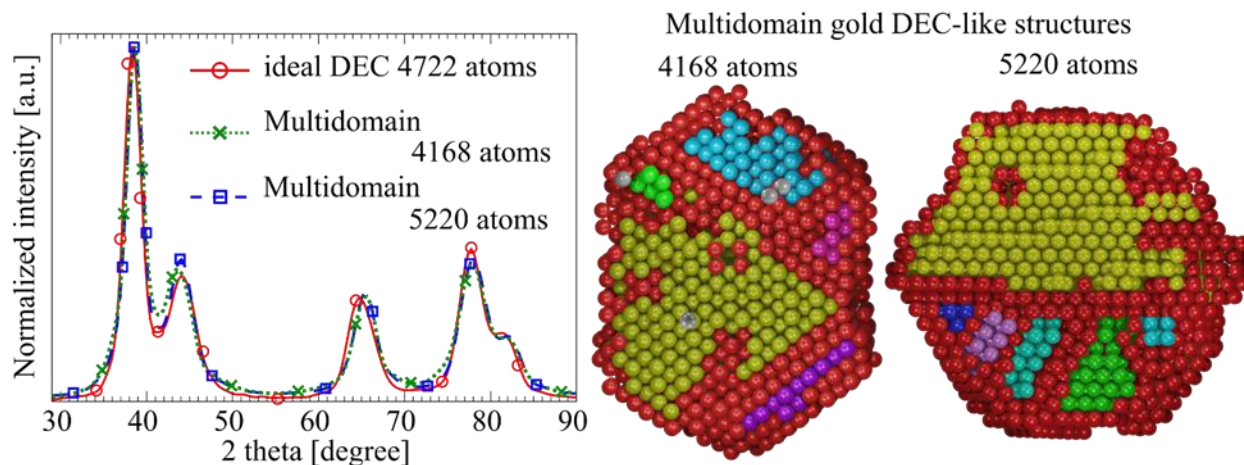


Figure 25 Calculated X-ray diffraction patterns of the regular relaxed DEC and of two relaxed multidomain structures. Atoms shown in red belongs to twin planes or neighbor the surface/defects atoms, all other colors represent ideal FCC domains. All models are made of gold atoms.

3.2 Vacancy driven twinning

Appearance of one or another FCC morphology is usually justified by its minimum potential energy per atom. However, this approach does not allow to account for infinite variety of the experimentally observed multiply twinned nanoparticles [30, 40, 118]. Furthermore, some computational models of irregular morphologies can be as stable as ideal CUB/ DEC/ ICO forms (Figure 26). Therefore, the thermodynamic approach should consider free energy and cannot be widely applied. Instead, it is simpler to consider the mechanism of twinning taking into account kinetic aspects [119,120]. At the moment, three commonly used mechanisms can be distinguished.

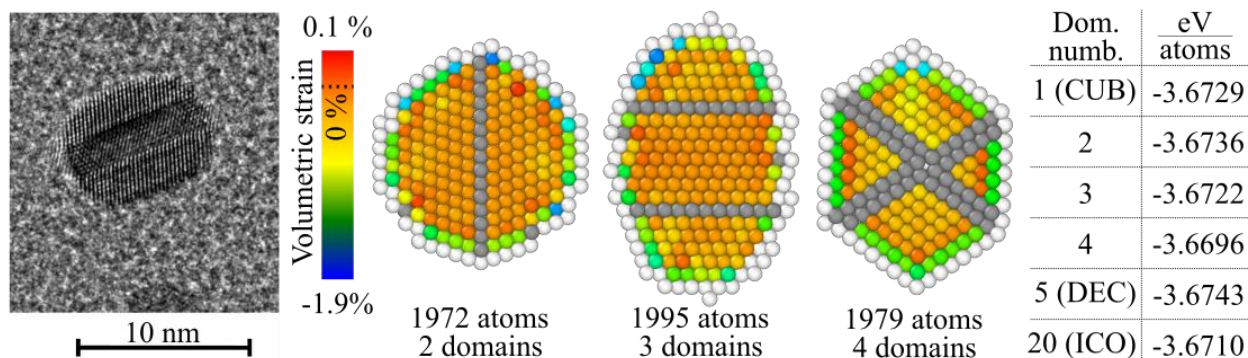


Figure 26 TEM image of the 3 domain Au@PVP NP; computational models of 2, 3 and 4 domains Au clusters. The table shows the potential energy per atom for the irregular (2,3,4 domains models) and regular CUB (1985 atoms), DEC (1984 atoms) and ICO (1985 atoms) models. White balls correspond to surface atoms, gray atoms represent twin planes. The visualization of other atoms is based on volumetric elastic strain calculations done by OVITO [60]. All models were relaxed.

The first twinning mechanism is the formation of twin boundaries as a result of coalescence. Particles sintering can lead to the appearance of a single or multiple mirror planes [30, 121]. The simple single twin plane is a mobile structure, and its appearance can be reversed [118, 122]. However, in the case of multiple twinning, a complex cross-twinning phenomena occur, sometimes leading to the creation of a 5-fold axis [31]. The coalescence of particles was studied explicitly using computational simulations [36, 123, 124]. Nelli et al. [125] even described the appearance of DEC/ICO - like structures as the product of sintering of multiply twinned particles.

The second mechanism considers twinning as a result of stepwise nucleation processes in a gas phase. The growth process begins with formation of the ideal FCC tetrahedral seed, followed by appearance of HCP islands near the edges of the tetrahedron. At the next step, these HCP pieces act as nucleation centers for new FCC domains, which eventually lead to the formation of a twin plane in between the old and newly formed domains. Depending on the number of simultaneously formed stable HCP islands the nucleation process can lead to the appearance of DEC (2 islands) or ICO (3 islands) [38]. This mechanism was observed experimentally by the in-situ TEM technique [126, 127].

The third mechanism is more chaotic and considers twinning as a consequence of condensation of atoms. To simulate this process all atoms can either be slowly, atom by atom, deposited next to the initial seed [33, 128] or randomly placed in a certain volume at once. The first approach most often leads to the formation of distorted (asymmetric) regular DEC or ICO structures. The second one allows to obtain irregular two / three [129] and regular five [130] domains structure.

In most cases, these mechanisms lead to the formation of DEC / ICO - like structures. The appearance of other irregular forms (Figure 26, [40]) is rarely considered because experimental microscopy observations often show regular structures. However, it is likely that the native morphology of clusters can be strongly affected by the electron flux during TEM analysis. Young and co. [131] showed that Au nanoparticle can dramatically change its morphology under the focused electron beam. The non-perfect 9 nm DEC cluster becomes half amorphous after 30 sec of e^- beam exposure, followed in 15 seconds by formation of an ideal single domain structure, eventually forming ~ 2 domain structure after 75 sec of exposure. Even if such a large particle morphology is unstable, then one has to be careful with the interpretation of TEM data.

It is expectable that NPs prepared by chemical route may possess a structure that does not correspond to the energy minimum. Since the e^- beam can facilitate atomic diffusion [132, 133], the particles with high potential energy configuration may rearrange their interior towards a lower energy state [122]. Therefore, to observe original morphologies, one has to find an alternative to microscopy techniques. The MDXRD is the method that can provide less disruptive insight into the structure.

To fill the gap in understanding the appearance of irregular and unstable morphologies, a new concept was developed - vacancies driven twinning. This concept can also provide a certain insight into the kinetic trapping effect of twinning processes. The previously listed mechanisms cannot do this, because they descriptively show how atoms should stack to obtain one or another morphology. However, there are no clear criteria of why one type of stacking should take place and not another. Vacancies driven twinning can be indirectly verified by TEM, XRD and SAXS techniques by measuring vacancy dependent parameters: size and density of NPs. Also, the results of computational simulations based on this concept are in a good agreement with the experimental observations and XRD patterns.

3.2.1 Vacancy driven twinning

As it was shown earlier (Chapter 1.1.3) the role of vacancies was considered only from the point of view of the melting temperature and its effect on a surface. Mei and Lu [134] proposed that temperature induced melting of the bulk occurs when surface vacancies (at least 10 % of the whole surface) diffuse into the bulk. The diffusion of vacancies into the bulk makes the crystal lattice unstable, which eventually leads to the melting. Nevertheless this concept differs significantly from the vacancies driven twinning approach outlined below. Mei and Lu considered premelting temperatures and did not predict the appearance of any changes in the crystal lattice.

Based on computational simulations (performed in the CLUSTER program), it was found that twinning of FCC metals can be triggered by vacancies. The simulations consider random deletion

of the crystal atoms followed by the energy relaxation of the model. If the concentration of the formed vacancies is below $\sim 13\%$, no visible change in morphology occurs, and all defects are distributed in the cluster. The only result is the displacement of atoms neighboring vacancies from their nodal positions toward defects, causing appearance of the elastic strain (Figure 27 a) and overall lattice contraction. The shrinking of the crystal lattice can be noticed from the XRD patterns as a uniform shift of all peaks to the right-hand side (Figure 28 c).

As follows from simulations, if the concentration of vacancies equals to or exceeds 13% , then some defects can rearrange into twin planes (Figure 27 b). It is likely that high concentration of defects reduces the energetic barrier for collective movements of atoms. Therefore, the atoms located near vacancies fill the empty space, while their neighbors got enough space to find a new nodal position initiating cascade movement of atoms. These rearrangements decrease the content of vacancies and partially release the elastic strains.

It is important to note that CLUSTER generates vacancies randomly, therefore they are not always uniformly distributed in a particle. If the local arrangement contains a high concentration of defects then the twinning will occur. Additionally, even after twinning, some vacancies can be preserved as shown in Figure 27 b. The critical concentration of 13% is not universal and is an average empirical value. In some cases the twinning may not occur even with $14\text{--}16\%$ of defects. At the same time, during high temperature computational simulations (simulated annealing) the twinning may occur below the critical value.

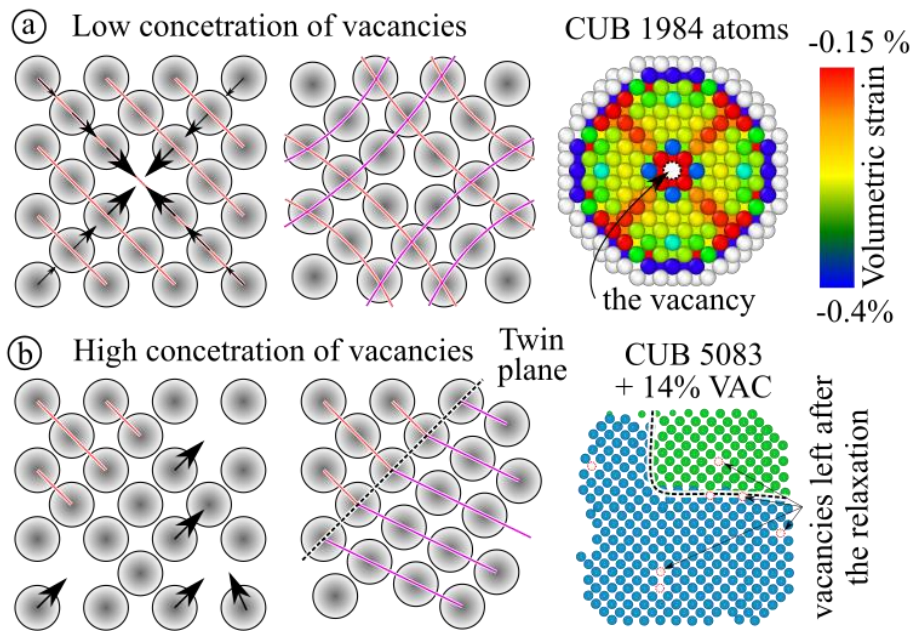


Figure 27 Schematic illustration of the vacancies driven twinning concept; a) if the concentration of vacancies is less than $\sim 13\%$ then only elastic strains appear after the relaxation; b) If the concentration of vacancies is equal to or exceeds $\sim 13\%$ then after the relaxation, the cross-twinning may occur while some of the vacancies may be preserved. Visualization of green and blue domains was done in the BLENDER software; different colors represent different domains, that have been identified manually.

3.2.1.1 Computational simulations: Relaxation

Using embedded into the CLUSTER software functions, one can easily follow the twinning induced by the vacancies. Figure 28 shows an example of a magic number CUB (5083 atoms) deprived of 14% atoms, that has been relaxed. Vacancies were generated randomly by removing atoms at random positions (one vacancy – one atom). The relaxation (following conjugated gradient routine) was stopped when the gradient of total potential energy reached the level of $1E-5(6)$ Ev/[Å].

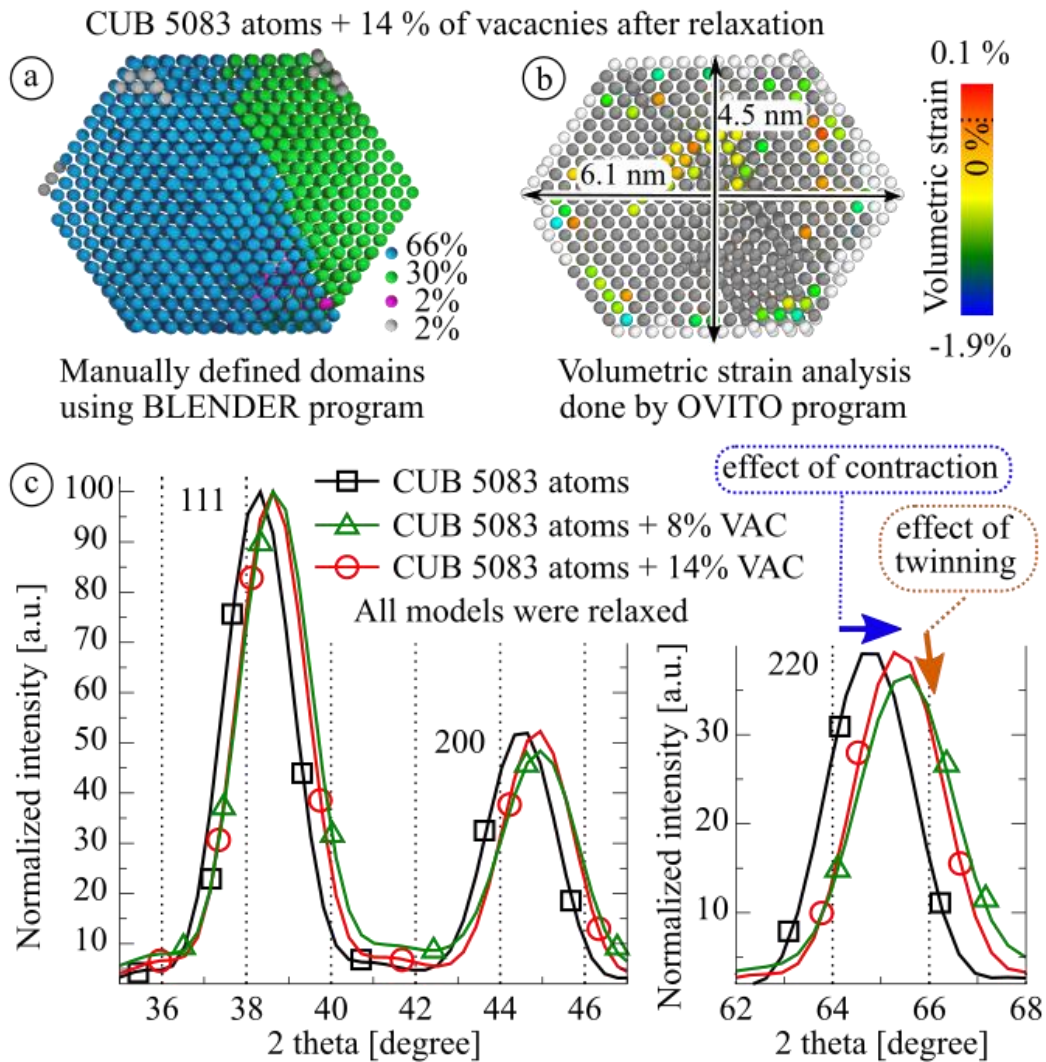


Figure 28 Analysis of the CUB (5083 atoms) with 14% of vacancies (minus 712 atoms) after the relaxation; a) the result of manual domain analysis performed visually based on how ideally and periodically the atoms lie in rows. The ideal FCC domain should not contain twin planes and added atoms (shown in grey). b) automatic volumetric strain analysis done by OVITO program; c) XRD patterns correspond to ideal CUB (5083 atoms), CUB with 8% and 14% of vacancies.

As can be seen from Figure 28 **a**, the obtained multidomain structure is not symmetrical and domains are not equal. It is easy to divide DEC / ICO into segments and draw conclusions about morphology. In the case of multidomain structures such an approach can't be applied. First of all, the newly created domains have different sizes and complex 3D shapes. To some extent, it is possible to manually guess boundaries of domains by rotating the structure in 3D space using graphical programs (such as BLENDER). However, this is an extremely time-consuming, non-trivial task with not very accurate results in the end. The problem of domains boundaries determination can be solved by using elastic strain calculator/structure type analysis that are sensitive to the type of crystal structure (OVITO program). The algorithm can determine the local arrangement of FCC atoms. When a twin plane appears it creates a HCP atom coordination which breaks the FCC sequence and corresponding HCP atoms will be excluded from the analysis. Therefore, the twin plane analysis (Figure 26, Figure 27 **a**) is a side product of the elastic strain calculator. However, this algorithm is also sensitive to vacancies and it will not work for models with high concentration of defects (Figure 28 **b**). In such a case the algorithm will exclude most of atoms from the FCC pool. The determination of domain borders in highly defected models is thus less strict and more intuitive.

The second problem is definition and selection of domains. It is known that the regular DEC has 5 domains, ICO contains 20 segments. However, how to characterize irregular structures such as the cluster shown in Figure 28 **a**? Is it a two/three or four domains structure? Using the manual domains determination one can find the reasonable answer. However, the visual approach cannot be used as a routine tool because it requires manual analysis of all models, which is difficult for the above mentioned reasons.

The easiest way to overcome these issues is to use the MDXRD method. Since it is sensitive to twinning it can provide a reasonable description of the sample. The results of multidomain XRD approach applied to CUB 5083 atoms with different density of vacancies are shown in Table 5. According to the MDXRD approach, the cluster shown in Figure 28 **a** has 1.9 domains. This is the average result for the whole structure.

As discussed earlier (Chapter 3.1.3) the goodness of MDXRD analysis can be assessed by comparing the MDXRD size estimation with results from other methods. However, for a nonsymmetrical computational models (like CUB) which are vacancy-ridden it's difficult to get the precise average size. Also, different methods are sensitive to different structure features. For these reasons, SAXS, MDXRD and volume-based calculations will provide slightly different results. Nevertheless, Table 5 shows that there is a good correlation between obtained size estimations. Therefore, the MDXRD measurement of an average domain number can be considered as a valid tool for the analysis of multidomain particles.

In order to systematically explore how the vacancies driven twinning depends on the CUB size, we analyzed 3–10 nm CUBs with different density of vacancies (Table 6). The average domain values were estimated using MDXRD method adopted for the relaxed spherical models (Table 2).

The initial model is CUB 5083 atoms

VAC [%]	Scherrer equation		MDXRD		Volume based size, nm	SAXS Mean size, nm
	111 peak	220 peak	Num. dom.	Size, nm		
0	5.46	5.16	1.00	5.80	5.19	5.48
8	5.21	5.05	1.10	5.70	5.17	5.43
10	5.17	5.05	1.07	5.71	5.16	5.41
12	5.16	5.04	1.11	5.74	5.16	5.40
14	4.48	4.41	1.90	5.69	5.16	5.35
16	3.33	3.43	2.86	4.98	5.14	5.24
18	3.82	3.21	4.30	5.49	5.11	5.17
20	2.74	2.26	8.84	5.25	5.05	5.13
22	3.37	2.53	7.83	5.65	5.00	5.07

Table 5 Results of different size analysis methods applied to CUB (5083 atoms) models with different concentration of vacancies, after the relaxation. The volume-based size was calculated by the CLUSTER algorithm which measures the volume of the cluster, then calculates the diameter of the equivalent volume sphere. SAXS, MDXRD and Scherrer equation analysis were applied to the diffraction patterns of the simulated models. Diffraction patterns were calculated using the CLUSTER program.

As can be seen from Table 6, all computational models containing $\leq 12\%$ of vacancies consist of ~ 1 domain and did not show signs of twinning. Deviations from “1” are caused by the background subtraction method. To determine the background line systematically and to avoid a human factor the subtraction was done by the script. However, for small, monosized models, the peak shape includes side ripples moving with the size, and changes of the side bands' positions affecting peaks separation, were not taken into account. As a result, the background lines were not determined properly leading to an increase of the error in the estimation of the peak height. This observation highlights the principal difficulty of the MDXRD application - its sensitivity to background line subtraction. By comparing the size estimations made by MDXRD with results of other techniques (similarly to Table 5) one can roughly estimate the precision. If num.dom. < 10 the precision is smaller than ± 1 domain; if num.dom. > 10 the precision is bigger ± 1 domains.

According to Table 6 not every CUB with 14% of vacancies undergo twinning. This is probably caused by two features of the random distribution of the defects. First of all, if a significant number of vacancies is created on the surface the effective concentration of vacancies in a bulk will be lowered. As a consequence, the initiation of twinning will require more vacancies than actually

necessary (see Table 6 CUB 2057 + 16% VAC). The second feature is the local distribution of defects. If all defect are localized close to each other then it will make twinning of one cluster part more favorable than an another part. Taking into account all these factor one may introduce - the highest critical concentration at which twinning will occur with high likelihood. According to the simulations (Table 6) this parameter should be equal to 18%.

Au CUB, atoms	Vacancies [%]; relaxed models									Number of domain
	0	8	10	12	14	16	18	20	22	
923	1.1	1.3	1.1	1.2	3.5	2.9	8.3	6.1	7.5	1
1415	1.1	1.3	1.3	1.1	4.3	3.4	3.8	7.3	6.6	3
2057	1.1	1.1	1.1	1.2	1.2	1.5	4.0	3.7	5.3	4
2869	1.0	1.1	1.1	1.2	1.2	1.6	5.6	8.8	<u>3.8</u> ¹	6
3871	1.1	1.1	1.0	1.1	1.5	4.6	2.6		<u>7.7</u> ²	8
5083	1.0	1.1	1.1	1.1	1.9	2.9	4.3	8.8	7.8	10
6525	1.0	1.1	1.1	1.1	1.1	6.1	10.3	5.5	8.0	11
10179	1.0	1.1	1.1	1.2	1.2	6.0	7.7	12.6	5.1	13
14993	1.0	1.1	1.2	1.3	1.3	10.1	<u>6.5</u> ³	<u>8.9</u> ⁴	13.0	
21127	1.0	1.1	1.1	1.2	2.2	6.2	8.0	13.0		
28741	1.0	1.2	1.2	1.3	1.3	8.4	10.1	13.0		

Table 6 Summary of computational modeling of the vacancies driven twinning. A different number of vacancies were created in gold magic number CUBs, followed by relaxation. Then, for each model, corresponding XRD patterns were calculated and analyzed by the MDXRD method adopted for the relaxed spherical models (Table 2). This method provided information on the average number of domains in each model. For the two last CUBs (21127 and 28741), the effect of 22% of vacancies is not indicated because the computational time exceeded several months, and the equilibrium state was not reached. Models marked by 1-4 numbers are described in details below.

Analyzing the numbers of domains in models with 18–22 % of vacancies one can notice the apparent lack of a direct correlation between the number of vacancies and the number of domains. In some cases, a small number of vacancies produces a more distorted structure than models with a high number of defects. To explain this feature, we can apply the same reasoning as before. The generation of defect is a random process, meantime twinning strongly depends on the distribution of these voids.

However, the existence of a direct correlation in a large set of crystals (powder) seems logical: the more possibilities for rearrangement, the more often these rearrangements will occur. This trend would be clearer if the randomness of vacancy localization is eliminated. This can be observed by looking at large computational models. For such models, the random removal of atoms can be considered more uniform, because of the very low probability of removing atoms that are close to each other. In addition, such models show a low surface to bulk ratio. Probably for these reasons, for large CUBs (21127 and 28741 atoms) one can notice increasement of the average number of domains with growth of vacancy concentration.

The dependence of the number of domains on the density of vacancies is better seen using its average values over various sizes for a given density of vacancies. From Figure 29 a one can see two trend lines: the blue line represents single-domain models with small number of vacancies and the red line corresponds to the multiply twinned models. The intersection of these lines indicates the lowest concentration of vacancies allowing twinning, equal to $\sim 13.1\%$. If the concentration of vacancies is below this critical value twinning will not occur (in case of the relaxation). This parameter is size independent and universal. The exact origin and physical meaning of this value (13.1%) are unclear. There may be a special sequence of vacancies that may cause twinning with a defect density below 13.1% . However, the above-mentioned computational models consider only randomly created vacancies where the formation of twin planes is not efficient. In other words, not all randomly created vacancies contribute to the twinning, and the considered simulations require an excess of vacancies. Therefore, it is likely, that there is a fundamental lowest critical concentration leading to the twinning, which is lower than 13.1% .

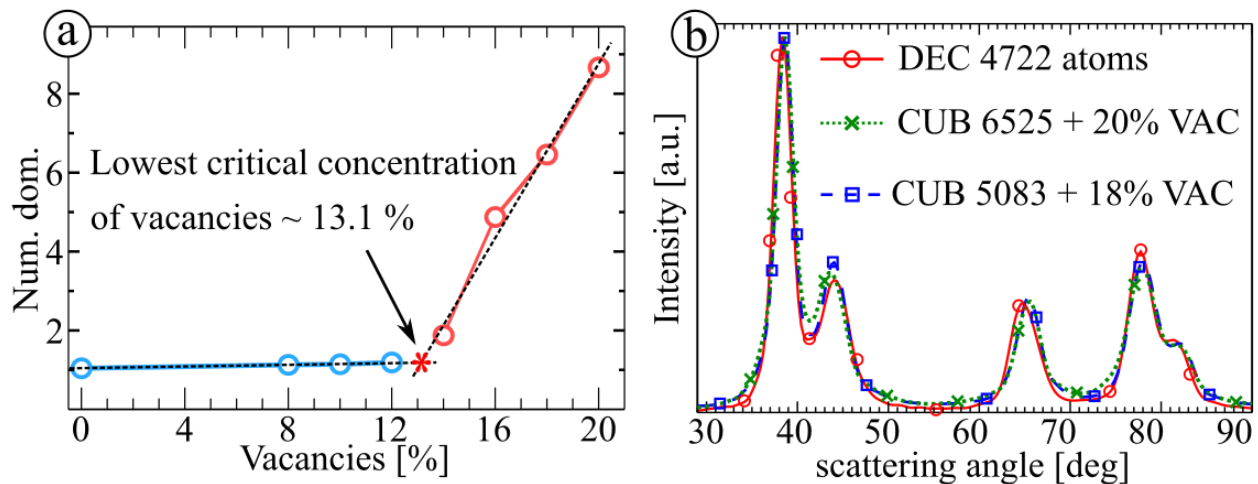


Figure 29 a) The dependence of the number of domains (Num.dom) averaged over models of all sizes depending on the fraction of vacancies. Blue points correspond to models without twin planes, pink points represent multiply twinned particles. The intersection of these lines correspond to the lowest concentration of vacancies at which twinning is possible; b) These graphs show the similarity of XRD patterns of regular DEC and two multidomain structures from Table 6.

Figure 30 shows that imposing vacancies in a regular CUB can lead to the creation of not only 1-2 layers thick HCP stack (in the form of twin planes), but also to a new 4-layers thick HCP phase. For this reason, a new 011 peak of the HCP phase can appear between 111 and 200 diffraction

peaks and can be seen in the XRD pattern. It should be noted that the absolute amount of HCP phase is less important than the ratio between HCP and FCC. Although CUB 10179 with 18% and 20% of vacancies has a similar share of HCP phase, the CUB model with 20% vacancies has smooth and symmetrical diffraction peaks, in contrast to the 18% VAC model. The higher HCP phase concentration, the more developed the peak associated with HCP. It can be clearly seen by comparing the diffraction patterns of CUB 2869 with 22% of VAC and CUB 3871 + 22% of VAC. The last model is especially interesting because it shows appearance and gives an idea of how Au HCP phase (which was observed experimentally [40]) can be more favorable than FCC.

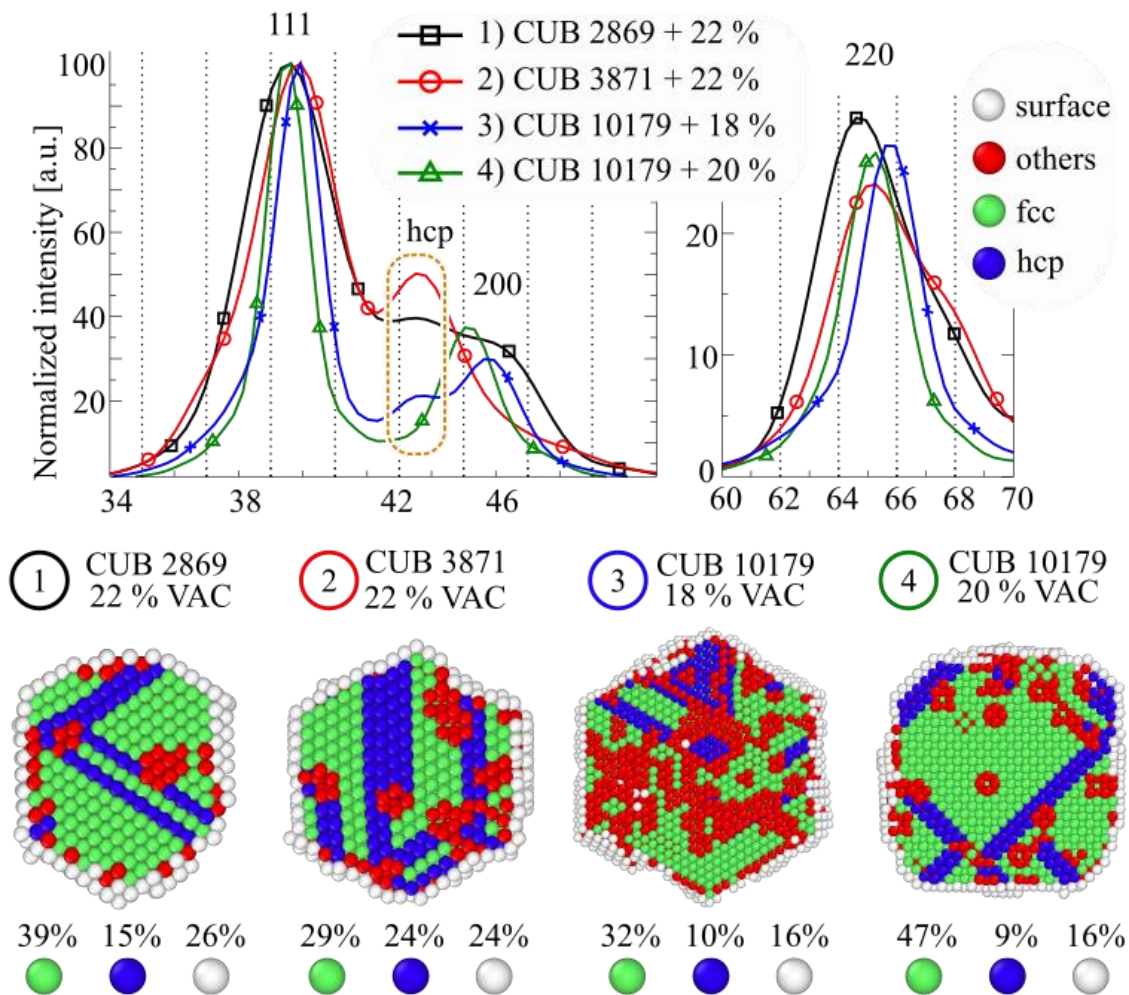


Figure 30 XRD patterns were calculated for four relaxed gold multidomain models. Using the OVITO software, FCC (green balls) and HCP (blue balls) atom environments were identified; the surface atoms (white balls) were defined by calculating the potential energy of atoms using CLUSTER program. Red balls represent atoms which are in direct contact with vacancies. The percentages shown below the cross sections of clusters represent the fraction of phases.

The phase analysis of multiply twinned particles shows that the appearance of HCP layers and phases can be considered as a common phenomenon. The asymmetry of 200 and / or 220 diffraction peaks were observed for ~ half of all models (Table 6) containing 16 – 22 % of vacancies. It is expected that such models are less energetically stable compared to regular CUB, DEC and ICO. From Figure 31 one can see that the minimum potential energy per atom of multidomain particles is significantly higher than in the case of regular structures. As it will be shown below, this is mainly due to the presence of vacancies rather than the appearance of stacking faults. Since all multidomain models were only relaxed, these models are in local energy minimum states, which allows trapping vacancies in the bulk.

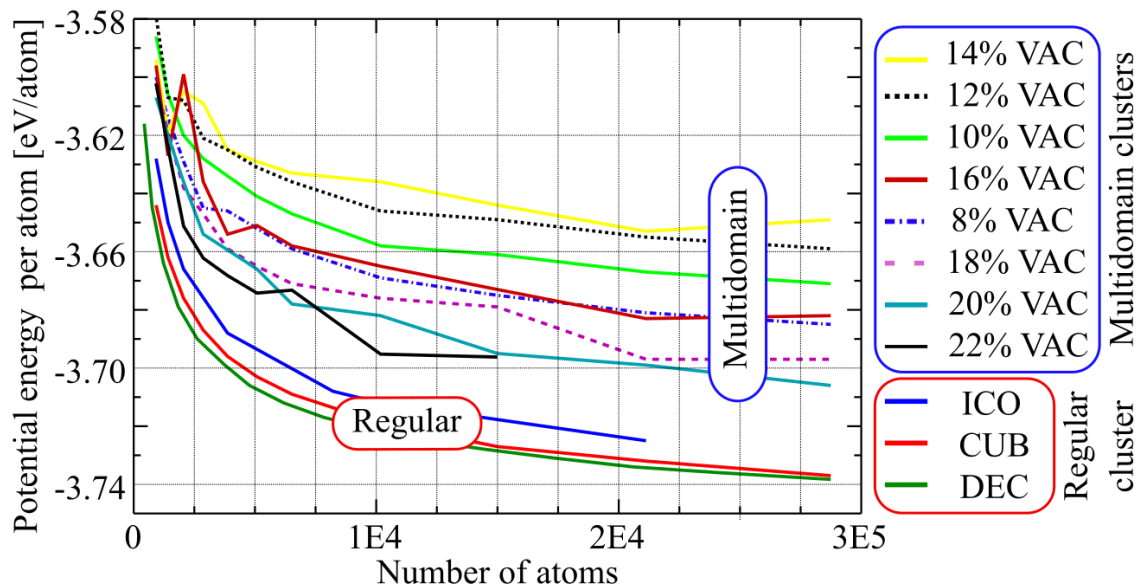


Figure 31 The minimum potential energy per atom calculated for regular and multidomain nanoparticles as a function of numbers of atoms in a cluster.

3.2.1.2 Molecular dynamics simulations

As can be seen from Figure 31 the multidomain particles have a relatively high potential energy. Therefore, if some external energy is applied to the system, making atoms more mobile, there is a chance that defects will diffuse to the surface. The diffusion of vacancies correlates with internal morphology evolution and can be simulated using molecular dynamics (MD) calculations. For a systematic study of these phenomena, a special initial model was chosen - ball cutoff of CUB with 5083 atoms. The use of a ball shape makes data analysis easier and more precise, in particular, SAXS technique is sensitive to shape of the particles. Then, nine initial models were selected with different concentration of vacancies (from 0 to 22%), relaxed, and followed by molecular dynamics calculations at 300 K. After that, the temperature was repeatedly raised and equilibrated stepwise by 50 K and MD relaxed until melting at 850 K, the duration of each step was at least 50 psec. To

avoid problems with correction for thermal expansion, prior to diffraction pattern calculation each model was relaxed.

For a detailed consideration of evolution of a multidomain particle, let's focus on a series of MD simulations of a CUB ball with 22% of vacancies (Figure 32). As can be seen from the cross sections, the relaxed model is significantly distorted and a big part of vacancies (red balls – atoms neighboring vacancies) still remains in the cluster. As the result, this structure possesses high potential energy (Figure 32 c) and only “precursor” areas of future twin planes were formed. After MD simulation at 300 K, these areas become more ordered: two stacking faults were formed and two more faults under construction. Observing evolution of the newly formed stacking faults at 300 - 550 K one can see how vacancies diffusing to the surface transform into twin planes (Figure 32 a; shown by a sequence of black circles with arrows).

If the concentration of vacancies decreases, then the overall density should grow. To verify this assumption for each multidomain model, we calculated a SAXS pattern and analyzed it in a q range $0.01 - 0.28 \text{ \AA}^{-1}$. Figure 32 b clearly shows how high temperature treatment causes diffusion of vacancies and ordering of multidomain structure, which leads to an increase in density and decrease in a mean size. However, as soon as the premelting temperature (800 K) was reached, the cluster again begins to accumulate vacancies, causing secondary twinning. This observation is in qualitative agreement with multiple and systematic experimental observations [135, 136]. The quantitative agreement requires a strategy different from the one that we have used for computational simulations.

Figure 32 c shows change in the potential energy per atom as a function of the MD temperature. It can be seen that over the entire temperature range $0 - 800 \text{ K}$, the change in the density (Figure 32 b) was correlating and proportional to the change in the potential energy (Figure 32 c). Meanwhile the decrease of the number of domains after 550 K did not violate of this proportionality. Therefore, one can conclude that the contribution of vacancies to the increase of potential energy is greater than the contribution of twin planes. If the concentration of voids is low the multidomain structure stability is comparable to that of regular ICO, DEC and CUB morphologies.

The trends described above are systematic can be observed on other models with different amount of vacancies ($0 - 20 \%$ of vacancies) in Table 7, Table 8, Table 9, Table 10:

- The higher temperature, the higher density of a cluster (Table 7);
- The improvement of density leads to decrease of the mean size (Table 8);
- Since the multidomain models are unstable, their heating leads to a crystal structure rearrangement and decrease of the number of domains (Table 9);
- The diffusion of vacancies and crystal lattice ordering lead to reduction of the potential energy per atom. Similarly to what was described above, changes in density are proportional to the changes in a potential energy (Table 10);

For all models, secondary twinning and decrease in density were observed at temperatures close to the melting point (800 K).

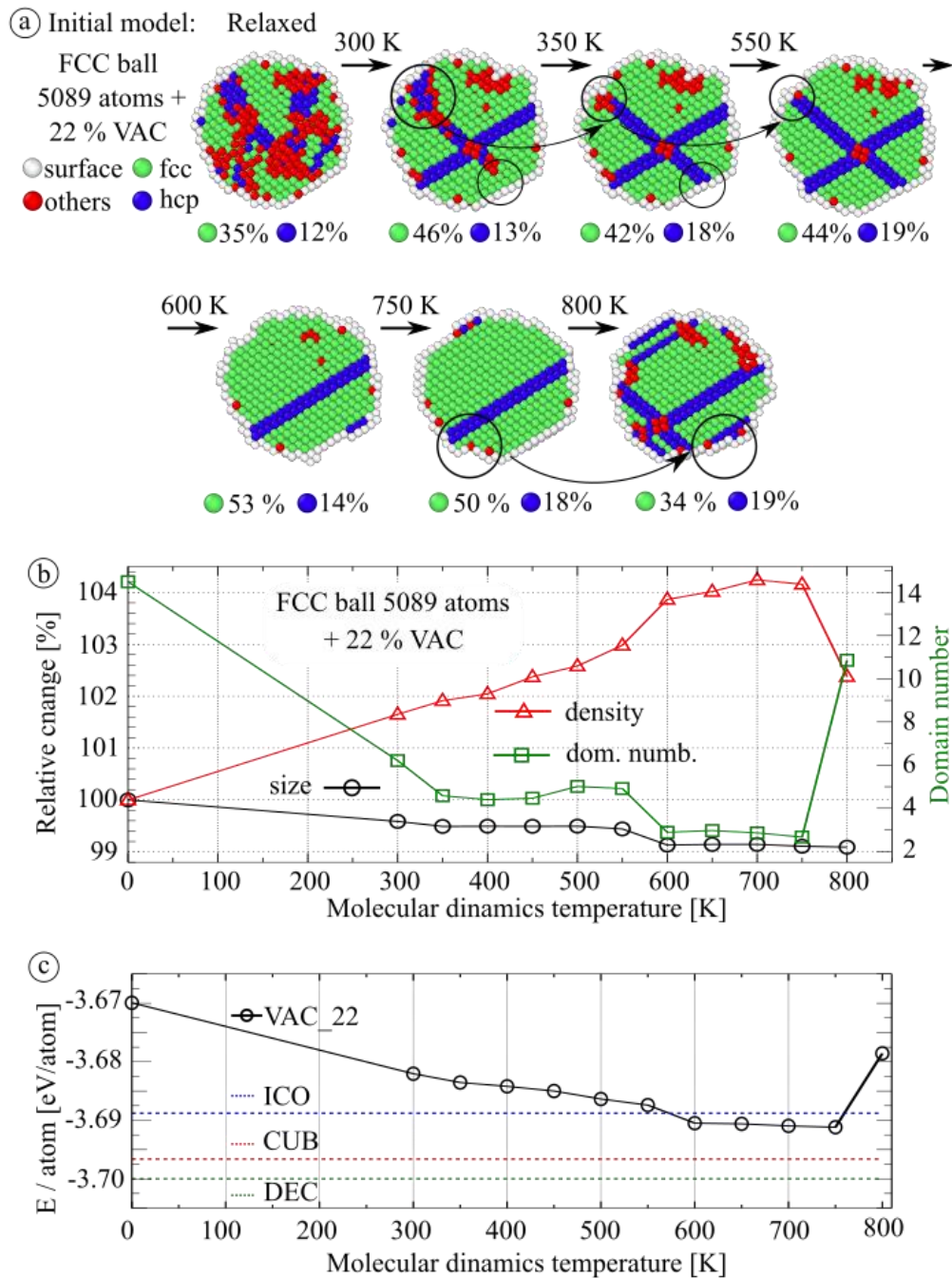


Figure 32 a) Cross sections of a CUB ball model with 22% of vacancies after relaxation and consequent MD simulations. After MD calculations, each model was relaxed, to ensure comparison of models at the same temperature; b) the left Y-axis represents relative changes in the density (red triangles, “N” parameter) and the mean size (black circles) calculated by SAXS. The right Y-axis represents the number of domains (green squares) which were calculated by MDXRD; c) This graph shows the change of the potential energy per atom of multidomain models after MD followed by the relaxation. The blue, red and green dotted lines represent the potential energy per atom of similar size ICO, CUB and DEC structures.

Change of density (SAXS)

TEMP, K	Vacancies [%]; MD + relaxation									Density scale
	0	8	10	12	14	16	18	20	22	
0	21.9	19.7	19.3	18.9	19.4	20.2	20.4	20.8	21.0	18.87
300	21.9	20.1	19.9	20.8	20.9	20.7	21.0	21.1	21.3	19.19
350	21.9	20.2	19.9	20.8	20.9	20.8	21.1	21.1	21.4	19.51
400	21.9	20.3	19.9	20.9	20.9	20.9	21.4	21.1	21.4	19.83
450	21.9	20.5	20.1	21.1	21.0			21.2	21.5	20.15
500	21.9	20.9	20.4	21.3	21.2	21.1	21.2	21.2	21.5	20.47
550	21.9	21.0	20.5	21.5	21.3	21.1	21.4	21.3	21.6	20.79
600	21.9	21.3		21.7	21.5	21.4	21.5	21.6	21.8	21.95
650	21.9	21.4	21.3	21.7	21.6	21.5	21.6	21.7	21.8	
700	21.9	21.5	21.4	21.7	21.8	21.7	21.7	21.7	21.9	
750	21.8	21.6	21.6	21.8	21.8	21.7	21.8	21.8	21.9	
800	21.6	21.8	21.7	21.7	21.9	21.6	21.9	21.8	21.5	

Table 7 Densities (N) of multidomain models were calculated on the basis of simulated SAXS patterns (q range 0.01 to 0.28 Å⁻¹)

Change of size (SAXS)

TEMP, K	Vacancies [%]; MD + relaxation									Scale size
	0	8	10	12	14	16	18	20	22	
0	27.38	27.18	27.09	27.01	26.61	26.07	25.90	25.55	25.39	25.16
300	27.38	27.12	26.87	26.53	26.23	26.04	25.79	25.49	25.28	25.47
350	27.38	27.12	26.87	26.53	26.22	26.04	25.79	25.49	25.26	25.79
400	27.38	27.05	26.87	26.53	26.22	26.02	25.79	25.49	25.26	26.11
450	27.38	26.94	26.86	26.50	26.21			25.49	25.26	26.43
500	27.38	26.88	26.81	26.41	26.20	26.02	25.78	25.48	25.26	26.75
550	27.38	26.86	26.78	26.39	26.20	26.02	25.75	25.49	25.24	27.07
600	27.38	26.82		26.32	26.15	25.98	25.72	25.47	25.17	27.39
650	27.38	26.80	26.68	26.31	26.16	25.94	25.71	25.45	25.17	
700	27.38	26.74	26.62	26.30	26.13	25.92	25.70	25.45	25.17	
750	27.39	26.70	26.56	26.29	26.11	25.89	25.66	25.42	25.16	
800	27.38	26.64	26.45	26.25	26.03	25.87	25.53	25.39	25.16	

Table 8 Mean sizes (μ [Å]) of multidomain models were calculated on the basis of simulated SAXS patterns (q range 0.01 to 0.28 Å⁻¹).

Number of domains (MDXRD)

TEMP, K	Vacancies [%]; MD + relaxation									Number of domain
	0	8	10	12	14	16	18	20	22	
0	1.0	1.1	1.2	1.3	1.5	3.3	6.6	7.9	14.5	1
300	1.0	1.0	1.1	1.1	1.7	3.1	4.1	4.2	6.2	3
350	1.0	1.0	1.1	1.1	1.7	3.3	3.4	4.3	4.6	5
400	1.0	1.1	1.1	1.1	1.7	3.1	3.4	4.3	4.4	7
450	1.0	1.4	1.1	1.1	1.7			4.2	4.5	9
500	1.0	1.6	1.0	1.6	1.7	3.0	3.5	4.4	5.0	11
550	1.0	1.6	1.0	1.0	1.7	2.8	3.4	4.3	4.9	13
600	1.0	1.0		1.0	1.8	2.9	1.9	4.5	2.9	15
650	1.1	1.1	1.1	1.1	1.9	2.7	1.6	3.8	3.0	
700	1.0	1.0	1.1	1.1	1.7	2.9	1.7	3.8	2.9	
750	1.1	1.2	1.2	1.4	2.3	3.8	2.0	3.9	2.7	
800	3.3	2.6	3.5	7.4	4.4	6.7	5.1	6.9	10.9	

Table 9 Number of domains was calculated on the basis of simulated XRD patterns by MDXRD method

Potential energy per atom [eV/atom]

TEMP, K	Vacancies [%]; relaxed models								
	0	8	10	12	14	16	18	20	22
0	-3.704	-3.656	-3.643	-3.633	-3.644	-3.665	-3.663	-3.672	-3.670
300	-3.704	-3.667	-3.664	-3.673	-3.678	-3.676	-3.677	-3.681	-3.682
350	-3.704	-3.669	-3.665	-3.674	-3.678	-3.677	-3.679	-3.681	-3.684
400	-3.704	-3.672	-3.667	-3.675	-3.679	-3.679	-3.680	-3.682	-3.684
450	-3.704	-3.676	-3.669	-3.677	-3.680			-3.683	-3.685
500	-3.703	-3.682	-3.674	-3.681	-3.683	-3.682	-3.682	-3.684	-3.686
550	-3.703	-3.685	-3.678	-3.685	-3.684	-3.683	-3.684	-3.686	-3.687
600	-3.703	-3.689		-3.689	-3.688	-3.686	-3.687	-3.689	-3.690
650	-3.702	-3.690	-3.686	-3.689	-3.688	-3.689	-3.687	-3.690	-3.691
700	-3.701	-3.691	-3.687	-3.690	-3.690	-3.690	-3.688	-3.691	-3.691
750	-3.699	-3.693	-3.691	-3.691	-3.691	-3.685	-3.689	-3.690	-3.691
800	-3.695	-3.692	-3.691	-3.685	-3.690	-3.685	-3.688	-3.685	-3.679

Table 10 Potential energies per atom were calculated by the Cluster program.

From Table 9 one can notice one more feature. The lowest critical concentration of vacancies necessary to trigger twinning can be below 13%. The partial twinning may occur at 450 – 550 K for the model with only 8% of vacancies. The explanation is simple. Increasing the temperature of the system improved the mobility of atoms and diffusion of vacancies, so less free space was required to initiate the cascade motion of atoms. This means that in reality, the concentration of vacancies necessary for twinning initiation can be lower than 13% because this value was calculated for the relaxed models.

3.2.1.1 Condensation of atoms

The processes demonstrated above describe the diffusion of vacancies. However, in real life, prior to diffusion these vacancies must be created. We propose to extend the model of simple condensation of atoms on a seed by adding an intermediate step – accumulation of vacancies (Figure 33). It is easy to imagine that, during the condensation, the newly deposited atoms occupy non-optimal position- away of the lattice node. If the number of such lattice faults continues to grow, it will eventually lead to the formation of voids. In the context of vacancies driven twinning, we propose to use voids and vacancies as equivalent terms. As the result of an initial condensation, the mean size of particles increases while the density decreases. These two features are fingerprints of the accumulation of vacancies.

After some time and/or after the supply of additional energy (in form of X-rays or electron beams, heating etc.), the newly condensed atoms can arrive at an energetically favorable position. This process triggers the diffusion of vacancies to the surface. The most important aspect of this step is the improvement of the density resulting in decrease of the mean size. These two features are the fingerprints of vacancies release which was described in detail in the previous chapter.

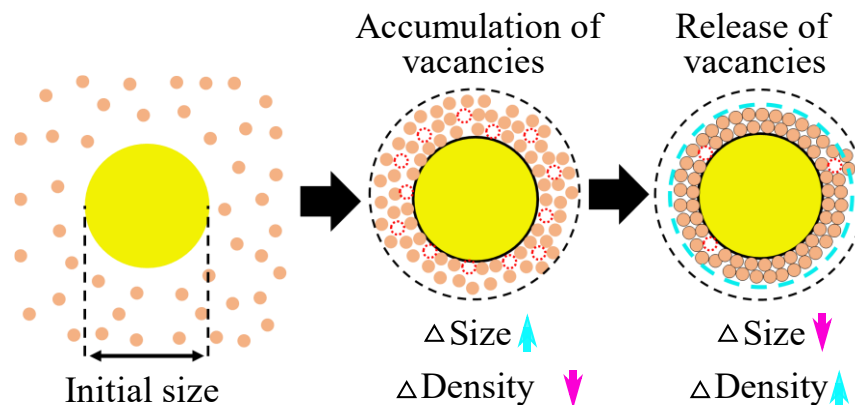


Figure 33 The scheme of atoms condensation on the seed. During condensation, the newly deposited atoms cannot find the optimal position creating voids (aka vacancies). After some time, atoms occupy more energetically favorable positions, causing the release of vacancies.

To verify the vacancies driven concept, the first step is to observe vacancies. Direct observation of them is impossible because vacancies are voids and has no physical parameters. Therefore only related parameters can be measured: density and size of the particles. By monitoring the relative changes of these fingerprints one can differentiate between accumulation and release of vacancies.

3.2.2 Experimental observations: ex-situ heating

The observation of vacancies accumulation is a complicate tasks because it is necessary to simultaneously monitor changes of the density and of the mean size during the particle growth. However, the release of vacancies does not require such complex observations. It is enough to limit all growth processes and trigger the release of vacancies by e.g. a heating. If nanoparticles are well protected and stabilized the release of vacancies should lead to decrease of the mean size, which can be noticed on TEM images.

3.2.2.1 Au@PVP@SiO₂ (TEM + XRD + SAXS)

To fulfill the above requirements, a special Au@PVP@SiO₂ sample was prepared (Figure 34). Au NPs were stabilized by PVP and encapsulated in SiO₂. Then, this sample was placed in a quartz U-shaped reactor (Volume ~12 ml) and was heated stepwise from 200 to 800°C (with a step of 100°C) in He atmosphere (flowrate 5 ml / min). To ensure achievement of the equilibrium state the duration of each step was ~120 hours (about 5 days). At the end of each step the system was cooled down to room temperature and a small fraction of the sample was collected for the analysis. After sample collection, prior to heating, the system was purged with He (flowrate 40 ml/min) for ~15-20 min. The total duration of the experiment was almost 36 days. The detailed information about all samples can be found in chapter 2.1.2.

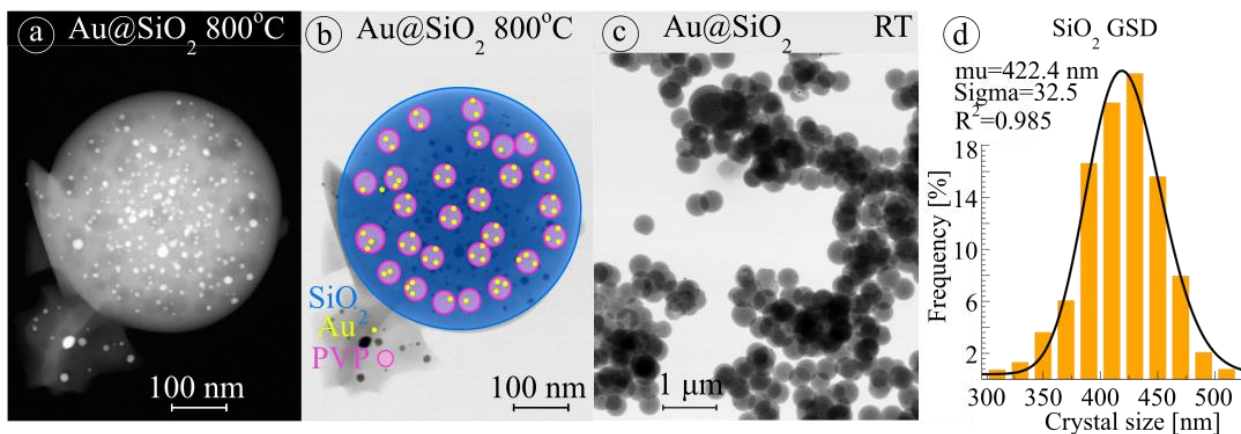


Figure 34 a) Dark-field and b) bright-field TEM of the Au@SiO₂ sample after high temperature treatment at 800°C; c) Bright-field TEM of as-synthesized Au@PVP@SiO₂ sample ; d) grain size distribution of SiO₂ spheres

Since TEM analysis provides a direct measurement of NP sizes, the unambiguous observation of vacancies diffusion can be performed using microscopy analysis. As can be seen from Table 11, the initial mean size of Au NPs was 6.71 nm. After the heat treatment at 400°C, the mean size was reduced by 0.37 nm. This difference is significant because at least 1200 particles were analyzed for corresponding grain size distribution (GSD) analysis. Despite a small growth of the mean size after heating at 500°C, the mean size was still smaller than the initial one (Table 11).

Au@PVP@SiO ₂	MDXRD		TEM		SAXS		
	Num. Dom.	Volume Weighted Size [nm]	Num. Dom.	Volume Weighted size [nm]	Num. Dom.	Volume weighted size [nm]	Density (N)
Room Temp.	4.46	7.09	4.01	6.71	4.33	6.98	7.1E-5
200°C	3.64	6.78	-	-	3.41	6.57	1.5E-4
300°C	3.45	6.77	-	-	3.39	6.72	1.5E-4
400°C	2.96	5.83	3.56	6.34	3.98	6.70	2.3E-4
500°C	3.08	6.94	2.58	6.44	2.61	6.47	1.9E-4
600°C	2.92	6.91	2.75	6.74	2.72	6.71	2.1E-4
800°C	4.01	19.03	-	7.24	-	9.23	1.3E-4

Table 11 Results of analysis of volume weighted size and average domain number of Au@PVP@SiO₂ nanoparticles after a high temperature treatment. More information about TEM and SAXS analysis details can be found in chapter 2.2.

The decrease of the mean sizes with temperature is also confirmed by SAXS analysis. However, due to the presence of SiO₂ sphere with a regular size distribution, the small angle diffraction pattern of NPs overlaps with the SiO₂ pattern. This obstacle should not significantly affect accuracy because centers of these two patterns are well separated due to the big sizes of silica spheres (422.4 nm). In any case, the difference of the mean size of Au NPs at room temperature and after heat treatment at 500°C is equal to 0.51 nm, which is substantial. Additionally, one can see the improvement of the density (by SAXS analysis) with increasing temperature. Some inconsistency of the density changes can be caused by few factors. First, there was no control over the density of powder sample bed in the sample holder. Secondly, since the samples were taken at different temperatures the overall composition was slightly different (because of decomposition processes).

As can be seen from Table 11, the MDXRD approach also points to decrease of the mean size with temperature. In general, for all samples in the temperature range 23 - 600°C there is reasonable correlation between mean size estimations performed by MDXRD, SAXS and TEM. It should also be noted that all techniques show a decrease of the average number of domains with temperature, and these results are consistent. The disagreement appears after the heat treatment at 800°C. As was mentioned earlier, at this temperature the stabilizing PVP agent is decomposing and SiO₂ spheres

become less stable. As a result, Au NPs began to merge supplying the high size tail in the grain size distribution. This phenomenon causes disagreement in data analysis because each technique is sensitive to different parameters.

Although the results of MDXRD, SAXS and TEM are sensitive to different parameters, the trends derived from them are systematic and in good agreement. The decrease of the mean size and growth of the density with temperature are fingerprints of the release of vacancies. It is difficult to explain the observed changes in another way.

3.2.3 Experimental observations: effect of X-ray

X-ray based techniques are often considered as non-destructive, regardless the well-known fact that synchrotron radiation causes a radiation damage [137]. Nevertheless, laboratory X-ray diffractometers have not been acknowledged as destructive devices because of the low intensity comparing to the synchrotron sources. However, in fact, a low X-ray flux doesn't mean that the radiation damage is absent.

In the specialized X-ray laboratories researchers sometimes uses glass sample holders. If these samples holders are old enough, one can notice the appearance of dark spots inside the bulk of holders. Our experiments with long time exposure to laboratory Cu X-rays can clearly demonstrate this effect (Figure 35). These sample holders show dark "crosses" formed by the rectangular X-ray beam. One rectangle spot corresponds to approximately one month of continuous X-ray exposure. Moreover during X-ray irradiation, these holders were always filled with NPs, therefore most of X-rays was absorbed by NPs and supporting material. If glass suffers from radiation damage, the NPs must also be affected.

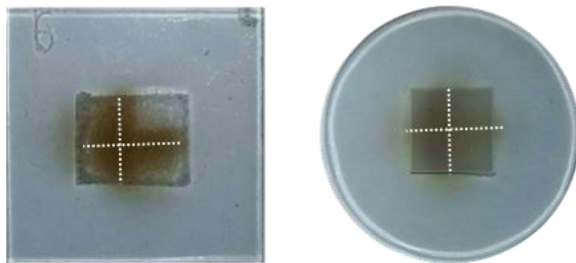


Figure 35 Two glass samples holders after months of continuous X-ray exposure. Dark rectangular spots form a cross because of a different sample holder positions during different long-term measurements. In other words, one rectangle like spot correspond to the one experiment. The contrast of pictures was artificially increased by ~20%.

Since radiation damage from laboratory X-rays is considered to be small, it should result in subtle changes in the irradiated sample. Therefore, we expect these changes to be more pronounced for nanoparticles than for macroscopic samples. To investigate this phenomenon, we synthesized small Au@PVP NPs (average size 1.8 nm), continuously and repeatably measured their diffraction pattern using a laboratory diffractometer with Cu X-ray tube (40 mA; 40 kV). Duration of the X-ray exposure steps was set schematically as the results could not be predicted. In total, three sets of experiments were performed (Figure 36).

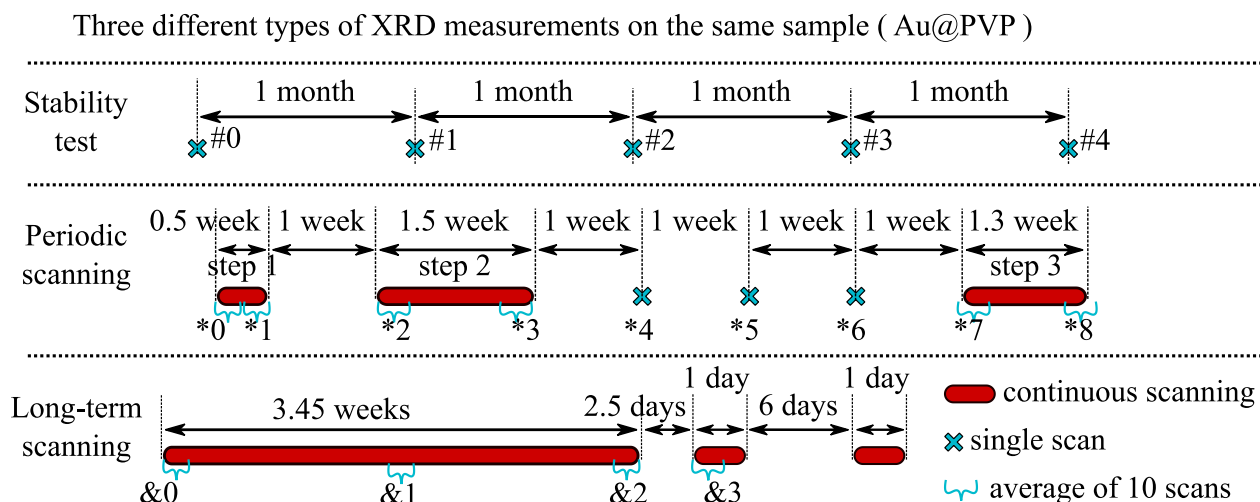


Figure 36 Scheme of experiments with Au@PVP NPs. The same Au@PVP samples were exposed to the laboratory Cu X-rays at different times and for various duration of the irradiation.

The initial Au@PVP catalyst was divided into three parts and each part was placed in its own glass sample holder. Every time after a continuous or single scanning, the sample holder was removed from the stage and stored inside the diffractometer box in a Petri dish. The temperature in the room was maintained by air conditioning. I.e. all samples were stored at the same environmental condition (room temperature, air, exposure to light, dust protection ...). The amount of material placed in the sample holders and density of the sample bed remained constant (except for one collection of small amounts of material during the periodic scanning). Thus, within a given type of measurement, it is possible to directly compare the absolute values of XRD analysis results. The only source of error is a possibly non-identical positioning of the sample in the holder during its mounting on the stage after breaks.

The analysis of NPs diffraction patterns is not always straightforward. Diffraction peaks are broad, they may overlap and internal strains can also affect the lattice parameters. Therefore, to improve the accuracy of analysis, the initial sample was mixed with an aliquot of polycrystalline quartz serving as the internal standard.

3.2.3.1 Laboratory X-ray: Stability test

Before analyzing the effect of X-ray damage, it is necessary to check the stability of synthesized NPs. In other words, to make a reference test. The initial Au@PVP sample was placed in a sample holder and was scanned once a month (Figure 36 “Stability test”) for 4 months.

To assess the stability of NPs, one has to compare corresponding 5 XRD patterns. The problem is that typical analysis by fitting diffraction peaks by analytical functions is not accurate. As previously mentioned, it is a complicated task due to the broadening and overlapping of diffraction

peaks. Therefore, an alternative method can be used. Since the amount of the sample and its bed density remain the same, the diffraction patterns can be directly compared. Figure 37 shows the difference of XRD patterns in different periods of aging (Figure 36). Two types of changes can be determined. The first one is a change of PVP (green dotted line). The second one is a change of crystalline phase near 111 and 200 peaks.

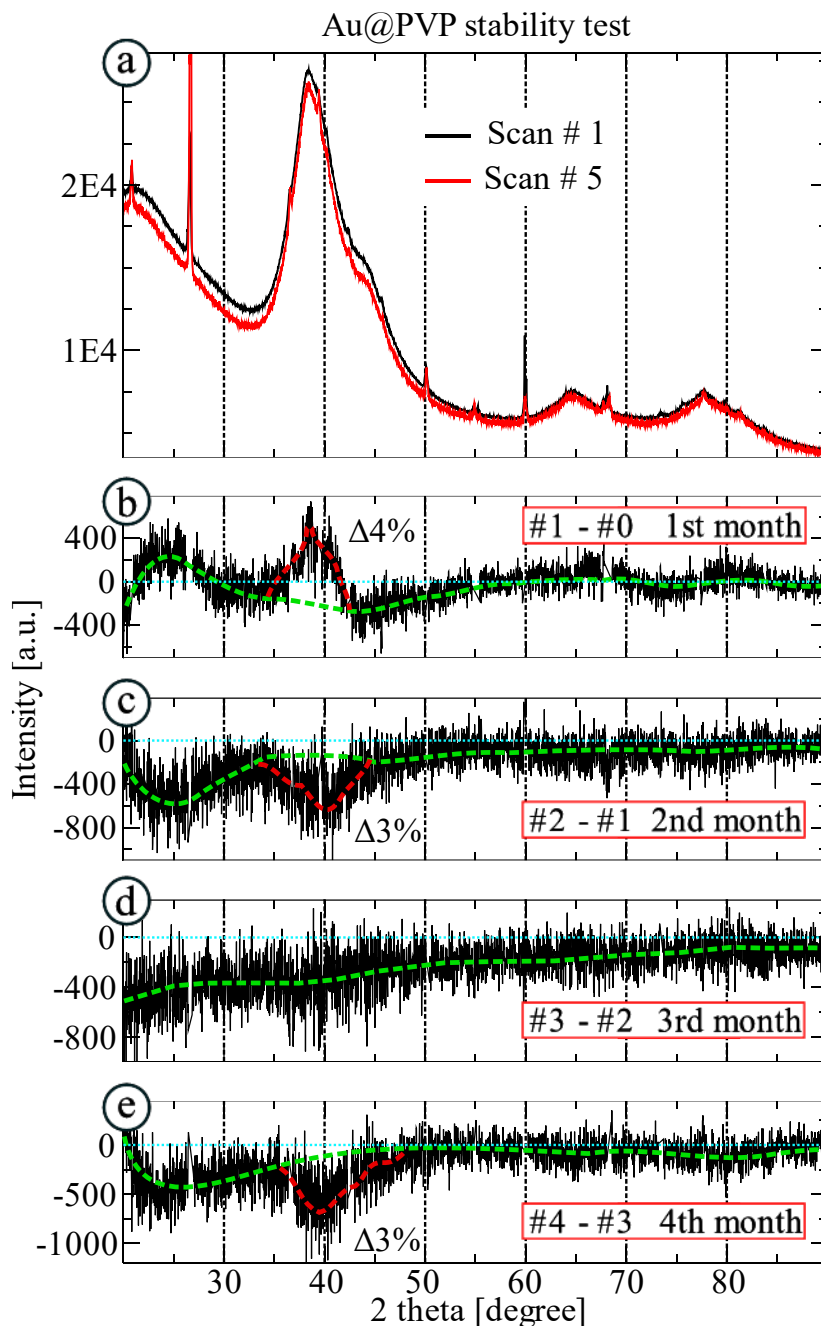


Figure 37 a) The graph shows XRD patterns of the initial Au@PVP sample and after 4 months of the aging. Four graphs below (b-e) show the differences of diffraction patterns of samples during different period of time. The green dotted line indicates the change of PVP, the red dotted line correspond to a change of the crystalline phase.

Nevertheless these changes are subtle and corresponding patterns are noisy. It's difficult to conclude whether it's the effect of aging or effect of a sample holder misplacement. After the first and second months, opposite changes were observed. Therefore, it can be expected that the sample is unstable and at least some changes should appear after the third month. However, nothing happened, Figure 37 **d** clearly shows only small changes in the background. All the patterns have normalized total intensity to correct for a possible primary beam instability.

Some traces of the aging process can be visible, but its effect is comparable to the error caused by the sample holder displacement. The comparison of the initial and the 4-month-old diffraction patterns (Figure 37 **a**) does not reveal significant changes of peak profiles. Therefore, one can conclude that Au@PVP NPs are quite stable at room temperature. In other words, any change of NPs during X-ray exposure tests can be considered as a consequence of radiation damage.

3.2.3.1 Laboratory X-ray: periodic scanning

The scheme of the periodic scanning measurements can be found in Figure 36, while results are summarized in Figure 38. It is clearly seen from this figure that X-rays cause some structural changes in NPs. All diffraction peak parameters are changing with time: heights, widths and positions of peaks. Additionally, TEM and SAXS analysis confirms that these are real structural changes and not the XRD analysis artifacts.

Detailed analysis of Figure 38 shows that two scenarios of structural changes may take place: when the height of 111 peak increases (1st and 2nd steps) or when it decreases (step 3). It is interesting to note that steps 1 and 2 are almost identical. In both cases, the height of 111 peak is slowly increases, while 220 FWHM and the number of domains decreases. As discussed earlier (Chapter 3.1.2.3) FWHM of the 220 peak can be used as an indicator of the average domain size, showing its slow growth. Figure 38 shows that the average number of domains during X-ray exposure remains the same/slightly decreases. At the same time the mean size of NPs is growing. Such growth mechanism is similar to a template growth which is typical for Ostwald ripening or condensation of very small clusters on the seed.

These growth mechanisms should lead to the disappearance of small particles and enlargement of big clusters. Analysis of the XRD patterns difference at the beginning and at the end of each exposure step revealed one interesting feature (Figure 39 **b** differences “*1-*0” and **d** “*3-*2”). Closer to 40-degree, S-shaped oscillation of height can be observed. The presence of negative and positive parts can be explained in two ways. It is known that appearance of highly strained structures results in shortening of the distance between 111 and 200 peaks, and forming a “bridge” intensity in between. Therefore, if the strains were relaxed, it may lead to decrease of intensity between 111 and 200 and increase of intensity to the sides of the “bridge”. Another explanation is that small particles disappeared (creating a negative part) and were reabsorbed in one form or another by the larger particles (growth of a positive part).

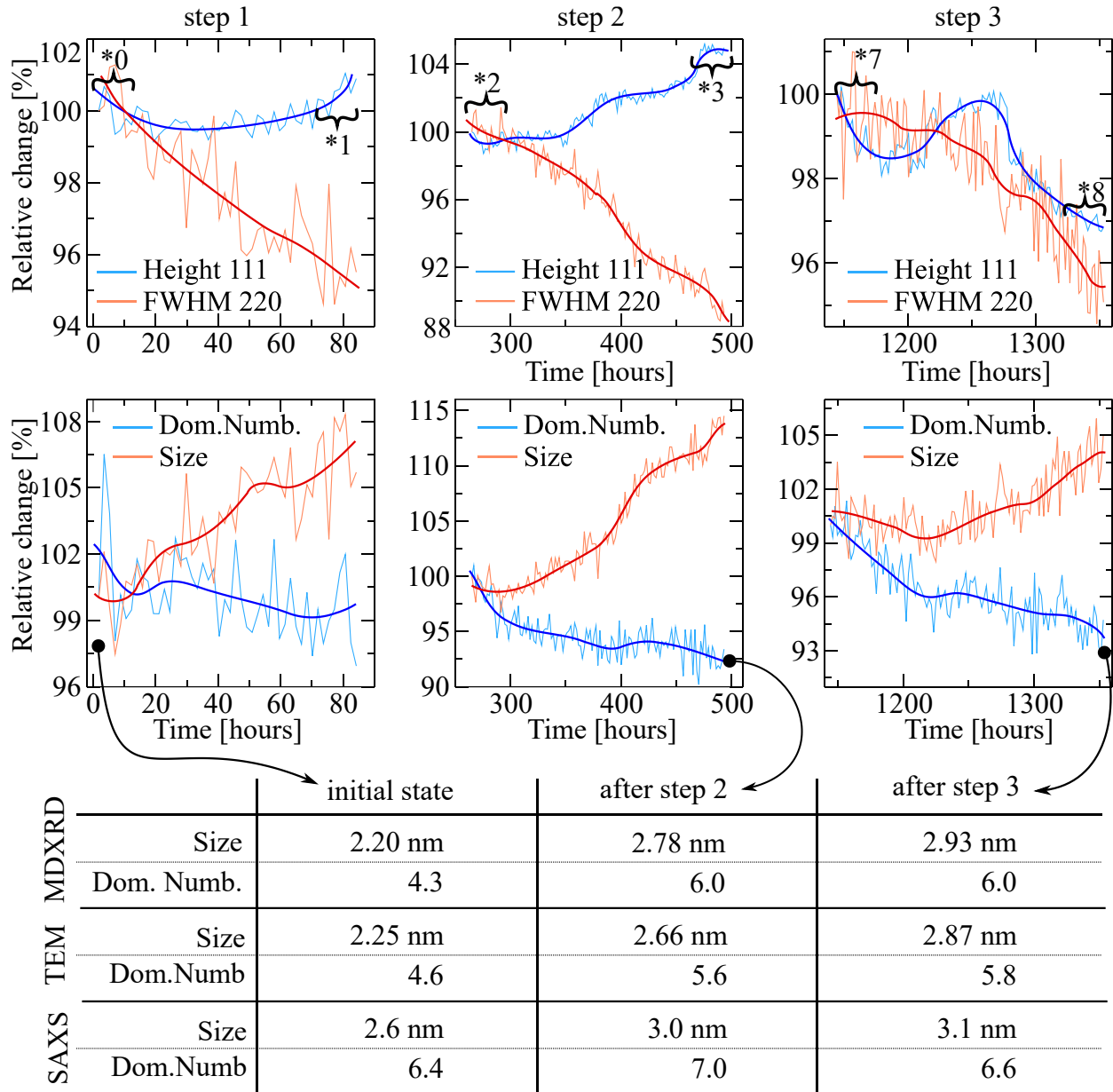


Figure 38 The results of Au@PVP NPs evolution under continuous exposure to laboratory Cu X-rays: step one ~ 86 hours of X-ray exposure (49 XRD scans) and 179 hours break; step two ~ 228 hours of X-ray exposure (131 XRD scans) and 651 hours break; step three ~ 209 hours of X-ray exposure (120 XRD scans). Three samples (the initial one - *0, after the step two - *3 and after the step three - *8) were additionally analyzed by SAXS and TEM techniques. The numbers in black brackets indicate the points, which are in detail analyzed in Figure 39. To improve the signal-to-noise ratio, each point was calculated as the average from 10 neighboring XRD patterns.

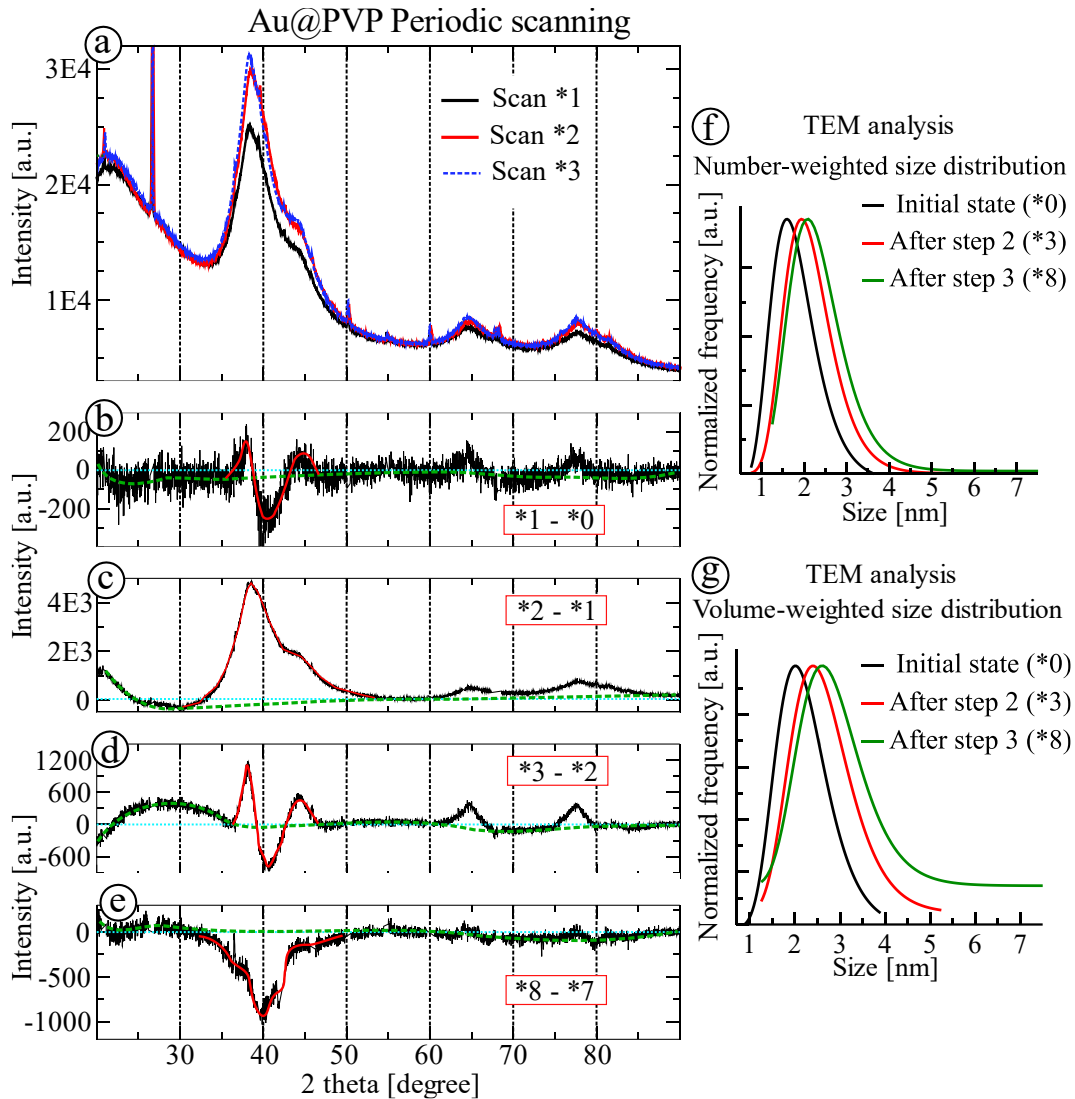


Figure 39 a) The graph shows averaged XRD patterns of Au@PVP at the different steps of the periodic scanning: at the end of step 1 (black line); at the beginning and end of step 2 (red and blue lines respectively). The four graphs below (b – e) represent differences of diffraction patterns at various stages. The green dotted line highlights the change of PVP, the red dotted line corresponds to a change of the crystalline phase. TEM analysis (f-g) shows the corresponding grain size distributions.

It is important to note that, in some cases, the structural evolution of NPs continues after the X-ray beam is turned off. As can be seen from Figure 39 c, after 86 hours of X-ray irradiation (step 1), after the 179 hours break, the X-ray diffraction pattern becomes more intensive. This dramatic change cannot be explained by the change in position of the sample holder. Moreover, MDXRD showed that after this break, the average domain number increased from 4.5 (end of the step one - *1) to 6.2 domains (beginning of the step two - *2), and the mean size increased from 2.1 nm to 2.6 nm (MDXRD). This means that 86 hours of exposure initiated serious changes in the NPs.

Step 2 (228 hours) did not result in a fundamental change. Although the X-ray beam damage was better noticeable compared to step 1 (Figure 39 **d** difference “*3-*2”), it did not lead to a rapid NPs growth. A week after the end of step 2, a single XRD scanning (“*4”) was performed to analyze structural changes after the long exposure to X-ray beam. Surprisingly, the changes were barely noticeable. After some time, single scan measurements were repeated several times (points *5, *6). The result was the same – the absence of any visible structural changes. Probably, after the very intensive step 1, the amount of material available for the further coalescence/condensation/ripening was depleted.

The analysis of the step 3 data confirms this statement. The duration of this step was 209 hours, but it did not cause a size growth as previously. According to TEM the mean size changed from 2.78 to 2.93 nm. In addition, the diffraction pattern difference contains only negative part (Figure 39). The exact interpretation of this observation strongly depends on understanding of the effect of radiation damage on NPs. Since the fundamental understanding of radiation damage is currently poor, an exact explanation is difficult. Nevertheless, the growth of NPs under the action of X-rays is a fact (Figure 38), and there must be a mechanism controlling it.

3.2.3.2 Laboratory X-ray: Long-term scanning

For the long time X-ray exposure experiments the same Au@PVP sample was used. However, this experiment was performed almost six months after the end of the previous measurements. Therefore, the initial state of the sample, in particular mean size (~2.35 nm) and number of domains (5.4) are different compared to the initial state of the sample in previous tests (2.2 nm; number of domains ~ 4.4). There is also a fundamental difference in the strategy of the experiment. Despite pauses in the X-ray exposure, the sample holder was never moved from the stage. Therefore, the effect of the sample holder position change is negligible.

From Figure 40 **a** one can see the long time stepwise decrease of the height of 111 peak followed by increase before and after the breaks. If one compare this measurement and the periodic scanning test (Figure 38) the different trends can be noticed. The long-term scanning starts with decrease of 111 peak height, in contrast to the periodic scanning. Probably, it is caused by different density of the sample beds, because for the long-term test the sample bed was quite loose.

The 111 peak height decreases stepwise: from 0 to 130 hours, it decreases by ~4%, over the next 120 hours the 111 peak height oscillates resulting in a net 0% change, followed by ~4% decrease during the next 250 hours. After 480 hours of the X-ray exposure the 111 height is rising.

Despite the continuous decrease of the 111 height, the 220 height behaves differently. Using MDXRD (equation 32), the average number of domains can be obtained by analyzing the 220/111 height ratio (Figure 40 **b**). At the very beginning of the test, the number of domains decreases (blue arrow), but after 300 hours the number of domains started to grow. It can be interpreted as an observation of twinning, but the effect is weak and requires further substantiation.

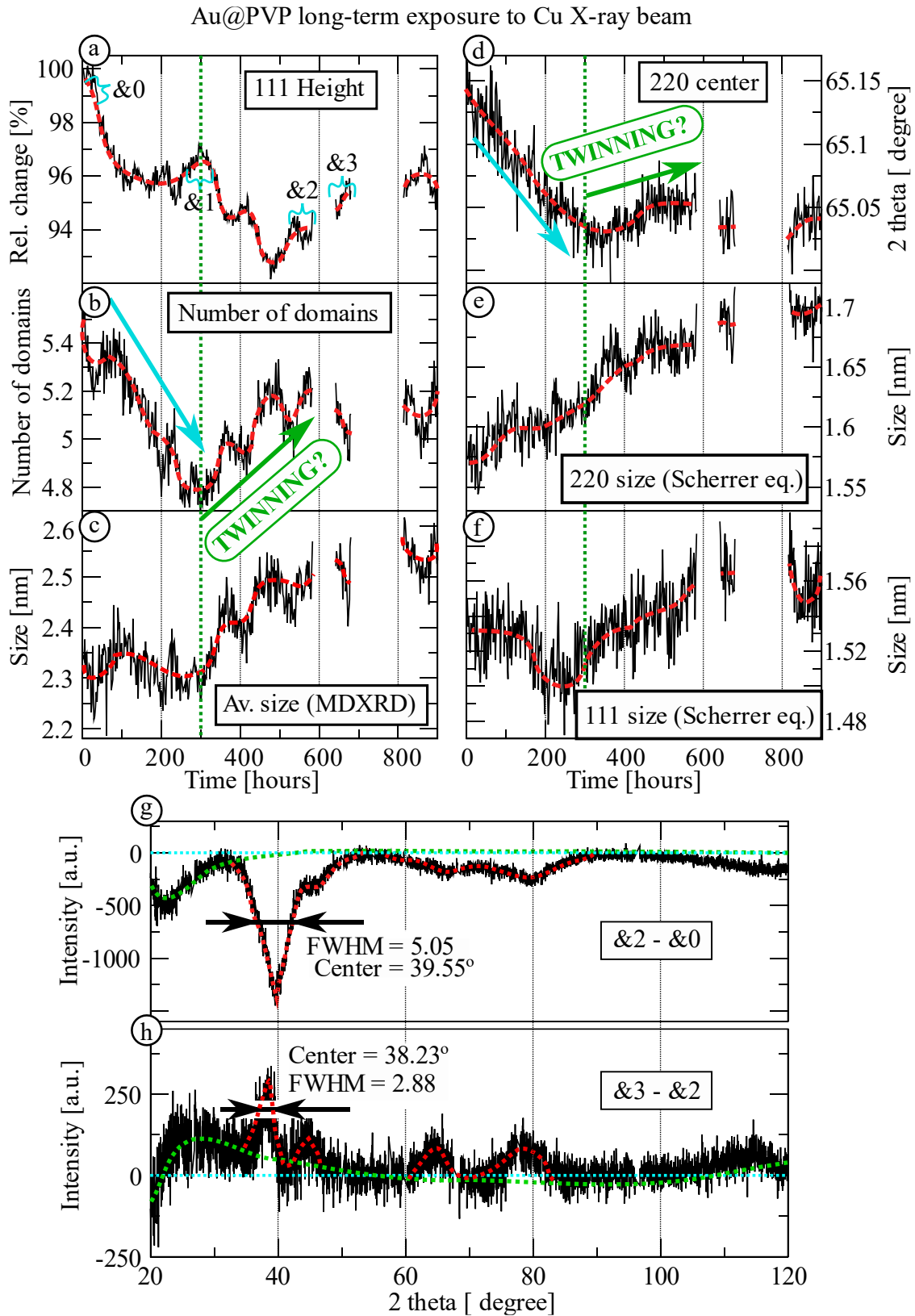


Figure 40 Results of the long-time X-ray beam exposure of Au@PVP nanoparticles

Figure 40 c shows the growth of the mean size after the twinning, which agrees with the increase of mean size calculated by Scherrer equation applied to 111 peak (Figure 40 f). During the accumulation of vacancies (0 – 300 hours), the number of domains decreases and compensates for the growth of the average domain size (Figure 40 e). However, when the number of vacancies exceeds a certain level, the twinning occurs, resulting in a change of peaks ratio. Probably, the rise of an average domain number is of stepwise nature (not monotonic) because both processes (accumulation and release of vacancies) happen simultaneously. In addition, the system contains many individual NPs whose structure evolutions are not synchronized.

The above-mentioned explanation is inconsistent with observations of the 220 peak position evolution (Figure 40 c). The simple accumulation of vacancies, as follows from Figure 27, leads to the contraction of the lattice constant, which leads to the shift of all diffraction peaks to the right-hand side. However, Figure 40 d clearly shows that 220 peak (during the initial ~300 hours period) and all other peaks are shifted towards lower angles. Further discussion will be focused on the 220 peak because it is less overlapped with other peaks which make the analysis more accurate.

It is likely that the left-hand side shift of peaks is caused not by vacancies, but by something else. First of all, the growth of the mean size of NPs under X-rays is a fact. Secondly, since the number of domains does not change significantly, the dominant growth mechanism is the Ostwald ripening/condensation of atoms. If the X-ray beam triggers depletion of small atoms (Ostwald ripening or coalescence), it must affect the diffraction pattern in a special way. The difference of the diffraction patterns (&2 - &0) shows the disappearance of small NPs (Figure 40 g, FWHM = 5.5) and some solidification of newly formed material (Figure 40 h, FWHM = 2.9) after turning off the X-ray beam (&3 - &2). These phenomena also took place during the previous periodic scanning experiment (Figure 39). However, they are difficult to monitor from the difference of XRD patterns, since depletion (negative part) and solidification (positive part) occur simultaneously.

Nevertheless, the described redistribution of nanoparticle sizes is well visible from TEM analysis (Figure 39 f and g). Additionally from Figure 40 h and g one can see different positions of 111 peaks. The depleted fraction has a smaller lattice constant and its diffraction patterns is shifted toward high angles. Therefore it can be assumed that 220 peak evolution (during the initial ~300 hours period) is caused by the disappearance of the high angle contribution from the small size fraction. The absence of further 220 evolution (after expected twinning) can be explained by analyzing two differences of XRD patterns (&1 - &0 and &2 - &1). During the first 160 hours the 111 height decreased by 74.3% of the total decrease (&2 - &0), and then the decrease slowed down. Probably the twinning was somehow suppressed by a side process during the depletion and once depletion effect became weaker the twinning occurred. The problem is that the depletion effect itself is studied purely, and in order to better interpret the observed evolution of morphology, one needs to better understand the elementary interaction between nanoparticles and X-rays.

The long-term experiment suffers from the bad time resolution. Over such a long time, the sample can undergo serious changes. As a result drawing of final conclusions is a difficult task. Nevertheless the principal problem can be illuminated by increasing the intensity of the incoming X-ray beam.

3.2.3.3 Synchrotron X-ray

Using the intensive synchrotron radiation the NPs evolution can be triggered immediately and monitored by various techniques. The combination of wide and small angle X-ray scattering (WAXS and SAXS) is especially promising for the vacancy detection. SAXS provides information about the mean size and density of a sample, while WAXS is sensitive to the interior of NPs.

For experiments with synchrotron radiation, the same Au@PVP sample was used. From Figure 41 a one can see the change of 111 peak height caused by low X-ray flux (the blue line). During the first 15 minutes, a rapid decrease of the 111 height was observed, accompanied by decrease of average number of domains and left hand-side shift of 111 peak position (Figure 41 c and e). All these observations (except the right-hand side shift of 220 peak, Figure 41 f are like in the previous experiment with the periodic scanning and can be interpreted as the accumulation of vacancies. Unfortunately, there is no good quality SAXS data for these first 15 min because of problem with filters lowering the beam flux. During the first 15 min, most of WAXS and SAXS patterns are of poor quality. Only some of the WAXS data (with good noise – signal ratio) was corrected by scaling the background line and included into analysis.

After the initial 15 min exposure to the low flux X-ray beam, the profile of the 111 height evolution is very similar to the profile obtained by using the laboratory setup (Figure 40 a): the initial 4% decay of the height, followed by a plateau and subsequent ~4% decay. However, this time the 220 peak position is slowly moving to the right-hand side. The position of the experimental diffraction peak (assuming the same material and no contaminations) can vary depending on a number of factors: concentration of vacancies, degree of twinning, mean size of NPs, change of elastic strains and temperature (in this case, only heating is possible). Among all these factors, only accumulation of vacancies and twinning can cause a right-hand side shift. Comparing the changes of the number of domains triggered by the high and low flux (Figure 41 c) one can see that in case of the low flux, the twinning effect is weaker. Therefore, the main reason of the 220 peak shift (at the low X-ray flux) is rather accumulation of vacancies than twinning. The fingerprints of vacancies generation were detected using SAXS: during the entire period of X-ray exposure, the density (N) decreases, while the mean size is growing as shown in Figure 33.

Despite the apparent similarities of the low flux synchrotron and laboratory measurements, they have principle differences. As can be seen from Figure 41 c, the number of domains began to noticeable grow after 15 minutes of the exposure. The amplitude of the change is significant compared to the evolution during the laboratory experiment (Figure 40 a). It is possible that the quick increase of the number of domains was caused by intense coalescence triggered by the heating effect of the synchrotron beam and/or simultaneous decomposition of the supporting PVP material. Nevertheless, since the 111 peak height was only decreasing, the newly formed multidomain structures were not ordered. Interestingly, the 200 peak position (Figure 41 g) continuously moves toward 111 peak (to the low angles). The 200 peak is very sensitive to the strains (Chapter 3.1.2.1), and the closer it is to the 111 peak the stronger strains are. Therefore, the newly formed particles are highly strained.

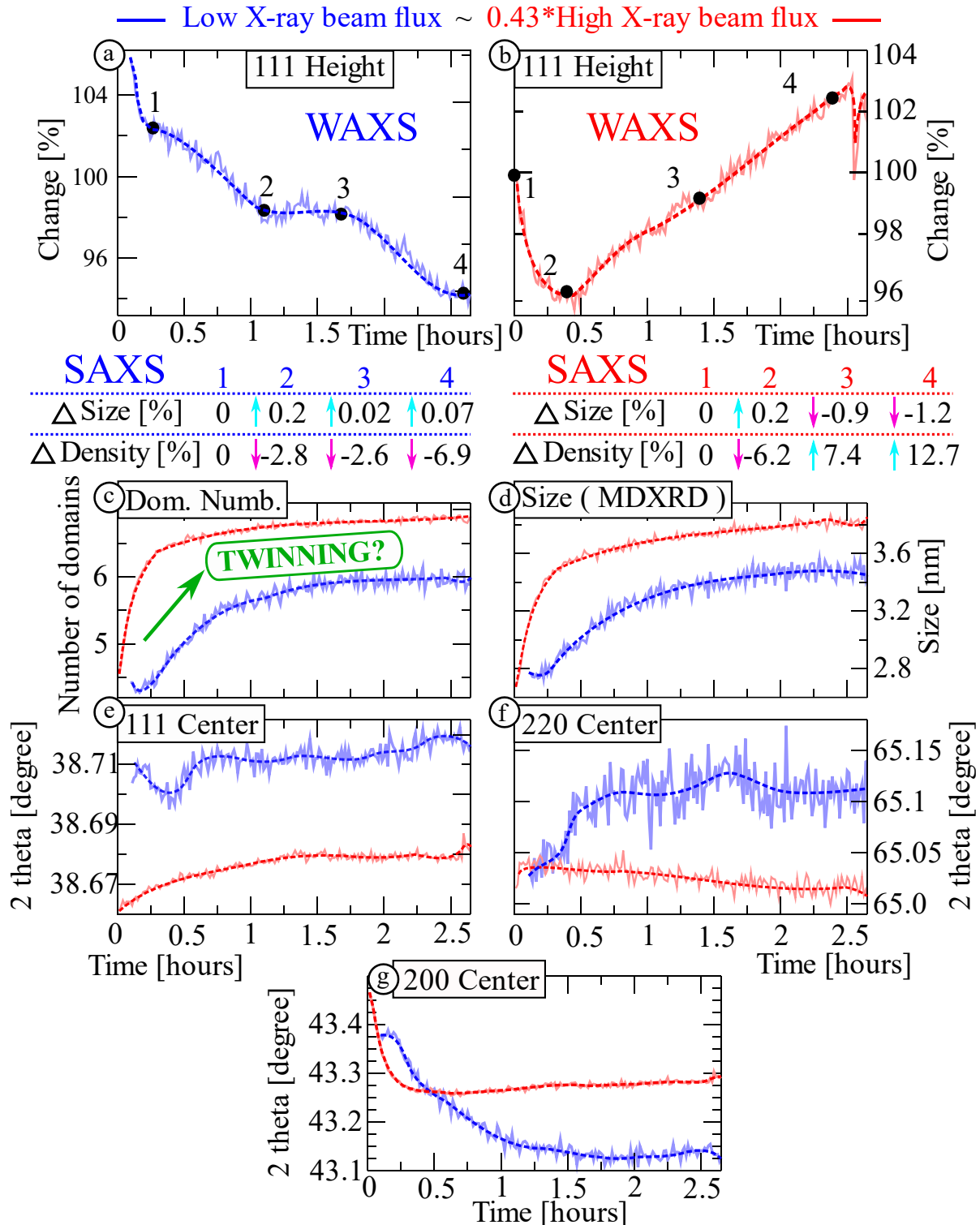


Figure 41 Results of the synchrotron X-ray beam (~ 12 keV) irradiation of Au@PVP NPs. Measurements using high X-ray flux give results in red, while measurements using low X-ray flux give results shown in blue.

The growth of the mean size of NPs under influence of X-ray is a fact, but it is necessary to define which growth mechanism is the dominant. From one point of view, coalescence can explain the rapid growth of the number of domains. However, the SAXS analysis shows very subtle change of the mean size, which is difficult to imagine if coalescence is running. Meanwhile, Ostwald ripening/condensation of small clusters can explain the slow growth of the mean size. If so, then the origin of intensive twinning is not clear. Probably the intense X-ray flux, similarly to electron beam, can cause ordering of the multidomain structure.

In the case of high X-ray beam flux (see Figure 41 **b**), the 111 peak height evolution is different. The initial 25 minutes decrease of the 111 height is followed by continuous linear increase. At the initial stage, the number of domains rapidly increases from 4.5 to ~ 6.5. These initial changes are similar to those measured at the low X-ray flux, although the key difference appears after 25 min. The growth of 111 peak height means that the newly formed domains are ordered, which is confirmed by the SAXS technique. Small angle X-ray scattering revealed increase of the density and decrease of the mean size. These two observations are fingerprints of the diffusion of vacancies.

It seems that the difference in ordering under the low and high flux is related to the effect of the X-ray beam flux. The more intense the beam, the higher the degree of ordering. In other words, the source of intense twinning at the initial stages of X-ray exposure tests is not coalescence, but the X-ray beam itself. If so, then it is more likely that Ostwald ripening is the dominating mechanism of NPs growth under the low X-ray flux. Especially that even at high flux the mean size of NPs didn't change significantly.

Nevertheless, there is a contradiction in 111 and 220 peaks position changes: 111 peak slowly moves to the high angles, meanwhile 220 peak is shifted to the left-hand side. The simple concepts of accumulation or diffusion of vacancies (not necessarily causing twinning) assume a uniform change of the lattice constant. Consequently, according to this assumption, the changes of 111 and 220 peaks positions should be alike, but they are not. Probably, the opposite change of 111 and 220 peaks positions is a complex effect of all the phenomena described above: accumulation of vacancies followed by ordering/release of vacancies, depletion of small clusters, Ostwald ripening and coalescence.

It is interesting to note that after the initial 25 min evolution the 200 peak position remains almost the same. If we assume that the position of this peak is sensitive to the elastic strains, then this means that the NPs have reached their local minimum energy state. Assuming that the high intensity X-ray beam leads to better ordering, the above interpretation is consistent, and a sort of template growth determines a further increase in the NP size. This process can be characterized by the relatively slow building up of the cluster atom by atom, which provides better ordering than the coalescence. Therefore, the number of domains would increase slowly, resulting in a less strained structure. One way the template growth can occur is through Ostwald ripening. This observation can be used as an additional argument in favor of the assumption that the dominant mechanism of NPs growth exposed to the X-rays is Ostwald ripening.

It seems difficult to distinguish between coalescence and Ostwald ripening by using only diffraction techniques. Also, there is no well-developed theory describing the exact effect of radiation damage on NPs. However, the exact mechanism of nanoparticles growth is not the subject of the current research. The most important aspects are the experimental observations of fingerprints of vacancies and twinning, which are consistent with the proposed theory.

Undoubtedly, the concept of twinning induced by vacancies requires more direct experimental observations and better substantiation. Nevertheless, the measurements and observations described above allow us to conclude that vacancies can play an important role in twinning, and the vacancy induced twinning concept deserves further development.

3.3 Phase segregation and separation in bimetallic NPs

The current understanding of segregation in bimetallic NPs was gained by three different approaches. Computational modeling predicts that small nanoparticles tend to form nanoalloys [71], with increasing temperature more likely the formation of a core-shell structure [138]. TEM observations provide contradictory results demonstrating that surface segregation can lead to the formation of Janus [139] or core-shell structures [140]. XRD measurements indicate the formation of core-shell structure as the most probable process [41]. Meanwhile, high-energy X-ray diffraction experiments combined with atomic radial distribution functions analysis [73] indicate that the alloyed form is the most stable one (for nanoparticles smaller than 10 nm).

Nevertheless, these approaches have several limitations: a) computational models are relatively small and do not consider a size dependence of the phase diagram; b) experimental observations were performed ex-situ, which limits the observation of mass transport phenomena; c) elementally steps of segregation processes are not well known, and existing studies do not provide any deep insight.

To overcome these problems, we based our research on a combination of in-situ + ex-situ XRD techniques complemented by computational modeling. The latter allowed us to distinguish between alloyed, core-shell, and Janus structures in various XRD patterns. On varying conditions of experiments, different diffusion mechanisms can be triggered separately. Understanding of mass transport phenomena strongly depends on the bimetallic sample's exact structure. To substantiate our interpretations, we intensively used TEM EDX map analysis.

3.3.1 Alloyed, Core-shell, and Janus models

Prior to in-situ + ex-situ XRD measurements, a series of computational simulations was performed to explore how XRD patterns change depending on NPs structure and morphology (Figure 42). The shown models were constructed with two assumptions, which limit the direct applicability of these simulations.

The first assumption concerns the NPs morphology: only one and five domain models were considered (Figure 42), while multiple random twinning was not taken into account. This aspect becomes especially important for fitting experimental patterns with the simulated ones. Twinning creates new interatomic distances and changes the ratio of peak intensities. As a result, this phenomenon may lead to misinterpretation of PDF [73] and XRD patterns.

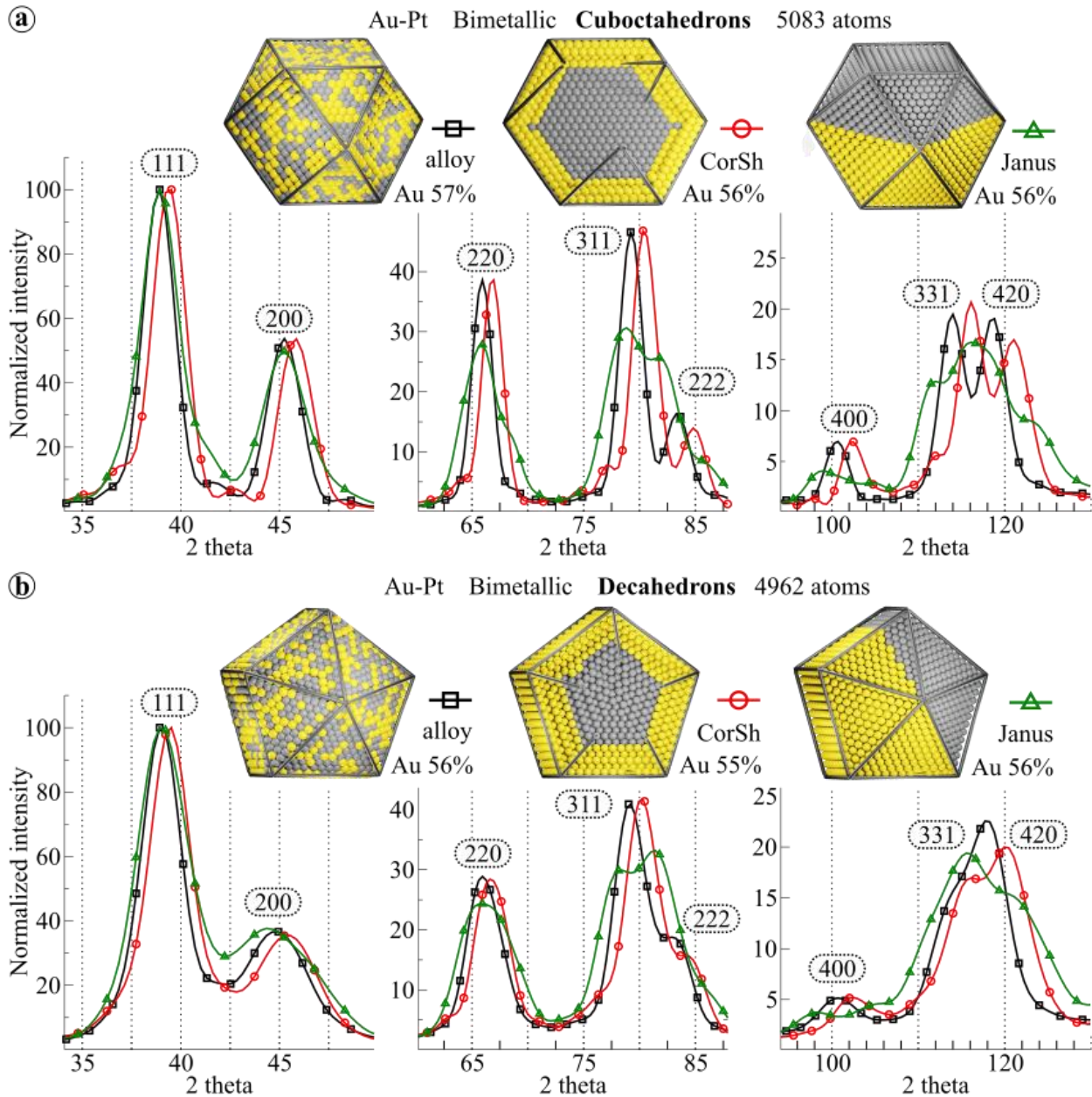


Figure 42 Simulated XRD patterns of relaxed bimetallic nanoparticles. a) AuPt NPs of cuboctahedron shape consisting of 5083 atoms; b) AuPt NPs have the decahedron shape ($m=13$, $n=9$, $p=1$) consisting of 4962 atoms. All patterns were normalized by equalizing the height of 111 peaks. The volume analysis of particles shows that all CUB and DEC morphologies have a size of ~ 5.1 nm. “CorSh” - is a short name for the core-shell structure.

The second assumption concerns composition of Au-rich and Pt-rich parts (lobes) in Janus and Core-Shell particles. The models shown consist of pure gold (Au-rich part) and pure platinum (Pt-rich). In reality, as was demonstrated by Braidy [139] and confirmed by our TEM EDX map analysis, the pure lobes with 100% concentration of one of the metals don't exist. If the core-shell

or Janus structures originate from the alloyed structures, their lobes would be composed of a mixture of metals. In other words, the Au-rich phase will contain some amount of platinum, while the Pt-rich phase will contain gold. The border between these phases is a gradient of concentrations rather than a straight/sharp plane.

Nevertheless, these simplified models illustrate the principal applicability of the XRD technique to detect structural evolution in bimetallic NPs. First, the 111 peak cannot be used as an indicator of segregation [41]! Even for a 5.1 nm CUB Janus particle (with pure Au and Pt lobes), the 111 peak shows no asymmetry. The barely noticeable asymmetry of 111 peak (in the case of CUB Janus NPs) appears when the cluster size exceeds 6.6 nm (10179 atoms). However, in the real samples, considering the above assumptions (morphology + lobes composition), the 111 asymmetry can hardly be noticeable even for 10 nm NPs.

Comparing the AuPt alloy and the core-shell models XRD patterns (Figure 42), only the change of peak positions is visible, while the overall shape remains the same. In the case of core (Pt) – shell (Au) structures, all peak positions are close to pure Pt peak positions (Figure 43 a). It happens because of two reasons. First, the Au shell has a specific shape – a 2-3 atoms thick layer wrapping the Pt core. Therefore, the diffraction pattern of the gold shell will be rather broad and irregular. Secondly, Figure 43 shows that although the Au shell only consists of gold, its diffraction peak positions are closer to the pure Pt peaks. It means that the gold shell is strongly affected and adjusting to the core's properties. It is possible because shell atoms are more mobile than core atoms. Meantime, less mobile core atoms are also affected. The platinum core's peak positions differ from the corresponding pure platinum. However, the core atoms are less strained than the shell atoms.

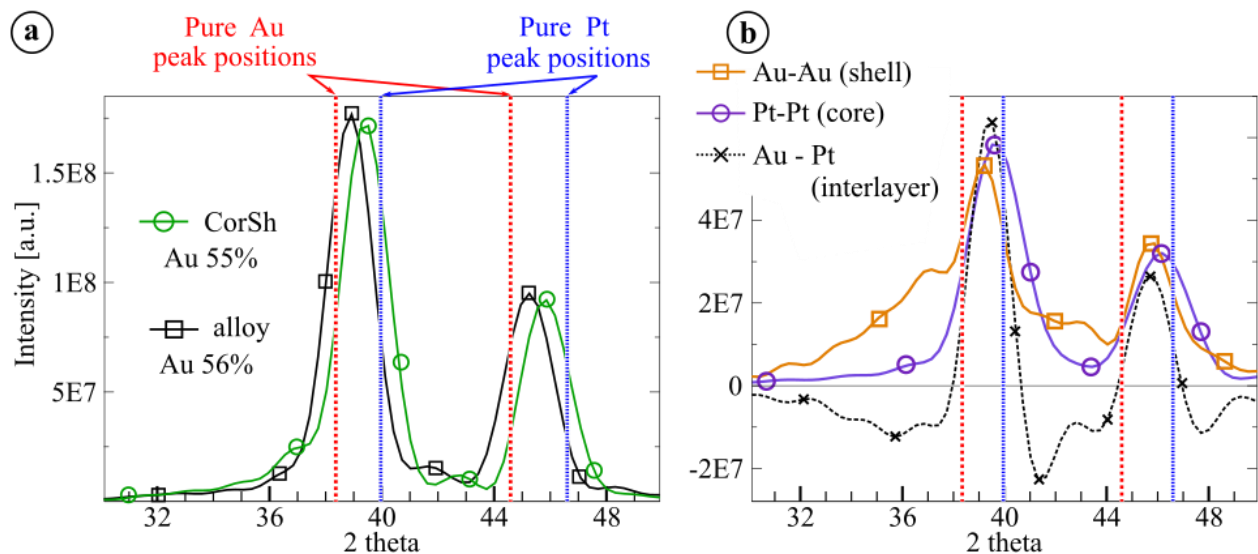


Figure 43 Illustration of a structure composition effect on a diffraction pattern: a) Simulated XRD patterns of the relaxed bimetallic cuboctahedron clusters consist of 5083 atoms; b) Constituents of the CUB core-shell diffraction patterns: contribution from the Au-Au interaction (shell); Pt-Pt interaction (core) and Au-Pt interaction (interlayer). Peak positions of the pure Au and Pt are given for the relaxed CUB models of 2057 atoms.

The same trend can be observed for a reversed structure: Au core - Pt shell clusters. The conclusion is the following: the core composition determines the resulting properties of the XRD pattern of the whole core-shell structure. This trend is probably a general rule typical for most FCC metals and was evidenced experimentally on example of PdAg nanoalloy [82].

Transition from alloy to core-shell can be observed as a uniform shift of all the peaks. Meanwhile, the same approach cannot be applied to detect alloy to Janus transition. A simplified Janus structure model consists of three parts: pure Au, pure Pt, and the phase boundary, which causes appearance of elastic strains in pure lobes. Therefore, for a small cluster, the peak widths of pure lobes patterns are wide and broadened due to elastic strains (and twinning, in the case of multiply twinned models). As a result, these peaks strongly overlap at low diffraction angles, and their positions are close to the peak positions of the alloy model pattern.

Nevertheless, at high diffraction angles, it's already possible to differentiate contributions from different lobes. Therefore, to confirm the appearance of the Janus structure, we propose to monitor the following pairs of peaks: 311 and 222; 331 and 420. Since the Janus lobes have lattice constants similar to that of the pure elements, the corresponding diffraction pattern of a Janus NP will be similar to a sum of patterns of pure components. As a result, one may see that some fractions of the 311 and 331 peaks of the Janus structure are shifted to the left-hand side, compared to the same peaks of the alloy. These shifted fractions correspond to the pure gold lobe, so their positions get closer to that of the pure Au. At the same time 222 and 420 peaks are moved to the right-hand side in comparison to the alloy peaks. The reason is that the contribution of the platinum-rich lobe determines these peak positions.

It is important to note that the described above features (Figure 42) are deduced only from simplified models. In the real samples, the analysis of absolute peak positions is complicated, and diffraction pattern profiles can differ from simulations. Therefore, the analysis of a single XRD pattern scan is a complex task. However, in case of a series of measurements, when there is evolution of NPs morphologies and structures, one can observe a relative change of the XRD patterns. In this scenario, these relative changes can be compared with the predictions from Figure 42, what eventually may allow description of the real state of the sample.

3.3.2 Measurement strategy

For the experimental studies of segregation in the Au-Pt bimetallic nanoparticles, two types of nanoparticles were synthesized: Au₅₅-Pt₄₅@SiO₂ (chapter 2.1.3) and Au₅₅-Pt₄₅@C (chapter 2.1.5). Both as-synthesized samples had structure of alloy. The samples were heated in the stand-alone ex-situ heating setup (Figure 11) or in the in-situ chamber (Figure 12). The preliminary tests revealed that SiO₂-captured NPs are more thermally stable; therefore, they were analyzed more meticulously than carbon-stabilized particles.

Another aspect of these measurements is the use of different gas atmospheres: He and CO. Helium is an inert gas that doesn't form any strong interactions with Au or Pt. Therefore, in He atmosphere, all processes inside NPs will be controlled by thermodynamics. Meantime, CO molecules can be

strongly chemisorbed by Pt atoms. Therefore, in a carbon oxide atmosphere, phase segregation processes will be strongly affected by strong chemisorption.

These differences may allow subtle manipulations of bimetallic NPs structures. Using strong chemisorption interaction between Pt and CO, one may invert the equilibrium core (Pt) – shell (Au) structure. If temperature of the system is high enough, it leads to active mass transfer phenomenon inside the bulk of NPs. In the presence of carbon oxide, CO molecules have a chance to contact Pt atoms and keep them at the surface. Therefore, the shell composition will no longer be enriched with gold but with platinum. The kinetic aspects of such diffusion against the concentration gradient are poorly explored, which makes this approach especially attractive.

3.3.3 Au₅₅Pt₄₅@C

The first sample that was considered is Au_{54.9}Pt_{45.1} nanoalloy stabilized by the octadecylamine (ODA) and supported on the Vulcan XC 72. The metal content ratio with respect to the total mass of the sample is 20.2% (from the synthesis recipe). According to the original recipes [41, 72], the synthesis of nanoparticles should be followed by calcination protocol to remove the organic shell in the flow of a 20% O₂/N₂ gas mixture. Therefore, at the beginning of the in-situ experiments, NPs were exposed to this mixture of gases. After the calcination, the gas atmosphere was changed to helium to avoid any further oxidation reactions, which can strongly affect the experiment.

The initial mean size of the nanoparticle estimated by TEM is 4.6 nm (Figure 44). The same result can be obtained from the MDXRD method by measuring the integral breadth of 220 peak (instead of FWHM) ~ 4.4 nm. Comparison of the TEM volume-weighted size distribution (mean size is ~ 5.1 nm) and MDXRD (FWHM) of 220 peak (mean size ~5.5 nm) also shows similar results. These similarities suggest applicability of the multidomain method to the analyzed samples at their initial state.

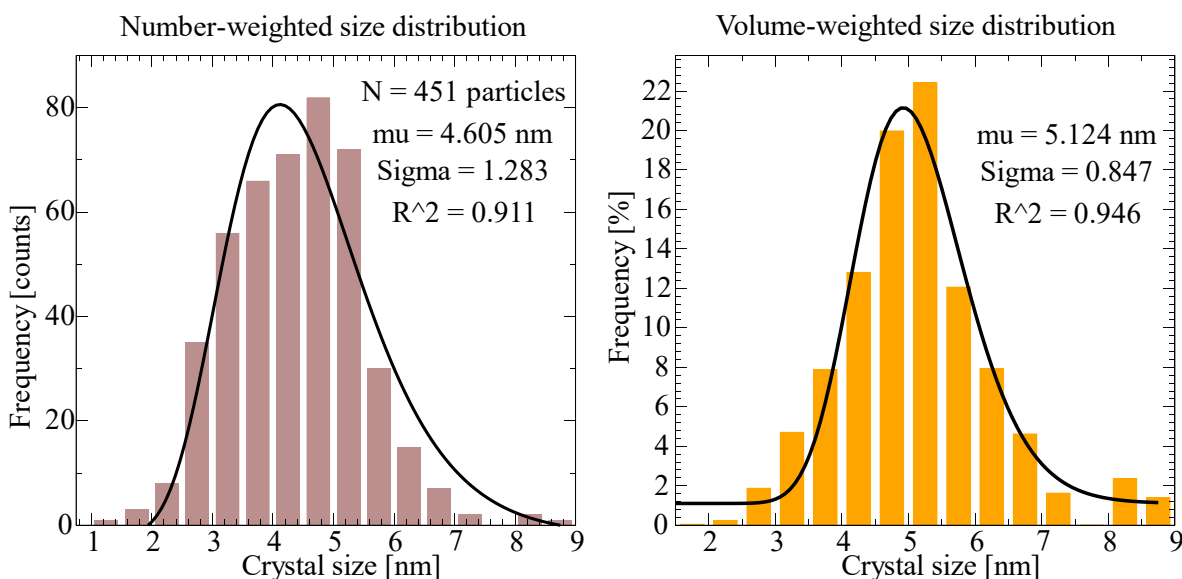


Figure 44 TEM analysis of particles size distribution of as-synthesized Au₅₅Pt₄₅@C NPs

The ratio of metals was analyzed by two techniques: XRF and XRD. According to XRF, the ratio between Au and Pt was 54.9 to 45.1. Applying Vegard's law to 220 peak, the ratio is 55.6 (Au) to 44.4 (Pt), what indicates that the synthesized nanoparticles have structure of alloy. After the in-situ experiments, the specimen was additionally analyzed by XRF to confirm the absence of contamination. After 361 hours of in-situ measurements, no sample contaminants were found.

3.3.3.1 In-situ XRD

The detailed scheme of the experiment is shown in Figure 45. The XRD pattern was measured from 20 to 90 degrees (2 theta) in continuous mode with rate of 0.02° per second. Therefore, it takes about one hour to collect one XRD pattern. This defines the time scale of the in-situ experiment stages (Figure 45) discussed versus the number of scan.

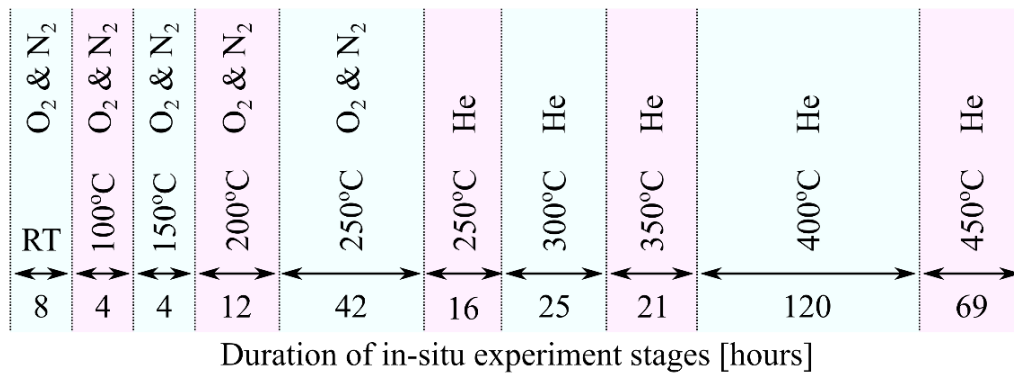


Figure 45 Scheme of the in-situ XRD experiment with Au₅₅Pt₄₅@C samples

Figure 46 illustrates the summary of the entire in-situ measurement. All data shown in this figure were corrected for the specimen displacement (Chapter 2.2.5.2) and thermal expansion of Au-rich and Pt-rich phases (Chapter 2.2.5.3). Since the analyzed sample consists of two metals, all observed lattice constants will always be in the range between pure gold and platinum. Therefore, the temperature evolution of lattice parameters can be considered relative to the parameters of pure metals. Instead of absolute values, Figure 46 **a** and **c** show the gold mass fraction in the sample (where 1 is 100% Au). The ratio of metals was calculated using Vegard's law applied to the 220 peak. This peak was chosen because it has no strong overlap with other peaks, what simplifies its analysis compared to other peaks. Summary of the 220 peak evolution is also shown in Figure 46 **a** and **b**.

In general, Au₅₅Pt₄₅@C nanoparticles evolution can be divided into distinct parts. At the first stage (< 250°C), there was no clear phase separation leading to split of diffraction peaks. During the heating, all peaks were uniformly shifted and preserved their initial shape. As can be seen from Figure 46 **a**, the lattice constant was decreasing and approaching Pt l.c. value. This trend was observed not only for 220, but also for other peaks. Since the actual ratio of metals didn't change, these shifts can only be caused by change in the internal structure.

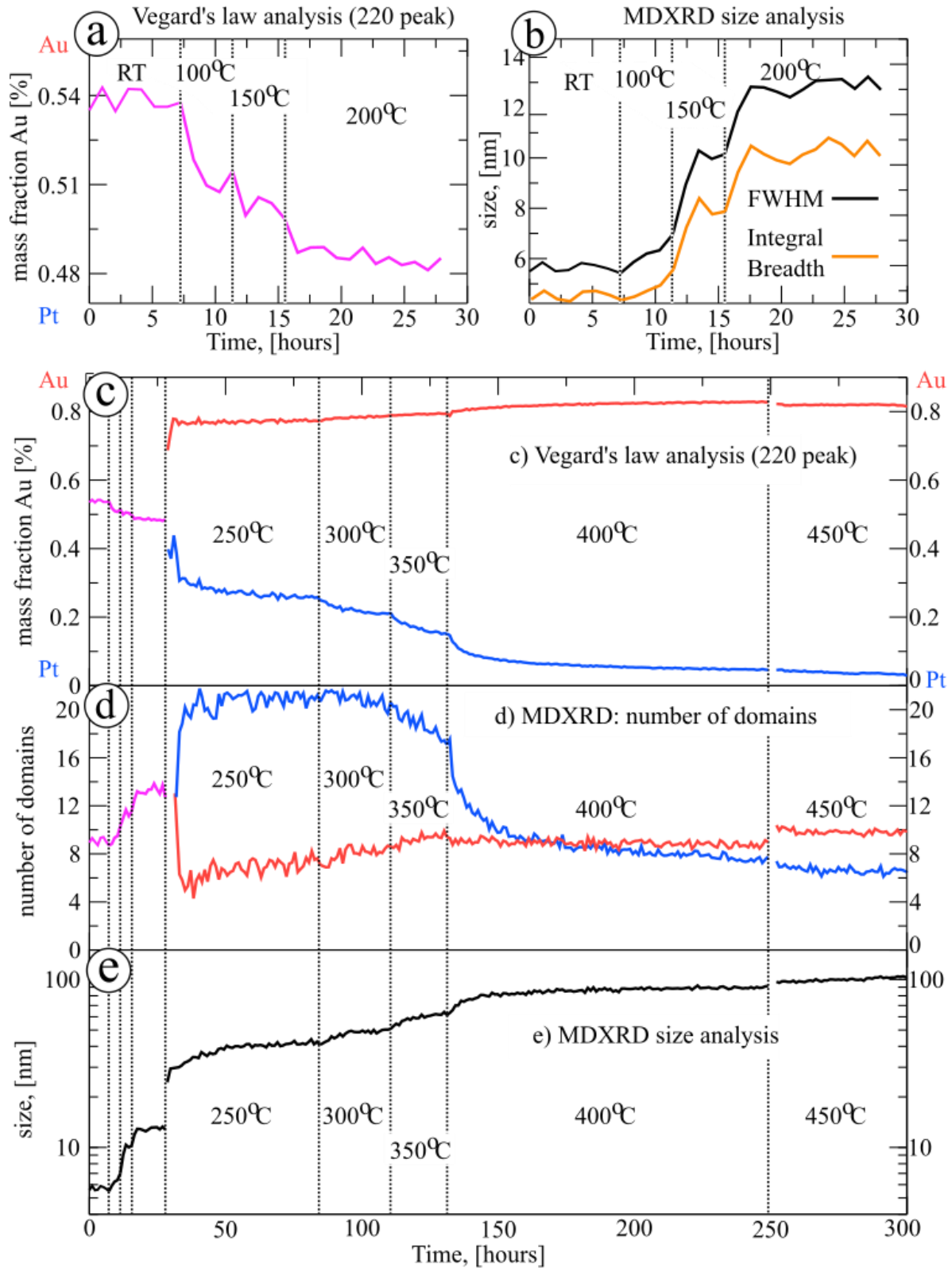


Figure 46 Summary of in-situ experiment with $\text{Au}_{55}\text{Pt}_{45}@C$ sample

According to Figure 42, the right-hand side shift (in terms of 2 theta degrees) can be caused by the transition from the alloy to the platinum core and gold shell structure. In this case, with such a transformation, the overall profile of the diffraction pattern doesn't change. Some subtle changes can only be found at high diffraction angles for 331 and 420 peaks. Unfortunately, the considered in-situ measurements did not cover this region.

The further heating of the sample led to growth of the mean particle size (Figure 46 b). However, the difference between MDXRD size analysis with FWHM and with integral breadth remains similar. Also the "shape" parameter of the Person 7 function didn't evolve so it is likely that size distribution broadening caused by heating was not too intense. Therefore, MDXRD is still applicable for this stage, although with less accuracy.

Combining Figure 46 a and b, one can see the active structure evolution happened during the initial size growth. Meantime, at 200°C when the mean size was about ~10nm (number-weighted one), the phase segregation rate became slower.

The (principal) second stage of the in-situ measurement occurred starting from 250°C. The main reason for this metamorphosis is thermal decomposition of the stabilizing agent – ODA. Once an oxidation environment is supplied and the temperature exceeds 200°C, the stabilizing ODA can be easily destroyed [141]. Therefore, after ODA removal, nanoparticles intensively started to grow, what strongly affected the NPs size distribution. At this stage, MDXRD is becoming less accurate. However, it can be used to evaluate magnitude of the mean size evolution (Figure 46 e). During the first few hours of heating at 250°C the mean NPs size has changed from ~13 nm to ~30 nm (volume-weighted sizes).

Besides rapid size changes, the NPs structure evidently evolved from a core-shell-like structure to a Janus-like structure (Figure 42, Figure 47). Unfortunately, there is no way to track down the kinetic aspects of this transformation. First of all, the size evolution was too quick to build a decent model of this process. Secondly, despite the relatively big NPs size, it is hard to clearly distinguish between gold-rich and platinum-rich phases. During the first few hours of heating, their diffraction peaks strongly overlap, making the detailed analysis challenging.

Nevertheless, MDXRD revealed a unique feature of the observed phase separation. The numbers of domains of Au-rich and Pt-rich phases are not equally changing (Figure 46 d). In the case of the Au-rich phase, right after the phase separation, there is a rapid decrease in the mean number of domains. Meantime, the Pt-rich phase demonstrates severe twinning, and the number of domains grew from ~13.3 up to 21! The number of domains started to slowly decrease only when the temperature exceeded 350°C.

It's likely that gold atoms ($T_{\text{melt}} \sim 1064$ °C) are more mobile than platinum ($T_{\text{melt}} \sim 1768$ °C). Therefore, one may assume that the main driving force of phase separation is the movement of gold atoms to the surface of a cluster. In other words, the gold-rich phase was dominantly formed via the migration of gold atoms from a previous Pt-Au mixture state (48% Au and 52% Pt). This can explain why the newly formed Au-rich phase has fewer domains than at the beginning. After Au migration, a significant number of defects were formed inside the Pt-rich phase. Since the platinum atoms are less mobile, they do not have enough energy to relax the defects preserving the same

morphology. It is likely that the accumulation of defects caused intensive twinning, which one can observe as an increase in the number of domains. The described mechanism is similar to the one described in Chapter 3.2: Vacancy driven twinning.

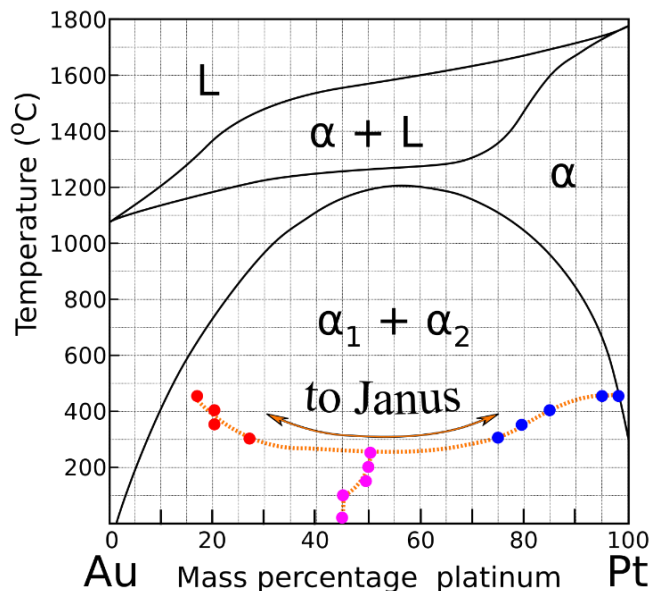


Figure 47 Summary of the 220 peak evolution. Purple points correspond to the initial alloyed state, which during the heating, demonstrates a shift characteristic for the formation of core-shell particles ($T < 250^{\circ}\text{C}$). Red and blue points correspond to the Au-rich and Pt-rich phases, respectively ($T \geq 250^{\circ}\text{C}$). The heating is a continuous process, and NPs states at the beginning and at the end of heating are different. Each point on the graph represents the initial state of the sample at the corresponding temperature. For example, the phase separation happened after the heating at 250°C . To show that the sample was stable up to this point, the only initial single-phase state at 250°C is shown. The final stage of phase separation at 250°C coincides with the initial state at 300°C .

In general, the described above phase separation is similar to the Kirkendall effect. When there is interdiffusion between two phases with different diffusion rates, it leads to the formation of vacancies and voids. However, in case of the considered AuPt particles, there is no interdiffusion but rather a segregation. The most suitable analog of this phenomenon for bulk alloys is spinodal decomposition (SD), in which vacancies play an important role. The phase separation proceeds without activation barrier and on small distances determined by the NPs size.

A literature search showed that there is the concept of SD that fits the experimentally observed phenomena (Figure 46 d) [142]. According to Kharchenko et al., if the defect formation rate is high enough, then vacancies can accumulate in the phase with a lower diffusion coefficient. Their numerical simulations support the notion of intensive twinning of the Pt-rich phase driven by vacancies.

It's important to note that the initial MDXRD equation 31, which was used to calculate Figure 46 b, d, e graphs, is not calibrated for non-RT measurements. Any change in temperature affects the Debye-Waller factor, which is size dependent. This means that the calibration graph (Figure

21) is less accurate, and some coefficients (β and slope value) in Equation 32 must be modified. To do this, one has to repeat the procedure that was described in Chapter 3.1: do molecular dynamics simulation for different size DEC; disassemble them into domains; analyze corresponding XRD patterns; plot dependencies, and, finally, modify equation 31. Moreover, it should be done for each temperature separately.

The modification of the initial MDXRD equation is a very laborious task. So far, it will be used in its current (RT) form. Even though absolute values obtained using MDXRD might differ from the real ones, the trends are trustful as, for example, the rapid decrease of the number of domains in the Pt-rich phase at 400°C. The rise of the DW factor should directly lead to the apparent growth of twinning, what is not the case. The same trend can be found in the Au-rich phase. Despite the rise of temperature from 200°C to 250°C, the average number of domains is decreasing. Although the multidomain equations used were calibrated for the RT, they can be applied to in-situ measurements to reveal the trends of internal morphology evolutions.

3.3.3.2 TEM EDX mapping

After the in-situ measurement, the structure of the nanoparticles was examined using TEM with energy dispersive X-ray (EDX) elemental analysis. As can be seen from Figure 48, after the high-temperature treatment (450°C), most of the particles demonstrate phase separation of Au-rich and Pt-rich phases. Only very small particles (below ~10 nm) demonstrate a structure similar to a core-shell. No alloyed particles were found. These observations confirm our in-situ XRD-based assumption on the formation of Janus-like NPs.

Unfortunately, due to the high loading of the metals (~20 wt.%), once the stabilizing ODA agent was removed, an intensive coalescence occurred. NPs started to grow, forming non-spherical particle aggregates. Therefore, it's difficult to perform a convenient size distribution analysis for this sample. Additionally, one may notice that very big particles (left-hand side figure) cannot be called "Janus", because of the non-uniform distribution of phases.

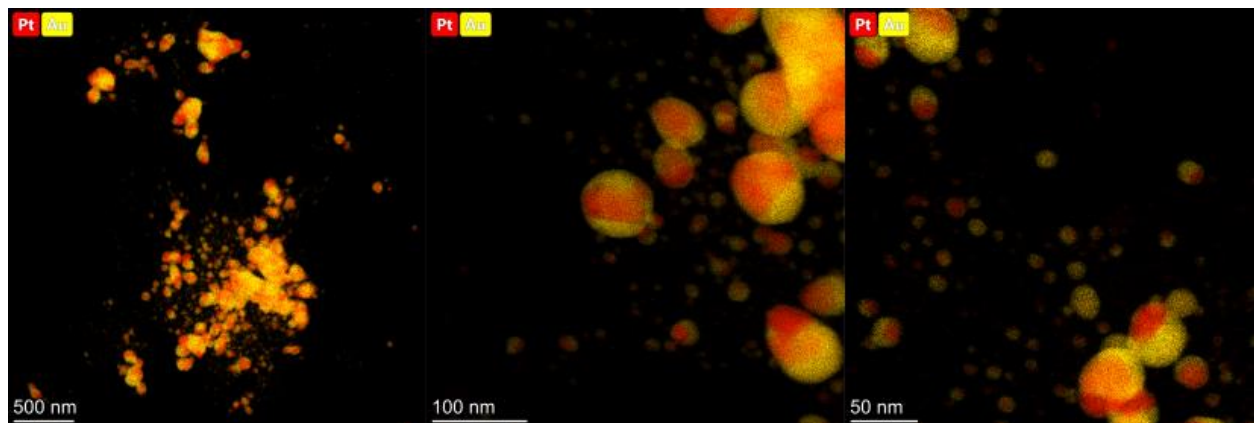


Figure 48 TEM EDX mapping of Au₅₅Pt₄₅@C sample after the in-situ XRD measurement

3.3.4 Au₅₅Pt₄₄@SiO₂

The second sample that was studied is Au_{55.2}Pt_{44.8}@SiO₂ stabilized by PVP and supported on SiO₂. The metal content ratio with respect to the total mass of the sample is 1.4% (according to the synthesis recipe).

The ratio of metals was analyzed with two techniques: XRF and XRD. According to XRF, the ratio between Au and Pt was 55.2 to 44.8. Applying Vegard's law to 220 peak, the ratio is 56 (Au) to 44 (Pt), what indicates that the synthesized nanoparticles have alloy structure.

The initial mean size of nanoparticles estimated by TEM was 3.6 nm (Figure 49). A similar result can be obtained using the MDXRD method by taking the integral breadth of 220 peak (instead of FWHM) ~ 3.4 nm. Comparison of the TEM volume-weighted size distribution (mean size is ~ 4.2 nm) and MDXRD (FWHM) of 220 peak (mean size ~4.3 nm) also shows similar results. These similarities indicate the applicability of the multidomain approach to the analyzed sample at its initial state.

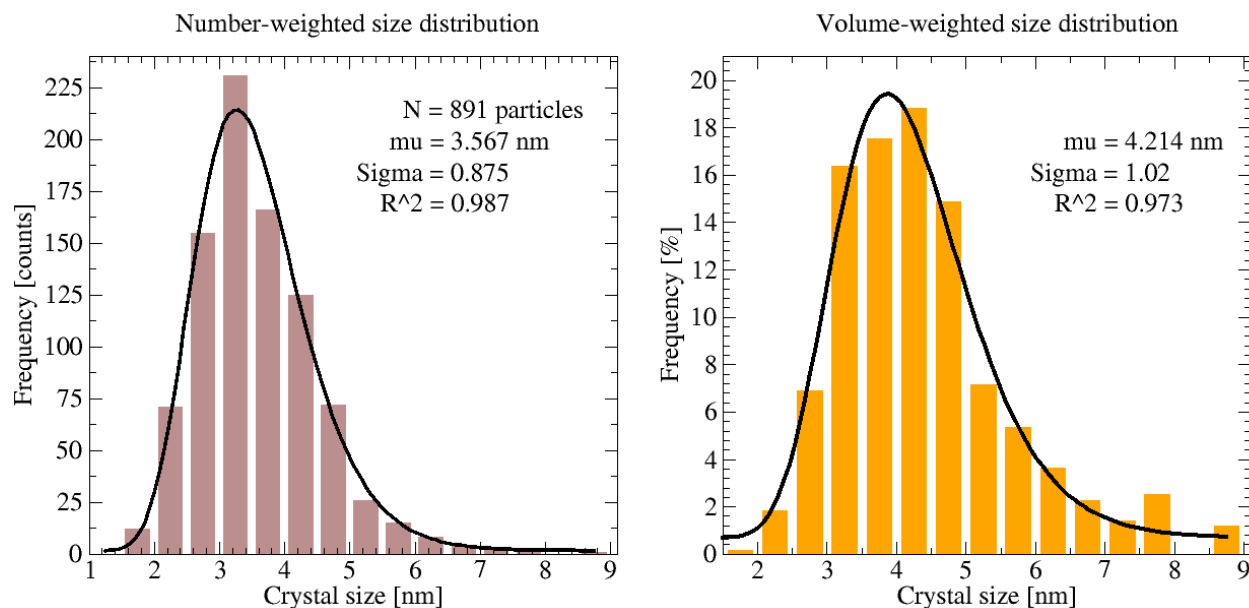


Figure 49 TEM analysis of particles size distribution of as-synthesized Au₅₅Pt₄₅@SiO₂ NPs

3.3.4.1 Ex-situ XRD

The detailed scheme of the experiment is shown in Figure 50 a. Approximately 1g of the as-synthesized sample was placed in the ex-situ reactor (Figure 11). Then the system was heated up according to the scheme given below. At the end of each stage, the whole setup was cooled down to RT, and a small fraction of the sample (~40-50 mg) was collected for further analysis. After the sample collection, prior to heating, the system was purged for 15-20 min with gas that was planned to be used.

The XRD pattern was measured from 15 to 140 degree (2 theta) in continuous mode with rate of 0.02° per second. XRD technique is sensitive to the parameters of the analyzed sample packed bed; therefore, a few more aspects were taken into account to improve the quality of the final XRD patterns. To keep the same thickness of the bed, the same sample holder was used each time. To maintain the bed density approximately constant, the mass of the sample taken for the XRD analysis was strictly controlled. All samples were measured after cooling down to RT, so all diffraction patterns were analyzed without corrections.

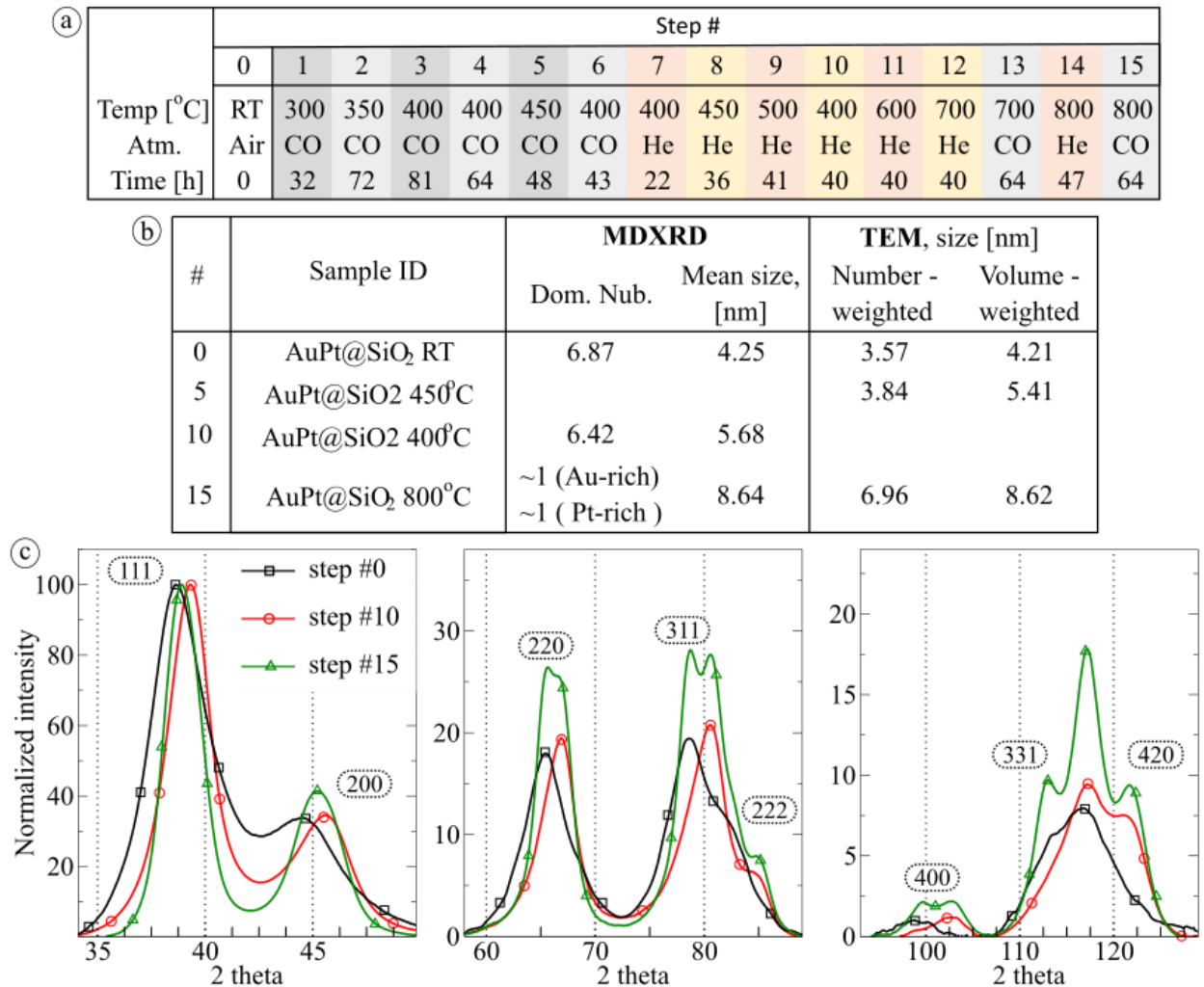


Figure 50 a) Scheme of the ex-situ experiment with Au₅₅Pt₄₅@SiO₂ samples; b) results of MDXRD and TEM size distribution analysis of samples at key stages of the ex-situ measurement; c) XRD patterns of AuPt@SiO₂ samples at key stages of the ex-situ measurement. Unfortunately, there is no diffraction pattern for step #5 and no TEM data for step #10. However, XRD analysis shows that after step #5, there were no significant changes in the sample structure until step#11. Therefore, the samples at stages #5 and #10 can be considered interchangeable.

During the heating, the synthesized AuPt@SiO₂ samples were very stable, and quick sintering of NPs did not happen. According to the TEM analysis, even after the heating at 800°C, the mean volume-weighted size increased only up to 8.6 nm (Figure 50 b).

The whole evolution process of the AuPt@SiO₂ sample can be divided into two main stages: from step # 0 to #10 and from step #10 to #15 (Figure 50 c). During the first stage, starting from 300°C, all diffraction peaks were uniformly moving towards high angles. According to the computational predictions (Figure 42), this feature indicates the transformation of alloyed particles into the core (Pt) – shell (Au) structure. This conclusion was confirmed by TEM EDX analysis. However, not only core-shell particles were found, but also not transformed alloyed ones. I.e., the analyzed sample (step #5, 450°C) is a mixture of the core-shell and the alloyed particles. Unfortunately, these alloyed and core-shell particles are too small, and their diffraction peaks strongly overlap. Therefore, it's difficult to calculate the ratio between these structures using the XRD method.

During the second stage (#10 - #15), starting from 600°C, the phase separation can already be noticed (220, 311, and 400 peaks). The small angle profile of the splitted peaks were moving to the left-hand side, while the higher angle profile to the right-hand side. This pattern is typical for the phase separation, which means that with rising of temperature (and the mean NPs size!), core-shell structures transformed into the Janus particles. This conclusion was confirmed by the TEM EDX analysis. However, not only Janus particles were found, but also not transformed core-shell clusters (and very few alloyed NPs). I.e., the analyzed sample (step #15, 800°C) is a mixture of Janus and core-shell particles (Figure 51). Unfortunately, even these particles are too small, and their 111 diffraction peaks strongly overlap. Therefore, it's difficult to calculate the ratio between these structures using the XRD method.

Nevertheless, even if two structures are present, one may notice how the height of the 220 peak of the last sample (#15) differs from that of other samples. According to the multidomain approach, the H_{220}/H_{111} ratio is an indicator of the degree of twinning. That means that the last sample has significantly smaller concentration of domains than the other samples. Making the assumption that the sample at stage #15 consists of only Janus particles, both Au-rich and Pt-rich phases have approximately 1 domain! This means that once coalescence is suppressed, with the rise of temperature, the mean number of domains decreases.

One may notice that further TEM EDX indicated the presence of core-shell and Janus particles; meanwhile, for the MDXRD analysis, only the Janus model was considered. Unfortunately, there is no way to differentiate the contributions of these structures, and only one model can be considered. The Janus particles model provided a size analysis result, which is in good agreement with TEM data. On that basis, the number of domain analyses can be considered valid.

3.3.4.2 TEM EDX mapping

Two samples were analyzed with TEM EDX analysis: samples at stages #5 (450°C) and #15 (800°C). Both samples revealed similar trends. The analysis of the first sample (stage #5) showed that it consists of a mixture of the alloyed and the core-shell particles. Meanwhile, the second one (stage #15) consists of the quasi-Janus (q-Janus) and the core-shell particles (with a small fraction

of the alloyed NPs). The best example representing these features is shown in Figure 51 a - experimentally observed EDX map analysis of the AuPt@SiO₂ NPs after the treatment at 800°C in CO (stage #15). This figure shows that different bimetallic structures may coexist at the same time despite of the high-temperature treatment! This means that an appearance of one or another bimetallic structure is a complex phenomenon that depends not only on the supply of external energy. If there were a common energetically stable state for all NPs, then all observed particles would have the same structure. This means that the minimal energy state depends on something that is individual for each particle and differs the given particle from others.

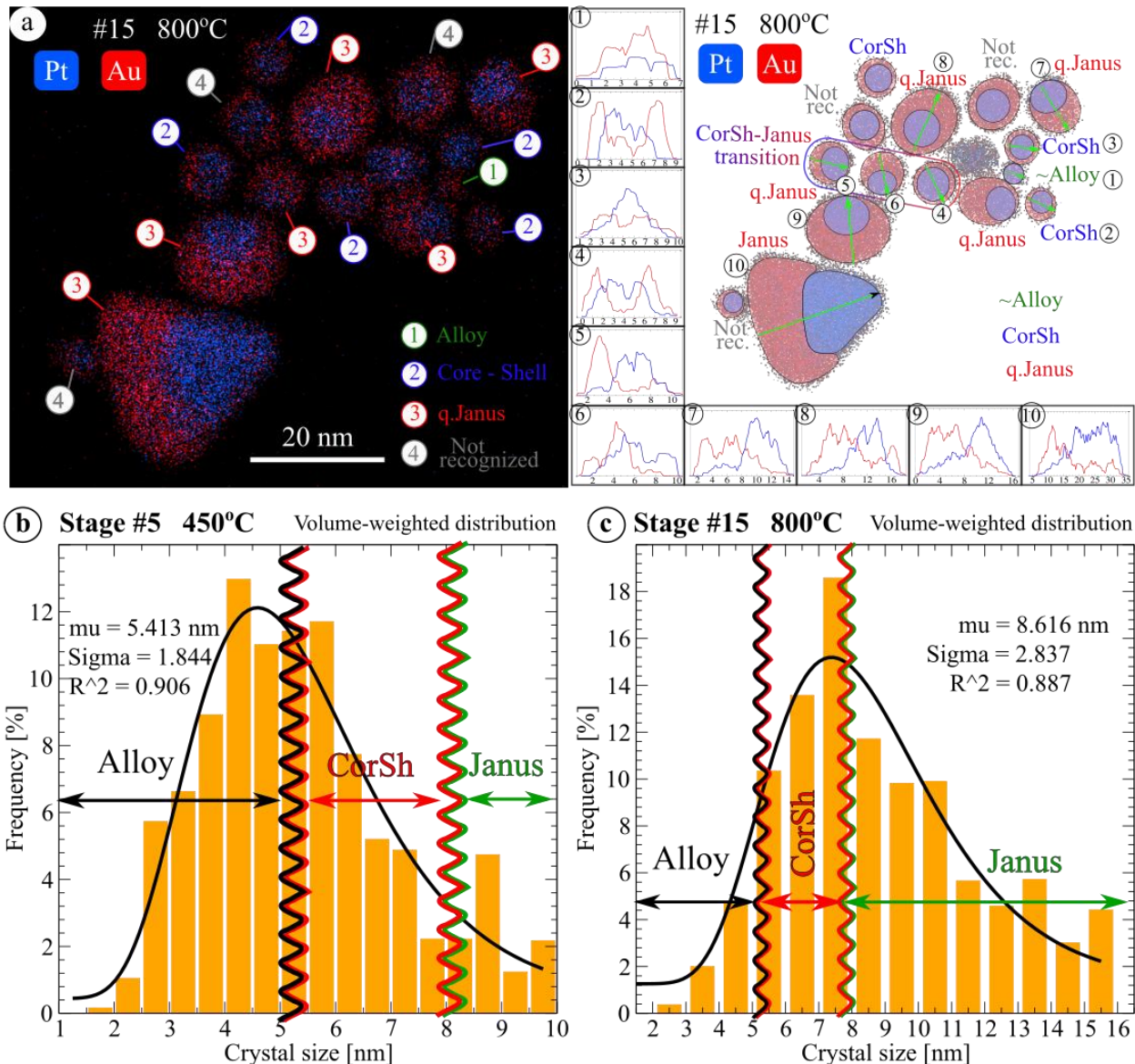


Figure 51 a) TEM EDX mapping analysis of the AuPt@SiO₂ sample after heating at 800°C in CO (stage 15); the right-hand side figure shows the cross-section analysis of the numbered particles (from 1 to 10) along the green arrows; b) TEM analysis of particle size distribution (recalculated to the volume-weighted one) after the stage #5; c) TEM analysis of particle size distribution (recalculated to the volume-weighted one) after the stage #15

The right-hand side of Figure 51 **a** shows the simplified version of the left-hand side figure. One may notice that the big particles (particles number 6 – 9) are quasi-Janus particles. Once the NPs size becomes smaller than ~8.5 nm (diameter of particle # 6), only core-shell particles can be seen (4-2). A very small particle with diameter of 4.3 nm resembles the alloyed structure. On the basis of this observation, one may conclude about the size dependency of the phase separation and segregation. In other words, the appearance of quasi-Janus, core-shell, or alloyed structure is not only temperature dependent but also depends on the size of a particle.

This conclusion means that each structure has its own size range in which it can exist. In order to gather more evidence to support it and to determine the ranges, a detailed analysis of TEM EDX maps was performed. In total, 9 EDX maps (five and four figures of stages #15 and #5, respectively) were analyzed for the smallest core-shell and quasi-Janus NPs. The smallest core-shell structure has a diameter of 5.6 nm, and the smallest quasi-Janus - 8.5 nm (Figure 51 **a**) NP number 6. From the right-hand side of Figure 51 **a**, one can see how the transformation from the core-shell to the quasi-Janus particle may occur. Particle 4, with a size of 7.6 nm has a core-shell structure; while its neighboring particle 5, with a size of 8.3 nm, already looks more like Janus (see cross-section). The even more decent quasi-Janus structure can be seen for particle 6, which has a size of 8.5 nm. Despite similar environmental conditions, these three particles have different structures.

The structural transition appears as a continuous process without sharp steps. Even within quasi-Janus particles, the concentrations of metals inside Au-rich and Pt-rich phases might differ. It seems that the phase separation and segregation have no strictly defined size for transitions. There are rather size ranges at which these transformations start to occur. The approximate size ranges at which different structures exist (Figure 51 **b** and **c**) are shown by the wavy lines. These borders are not strict, and their width is not statistically meaningful.

Still, it is difficult to distinguish between core-shell and quasi-Janus particles at such small NPs size. To draw the conclusion about particle structure from the TEM EDX map analysis, every figure needs to be separated into several monochromic figures. Then, in some cases, comparison between these figures allows for determining the orientation of Au and Pt-rich phases with respect to each other. For example, if the Pt-rich phase is not surrounded by Au-rich phase and is located at the side of the cluster, then the analyzed particles have a quasi-Janus structure (Figure 51 **a**) NP number 8.

3.3.5 Au-Pt segregation concept

Besides observations in Figure 51 **a**, there are other pieces of evidence endorsing the idea that phase separation and segregation are size dependent. During the in-situ XRD experiment (with AuPt@C NPs), the structural evolution path was very similar. The only difference is that the core-shell transition was not very well visible because of a rapid NPs size growth. Nevertheless, during the heating at 100°C to 200°C, all diffraction peaks shifted towards high angles (Figure 46 **a**) while phase separation didn't happen. This transition indicates the core-shell particles formation.

The most significant difference between ex-situ (AuPt@SiO₂) and in-situ tests (AuPt@C) is the temperature at which phase separation occurred. In the case of AuPt@SiO₂, it happened at 600°C; meantime, for the AuPt@C sample, it happened at 250°C (Figure 52 a)! Moreover, the analysis of the 220 peak position by Vegard's law shows that in the case of the low-temperature experiment, the phase separation was stronger and faster!

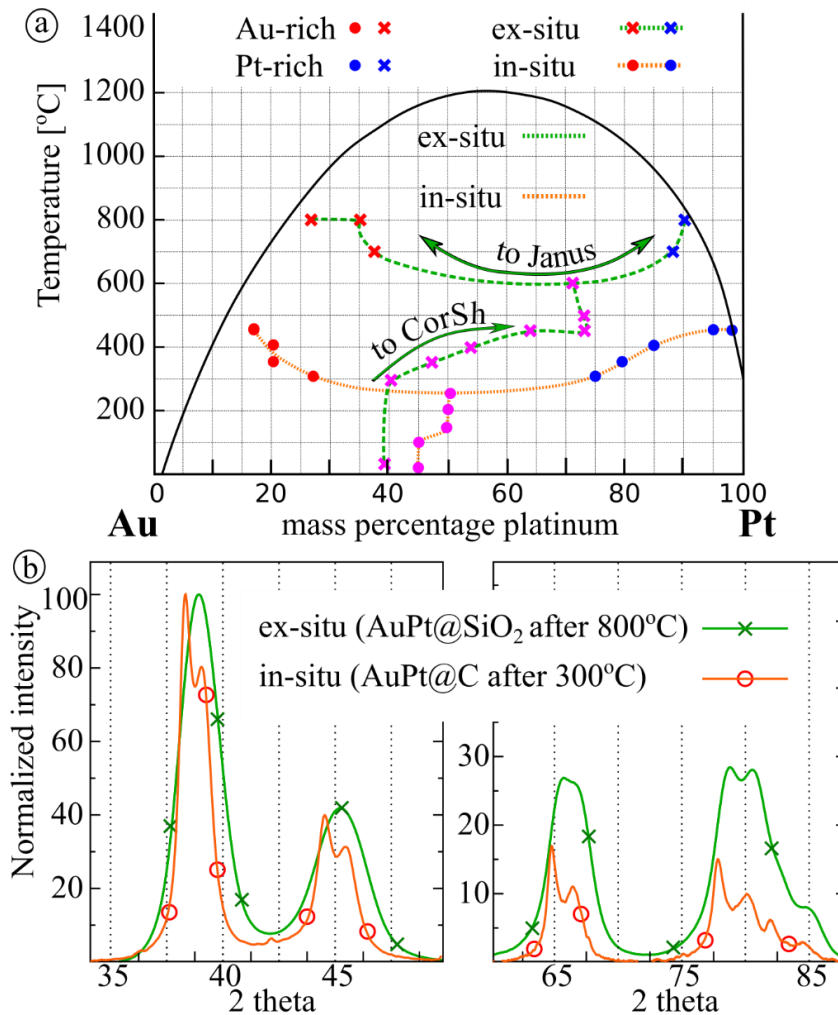


Figure 52 a) Summary of the 220 peak evolution showing the change of metals ratio based on Vegard's law. The heating is a continuous process, and NPs states at the beginning and at the end of heating are different. Each point of the graphics represents the initial state of the sample at the corresponding temperature. b) Comparison of XRD diffraction patterns of the AuPt@SiO₂ sample after the ex-situ measurements at 800°C in CO (stage #15) and AuPt@C sample after the in-situ measurements at 300°C in He (in the middle of the stage ~ 10 hours).

One may find similar phase separation states in both samples. It can be done by analyzing the difference between the peak positions of Pt-rich and Au-rich phases. The strongest phase separation of the ex-situ sample occurred at the very last stage (800°C), meantime a similar state was observed

for the in-situ sample at only 300°C (Figure 52 b). This means that the driving force of segregation was large at significantly smaller temperature! To explain this phenomenon, one needs to add an additional parameter that will influence the phase separations. On the basis of all the arguments described above, the best candidate for this parameter – is the size.

Alternatively, one may argue that the sample supporting materials (ODA and PVP) were treated at different gas atmospheres. The ODA was burned in the O₂ while PVP was decomposing in the flow of CO and HE. As a result, the AuPt@C sample surface (ODA removed) was more mobile, which may provide better vacancy diffusion from the surface to the bulk. Which eventually may promote better and faster diffusion of atoms, leading to stronger phase separation.

This explanation can be valid, but to a less extent than the size dependency. The problem is the following: the idea of the active vacancy formation doesn't explain why AuPt@SiO₂ sample after the treatment at 800°C doesn't reach the same phase separation degree as the sample treated at a lower temperature. Also, this theory doesn't explain the existence of the core-shell particles at 800°C. One may notice that the number of domains at the high temperature is significantly smaller than in the case of the AuPt@C sample. This means that atoms inside the AuPt@SiO₂ sample have enough energy to relax twin planes. Therefore, the internal diffusion rate should be sufficient to provide as strong phase separation as it is possible.

The separate pieces of the described size-dependent segregation are known and well-described. There are a lot of experimental and theoretical works showing that the transition from the alloyed state to the core-shell is energetically favorable. Besides, there are works describing the transition from the core-shell to (quasi-)Janus and indicating its high probability. Moreover, the size dependency of the alloyed and the core-shell particle appearance was theoretically described. However, to the best of our knowledge, these elements have never been considered as one phenomenon.

So far, the theory of size-dependent phase separation and segregation is based on the experimental observations described above. The next step would be to combine these observations with theoretical predictions.

4 Conclusions

For a long time, nanoparticles have been the subject of intensive studies. Despite numerous works describing the importance of morphology on NPs properties, most of the scientific community is underestimating this aspect. One of the main reasons for that is a lack of experimental tools for bulk morphology analysis. So far, only high-resolution TEM allowed twin planes and stacking fault analysis. However, microscopy has drawbacks that make it not applicable as a routine tool and unavailable for many scientists.

The first part of the thesis addresses this issue. Extensive computational simulations showed how twin planes affect X-ray diffraction patterns, leading to the formation of elastic strains. 13 various sizes (3.1 – 9 nm) decahedrons were disassembled into one, two, three, and four domain clusters to demonstrate this phenomenon. Then, a powder XRD pattern was calculated for each model, followed by the analysis of the 220 to 111 diffraction peak height ratio. As a result, it was described how H_{220}/H_{111} ratio depends on the number of domains in the cluster. The method allowing characterization of the NPs morphology based on XRD is called multidomain XRD.

Besides the theoretical development of MDXRD, it was applied to various gold and gold-platinum bimetallic particles. The results of MDXRD were in good agreement with the reference TEM and SAXS techniques. The multidomain analysis allowed monitoring of several types of morphology evolution: a) ordering of NPs structure in the Au@SiO₂ sample; b) growth of the number of domains for the Au@PVP; c) remarkable twinning of Pt-rich phase during phase separation of the AuPt@C sample.

Additionally, the applicability limitations of the multidomain approach were discussed. In the case of broad particle size distribution, MDXRD tends to overestimate the mean size of NPs. In fact, the obtained (overestimated) result will be correct but represents the large-size fraction. This limitation was demonstrated in experiments with ex-situ heating of the Au@SiO₂. For temperatures below 800°C, the particle size distribution was narrow, and there was a good agreement between TEM, SAXS, and MDXRD. Once the temperature exceeded 800°C, intensive particle growth happened, resulting in the divergence of the mean size estimations.

The second part of the thesis focuses on describing a novel mechanism of twinning formation – vacancy driven twinning. It is known that vacancies are present inside nanoparticles. However, only a small concentration of defects has been discussed so far. Extensive computational simulations showed that once the concentration of vacancies exceeds 13.1%, with a high probability it will trigger the stacking faults appearance: the higher the concentration, the higher the degree of twinning.

The vacancy driven twinning is an important step towards understanding twin plane formation. First of all, this method can be used in computational science (unlike other mechanisms). Secondly, as shown in the thesis, such an approach allows to model locally the HCP gold structure! To the best of our knowledge, this is the first time FCC gold was transformed into the HCP phase by regular computational simulations using an energy minimization procedure.

The experimental work on this topic can be divided into observation of vacancies and twinning. Detecting vacancies is a very challenging task as the relevant methods are scarce or missing. Therefore vacancy-related properties were analyzed: size and density. Ex-situ heating (!) of the Au@SiO₂ demonstrated a decrease in mean size with the temperature! So far, only vacancy diffusion to the surface can explain such counterintuitive change. Once mean size and vacancy concentrations decrease, it improves the density (confirmed by SAXS).

Other experiments with the Au@PVP aimed to observe twinning as a result of long-time X-ray exposure. It was found that X-ray exposure led to a decrease of 111 diffraction peak height while mean particle size grew. This phenomenon can only be explained as an accumulation of vacancies. Therefore, it is logical to expect that after a long exposure, the vacancies concentration can exceed the critical level and cause twinning. Unfortunately, for the regular Cu-radiation, there was no twinning detected. However, after synchrotron radiation, the number of domains started to grow.

The last part of the thesis focuses on the phase separation and segregation phenomena in bimetallic AuPt nanoparticles. The AuPt phase diagram assumes the mixing of these metals in wide range, allowing the appearance of different alloyed, core-shell, and Janus particles. To monitor transitions from one state to another, two types of experiments were performed with heating of the samples: in-situ XRD (AuPt@C) and ex-situ (AuPt@SiO₂).

In the case of heating of the AuPt@SiO₂ sample, the growth of nanoparticles was slow. It allowed monitoring of the transition from the initial alloyed structure to the core-shell followed by the (quasi-)Janus structure. TEM EDX analysis showed that at 800°C all three structures may exist simultaneously. Therefore, one may conclude that their size rather than the temperature determines the appearance of one or another structure: alloyed particles are stable below ~5 – 5.5 nm; core-shell structure exists in a range from 5.5 nm to ~ 8 nm, while quasi-Janus appears if their size exceeds 8.4 nm.

The in-situ experiment with the AuPt@C sample confirms the conclusion about the domination of size dependence over the temperature. The AuPt@C heating included removal of the stabilizing ODA agent, making it less thermally stable. Once ODA was removed NPs started to grow quickly, and XRD confirmed the first signs of Janus particles appearance at 250°C. Meanwhile, in the case of ex-situ measurements with the more thermally stable AuPt@SiO₂, first Janus particles were observed at 600°C.

The MDXRD analysis of phase separation (Janus particle formation) of the AuPt@C sample revealed that the morphology evolution of Au-rich and Pt-rich phases are dramatically different. If the Au-rich phase becomes more ordered, the Pt-rich phase gets remarkably twinned. Probably it is because of the difference in the mobility of gold and platinum atoms. At 250°C, gold atoms were mobile enough to initiate the phase separation, while platinum atoms were not. Therefore, migration of Au atoms (from the common mixed structure) created defects/vacancies in the just-formed Pt-rich phase. Since the metal ratio was Au 55 to Pt 45, the density of the created defects exceeded the critical value causing vacancy driven twinning. Interestingly, the number of domains returned to the average value only when Pt atoms became mobile (at ~ 400°C).

The current thesis focused on morphological and structural evolution in mono- and bimetallic FCC nanoparticles. It was shown how MDXRD method allows the discovery of structural details and their changes that were not accessible before. Analysis of the temperature-induced evolution of Au and AuPt particles showed how one could change the morphology of NPs. In a broad sense, a multidomain approach is a promising tool for unraveling the correlations between a number of domains and catalytic, electronic, and optical properties of NPs.

5 List of abbreviations

NP	–	nanoparticle
CUB	–	cuboctahedron
DEC	–	decahedron
ICO	–	icosahedron
FCC	–	face-centered cubic
HCP	–	hexagonal close-packed
W-H	–	Williamson - Hall analysis
VAC	–	vacancies
Num.dom.	–	number of domains
MD	–	molecular dynamic
TEM	–	transmission electron microscopy
XRD	–	X-ray diffraction
FWHM	–	full width at half maximum
XRF	–	X-ray Fluorescence Spectroscopy
RT	–	room temperature
MDXRD	–	multidomain XRD
SAXS	–	small angle scattering
WAXS	–	wide angle scattering
CNA	–	common neighbor analysis
PVP	–	polyvinylpyrrolidone
ODA	–	octadecylamine
l.c.	–	lattice constant
EDX	–	energy dispersive X-ray spectroscopy

Special crystallographic notations:

hkl	–	indication of diffraction peaks
(hkl)	–	indication of crystallographic planes
[hkl]	–	indication of crystallographic directions

Other remarks:

Structure	–	this term refers to the arrangement of atoms in bimetallic samples (alloy; core-shell; Janus)
Morphology	–	this term refers to the stacking of atoms in the bulk (e.g. CUB, DEC, ICO, multiply twinned / multidomain particles)
Phase separation	–	structural evolution leading to formation of Janus particles
Phase segregation	–	structural evolution leading to formation of Core-shell particles

6 References

- 1 Szunerits, S., and R. Boukherroub. "Near-infrared photothermal heating with gold nanostructures." (2018): 500-510.
- 2 Faraday, M. "The Baker Lecture: Experimental of Gold (and other metals) to light." *Philosophical Transactions of Royal Society of London* 147 (1857): 147-181.
- 3 Huang, Daniel, et al. "Plastic-compatible low resistance printable gold nanoparticle conductors for flexible electronics." *Journal of the electrochemical society* 150.7 (2003): G412.
- 4 Calavia, Paula García, et al. "Photosensitiser-gold nanoparticle conjugates for photodynamic therapy of cancer." *Photochemical & Photobiological Sciences* 17.11 (2018): 1534-1552.
- 5 Ghosh, Partha, et al. "Gold nanoparticles in delivery applications." *Advanced drug delivery reviews* 60.11 (2008): 1307-1315.
- 6 Priyadarshini, E., and Nilotpala Pradhan. "Gold nanoparticles as efficient sensors in colorimetric detection of toxic metal ions: a review." *Sensors and Actuators B: Chemical* 238 (2017): 888-902.
- 7 Wang, Chao, and Chenxu Yu. "Detection of chemical pollutants in water using gold nanoparticles as sensors: a review." *Reviews in Analytical Chemistry* 32.1 (2013): 1-14.
- 8 Tong, Ling, et al. "Gold nanorods as contrast agents for biological imaging: optical properties, surface conjugation and photothermal effects." *Photochemistry and photobiology* 85.1 (2009): 21-32.
- 9 Wang, Jianling, et al. "In vivo self-bio-imaging of tumors through in situ biosynthesized fluorescent gold nanoclusters." *Scientific reports* 3.1 (2013): 1157.
- 10 Zhou, Wen, et al. "Gold nanoparticles for in vitro diagnostics." *Chemical reviews* 115.19 (2015): 10575-10636.
- 11 Wilson, Robert. "The use of gold nanoparticles in diagnostics and detection." *Chemical Society Reviews* 37.9 (2008): 2028-2045.
- 12 Grisel, Ruud, et al. "Catalysis by gold nanoparticles." *Gold Bulletin* 35 (2002): 39-45.
- 13 Priece, Peter, et al. "Anisotropic gold nanoparticles: Preparation and applications in catalysis." *Chinese Journal of Catalysis* 37.10 (2016): 1619-1650.
- 14 Zhao, Yuyun, et al. "Tuning the composition of AuPt bimetallic nanoparticles for antibacterial application." *Angewandte Chemie International Edition* 53.31 (2014): 8127-8131.
- 15 Xiao, Fei, et al. "Ultrasonic electrodeposition of gold-platinum alloy nanoparticles on ionic liquid-chitosan composite film and their application in fabricating nonenzyme hydrogen peroxide sensors." *The Journal of Physical Chemistry C* 113.3 (2009): 849-855.

-
- 16 Shi, Y. C., Feng, J. J., Chen, S. S., Tu, G. M., Chen, J. R., & Wang, A. J. (2017). Simple synthesis of hierarchical AuPt alloy nanochains for construction of highly sensitive hydrazine and nitrite sensors. *Materials Science and Engineering: C*, 75, 1317-1325.
- 17 Zhong, Chuan-Jian, et al. "Fuel cell technology: nano-engineered multimetallic catalysts." *Energy & Environmental Science* 1.4 (2008): 454-466.
- 18 Jusys, Zenonas, and R. Jürgen Behm. "Borohydride electrooxidation over Pt/C, AuPt/C and Au/C catalysts: Partial reaction pathways and mixed potential formation." *Electrochemistry Communications* 60 (2015): 9-12.
- 19 Wang, Jiangwei, et al. "Size-dependent dislocation–twin interactions." *Nanoscale* 11.26 (2019): 12672-12679.
- 20 Kim, Jong Woo, et al. "3D Bragg coherent diffractive imaging of five-fold multiply twinned gold nanoparticle." *Nanoscale* 9.35 (2017): 13153-13158.
- 21 Carnis, Jérôme, et al. "Twin boundary migration in an individual platinum nanocrystal during catalytic CO oxidation." *Nature communications* 12.1 (2021): 5385.
- 22 Dupraz, Maxime, et al. "Imaging the facet surface strain state of supported multi-faceted Pt nanoparticles during reaction." *Nature Communications* 13.1 (2022): 3003.
- 23 Kim, Dongjin, et al. "Active site localization of methane oxidation on Pt nanocrystals." *Nature communications* 9.1 (2018): 3422.
- 24 Kaszkur, Zbigniew, and Ilia Smirnov. "Nanopowder Diffraction." *arXiv preprint arXiv:2212.06926* (2022).
- 25 Qian, Xiaohu, and Harold S. Park. "The influence of mechanical strain on the optical properties of spherical gold nanoparticles." *Journal of the Mechanics and Physics of Solids* 58.3 (2010): 330-345.
- 26 Nelli, Diana, Cesare Roncaglia, and Chloé Minnai. "Strain engineering in alloy nanoparticles." *Advances in Physics: X* 8.1 (2023): 2127330.
- 27 Wang, Lihua, et al. "New twinning route in face-centered cubic nanocrystalline metals." *Nature communications* 8.1 (2017): 2142.
- 28 Chen, Chien-Chun, et al. "Three-dimensional imaging of dislocations in a nanoparticle at atomic resolution." *Nature* 496.7443 (2013): 74-77.
- 29 Kim, Byung Hyo, et al. "Critical differences in 3D atomic structure of individual ligand-protected nanocrystals in solution." *Science* 368.6486 (2020): 60-67.
- 30 , Jong Min, et al. "In situ atomic imaging of coalescence of Au nanoparticles on graphene: rotation and grain boundary migration." *Chemical Communications* 49.98 (2013): 11479-11481.
- 31 Song, Miao, et al. "Oriented attachment induces fivefold twins by forming and decomposing high-energy grain boundaries." *Science* 367.6473 (2020): 40-45

-
- 32 Foster, D. M., R. Ferrando, and R. E. Palmer. "Experimental determination of the energy difference between competing isomers of deposited, size-selected gold nanoclusters." *Nature communications* 9.1 (2018): 1323.
- 33 Wells, Dawn M., et al. "Metastability of the atomic structures of size-selected gold nanoparticles." *Nanoscale* 7.15 (2015): 6498-6503.
- 34 Smirnov, Ilia, Zbigniew Antoni Kaszkur, and Armin Hoell. "Development of nanoparticles bulk morphology analysis: Multidomain XRD approach." *Nanoscale* (2023)
- 35 Gnutzmann, V., and Walter Vogel. "Structural sensitivity of the standard platinum/silica catalyst EuroPt-1 to hydrogen and oxygen exposure by in situ X-ray diffraction." *Journal of Physical Chemistry* 94.12 (1990): 4991-4997
- 36 Grammatikopoulos, Panagiotis, et al. "Coalescence-induced crystallisation wave in Pd nanoparticles." *Scientific reports* 4.1 (2014): 1-9
- 37 Lange, A. P., et al. "Dislocation mediated alignment during metal nanoparticle coalescence." *Acta Materialia* 120 (2016): 364-378.
- 38 Roncaglia, Cesare, et al. "Growth mechanisms from tetrahedral seeds to multiply twinned Au nanoparticles revealed by atomistic simulations." *Nanoscale Horizons* 7.8 (2022): 883-889.
- 39 Simmons, R. O., and R. W. Balluffi. "Measurements of equilibrium vacancy concentrations in aluminum." *Physical Review* 117.1 (1960): 52.
- 40 Huang, Xiao, et al. "Synthesis of hexagonal close-packed gold nanostructures." *Nature communications* 2.1 (2011): 1-6
- 41 Wanjala, Bridgid Nekesa, et al. "Gold-platinum nanoparticles: alloying and phase segregation." *Journal of Materials Chemistry* 21.12 (2011): 4012-4020
- 42 Huang, Rao, et al. "Insight into c of Au–Pt core–shell nanoparticles from atomistic simulations." *The Journal of Physical Chemistry C* 117.8 (2013): 4278-4286.
- 43 Deng, Lei, et al. "Surface segregation and structural features of bimetallic Au– Pt nanoparticles." *The Journal of Physical Chemistry C* 114.25 (2010): 11026-11032.
- 44 Wanjala, Bridgid N., et al. "Nanoscale alloying, phase-segregation, and core– shell evolution of gold– platinum nanoparticles and their electrocatalytic effect on oxygen reduction reaction." *Chemistry of Materials* 22.14 (2010): 4282-4294.
- 45 Suntivich, Jin, et al. "Surface composition tuning of Au–Pt bimetallic nanoparticles for enhanced carbon monoxide and methanol electro-oxidation." *Journal of the American Chemical Society* 135.21 (2013): 7985-7991.
- 46 Liao, Hanbin, Adrian Fisher, and Zhichuan J. Xu. "Surface segregation in bimetallic nanoparticles: a critical issue in electrocatalyst engineering." *Small* 11.27 (2015): 3221-3246.
- 47 Liu, H. B., U. Pal, and J. A. Ascencio. "Thermodynamic stability and melting mechanism of bimetallic Au– Pt nanoparticles." *The Journal of Physical Chemistry C* 112.49 (2008): 19173-19177.

-
- 48 Wang, Yuexia, and Marc Hou. "Ordering of bimetallic nanoalloys predicted from bulk alloy phase diagrams." *The Journal of Physical Chemistry C* 116.19 (2012): 10814-10818.
- 49 Van Hardeveld, R., and F. Hartog. "The statistics of surface atoms and surface sites on metal crystals." *Surface Science* 15.2 (1969): 189-230.
- 50 Teo, Boon K., and N. J. A. Sloane. "Magic numbers in polygonal and polyhedral clusters." *Inorganic Chemistry* 24.26 (1985): 4545-4558.
- 51 Cleveland, Charles L., et al. "Structural evolution of smaller gold nanocrystals: The truncated decahedral motif." *Physical review letters* 79.10 (1997): 1873
- 52 Marks, L. D. "Surface structure and energetics of multiply twinned particles." *Philosophical Magazine A* 49.1 (1984): 81-93.
- 53 Esparza, R., et al. "Structural analysis and shape-dependent catalytic activity of Au, Pt and Au/Pt nanoparticles." *Matéria (Rio de Janeiro)* 13 (2008): 579-586.
- 54 Ji, Wenhai, et al. "Synthesis of Marks-Decahedral Pd Nanoparticles in Aqueous Solutions." *Particle & Particle Systems Characterization* 31.8 (2014): 851-856.
- 55 Azcárate, Julio C., Mariano H. Fonticelli, and Eugenia Zelaya. "Radiation damage mechanisms of monolayer-protected nanoparticles via TEM analysis." *The Journal of Physical Chemistry C* 121.46 (2017): 26108-26116.
- 56 Besley, Nicholas A., et al. "Theoretical study of the structures and stabilities of iron clusters." *Journal of Molecular Structure: THEOCHEM* 341.1-3 (1995): 75-90.
- 57 Hendy, Shaun C., and Jonathan PK Doye. "Surface-reconstructed icosahedral structures for lead clusters." *Physical Review B* 66.23 (2002): 235402.
- 58 Sutton, A. P., and J. Chen. "Long-range finnis–sinclair potentials." *Philosophical Magazine Letters* 61.3 (1990): 139-146.
- 59 Mierzwa, B., and Z. Kaszukur. "Proceedings of the XIX Conference on Applied Crystallography, edited by H. Morawiec & D. Stróż." (2004): 162-166.
- 60 Stukowski, Alexander. "Visualization and analysis of atomistic simulation data with OVITO—the Open Visualization Tool." *Modelling and simulation in materials science and engineering* 18.1 (2009): 015012
- 61 Nilsson Pingel, Torben, et al. "Influence of atomic site-specific strain on catalytic activity of supported nanoparticles." *Nature communications* 9.1 (2018): 2722.
- 62 Madsen, Jacob, et al. "Accuracy of surface strain measurements from transmission electron microscopy images of nanoparticles." *Advanced structural and chemical imaging* 3.1 (2017): 1-12.
- 63 B. E. Warren *X-Ray Diffraction*, Addison-Wesley, Reading, MA, 1969,
- 64 Longo, Alessandro, and Antonino Martorana. "Distorted fcc arrangement of gold nanoclusters: a model of spherical particles with microstrains and stacking faults." *Journal of Applied Crystallography* 41.2 (2008): 446-455;

-
- 65 Simmons, R. O., and R. W. Balluffi. "Measurement of the equilibrium concentration of lattice vacancies in silver near the melting point." *Physical Review* 119.2 (1960): 600.
- 66 Simmons, R. O., and R. W. Balluffi. "Measurement of equilibrium concentrations of lattice vacancies in gold." *Physical Review* 125.3 (1962): 862.
- 67 Simmons, R. O., and R. W. Balluffi. "Measurement of equilibrium concentrations of vacancies in copper." *Physical Review* 129.4 (1963): 1533.
- 68 Boer, F. R., Boom, R., Mattens, W. C. M., Miedema, A. R., & Niessen, A. K. (1988). *Cohesion in metals: transition metal alloys* (Vol. 1). North Holland.
- 69 Okamoto, H., and T. B. Massalski. "The Au–Pt (Gold-Platinum) system." *Bulletin of Alloy Phase Diagrams* 6.1 (1985): 46-56.
- 70 Qi, W. H., and M. P. Wang. "Size effect on the cohesive energy of nanoparticle." *Journal of Materials Science Letters* 21 (2002): 1743-1745.
- 71 Xiao, S., et al. "Size effect on alloying ability and phase stability of immiscible bimetallic nanoparticles." *The European Physical Journal B-Condensed Matter and Complex Systems* 54.4 (2006): 479-484
- 72 Luo, Jin, et al. "Phase properties of carbon-supported gold– platinum nanoparticles with different bimetallic compositions." *Chemistry of materials* 17.12 (2005): 3086-3091
- 73 Petkov, Valeri, et al. "Pt–Au alloying at the nanoscale." *Nano letters* 12.8 (2012): 4289-4299.
- 74 Ferrando, Riccardo. "Symmetry breaking and morphological instabilities in core-shell metallic nanoparticles." *Journal of Physics: Condensed Matter* 27.1 (2014): 013003.
- 75 Laasonen, Kari, et al. "Competition between icosahedral motifs in AgCu, AgNi, and AgCo nanoalloys: a combined atomistic–DFT study." *The Journal of Physical Chemistry C* 117.49 (2013): 26405-26413.
- 76 Langlois, Cyril, et al. "Transition from core–shell to Janus chemical configuration for bimetallic nanoparticles." *Nanoscale* 4.11 (2012): 3381-3388.
- 77 Langlois, Cyril T., et al. "Energy-filtered electron microscopy for imaging core–shell nanostructures." *Journal of Nanoparticle Research* 10 (2008): 997-1007.
- 78 Snellman, Markus, et al. "Continuous gas-phase synthesis of core–shell nanoparticles via surface segregation." *Nanoscale Advances* 3.11 (2021): 3041-3052.
- 79 Parsina, I., and F. Baletto. "Tailoring the structural motif of AgCo nanoalloys: core/shell versus Janus-like." *The Journal of Physical Chemistry C* 114.3 (2010): 1504-1511.
- 80 Paul, Aloke, et al. *Thermodynamics, diffusion and the Kirkendall effect in solids*. Cham: Springer International Publishing, 2014.
- 81 Huntington, H. B., and Frederick Seitz. "Mechanism for self-diffusion in metallic copper." *Physical Review* 61.5-6 (1942): 315.

-
- 82 Kaszukur, Zbigniew, Wojciech Juszczyk, and Dariusz Łomot. "Self-diffusion in nanocrystalline alloys." *Physical Chemistry Chemical Physics* 17.42 (2015): 28250-28255.
- 83 Laue, M. von. "Eine quantitative Prüfung der Theorie für die Interferenzerscheinungen bei Röntgenstrahlen." *Annalen der Physik* 346.10 (1913): 989-1002.
- 84 Friedrich, Walter, Paul Knipping, and Max Laue. "Interferenzerscheinungen bei roentgenstrahlen." *Annalen der Physik* 346.10 (1913): 971-988.
- 85 Bragg, P. W. H. "Bragg WL Proc. R." *Soc. London. Ser. A, Contain. Pap. a Math. Phys. Character* 17 (1913): 428.
- 86 Scherrer, Paul. "Bestimmung der Grösse und der inneren Struktur von Kolloidteilchen mittels Röntgenstrahlen." *Nachrichten von der Gesellschaft der Wissenschaften zu Göttingen, mathematisch-physikalische Klasse* 1918 (1918): 98-100.
- 87 Lanson, Bruno, and Bernard Kubler. "Experimental determinations of the coherent scattering domain size distribution of natural mica-like phases with the Warren-Averbach technique." *Clays and Clay Minerals* 42 (1994): 489-494.
- 88 Ungár, Tamás, et al. "Correlation between subgrains and coherently scattering domains." *Powder Diffraction* 20.4 (2005): 366-375.
- 89 Vegard, Lars. "Die konstitution der mischkristalle und die raumfüllung der atome." *Zeitschrift für Physik* 5.1 (1921): 17-26.
- 90 Krishnamurti, Studies in X-Ray Diffraction. Part I: The Structure of Amorphous Scattering. Part II: Colioidal Solutions and Liquid Mixtures, *Indian J. Phys.*, **1930**, 5, 473-500
- 91 Warren, X-Ray Diffraction Study of Carbon Black, *J. Chem. Phys.*, **1934**, 2, 551-555
- 92 A. Guinier. La diraction des rayons x aux très faibles angles: applications à l'étude des phénomènes ultra-microscopiques. *Ann Phys (Paris)*, 12:161236, 1939
- 93 Ruska, Ernst, and Max Knoll. "Die magnetische Sammelspule für schnelle Elektronenstrahlen." *The magnetic concentrating coil for fast electron beams.) Z. techn. Physik* 12 (1931): 389-400.
- 94 Daw, Murray S., and Michael I. Baskes. "Semiempirical, quantum mechanical calculation of hydrogen embrittlement in metals." *Physical review letters* 50.17 (1983): 1285.
- 95 Gupta, Raju P. "Lattice relaxation at a metal surface." *Physical Review B* 23.12 (1981): 6265.
- 96 Rosato, Vittorio, M. Guillope, and B. Legrand. "Thermodynamical and structural properties of fcc transition metals using a simple tight-binding model." *Philosophical Magazine A* 59.2 (1989): 321-336.
- 97 Debye, Peter. "Zerstreuung von röntgenstrahlen." *Annalen der Physik* 351.6 (1915): 809-823.

-
- 98 Tsunoyama, Hironori, Nobuyuki Ichikuni, and Tatsuya Tsukuda. "Microfluidic synthesis and catalytic application of PVP-stabilized, ~ 1 nm gold clusters." *Langmuir* 24.20 (2008): 11327-11330;
- 99 El Amri, Nouha, and Kevin Roger. "Polyvinylpyrrolidone (PVP) impurities drastically impact the outcome of nanoparticle syntheses." *Journal of Colloid and Interface Science* 576 (2020): 435-443;
- 100 Dahlberg, Kevin A., and Johannes W. Schwank. "Synthesis of Ni@ SiO₂ nanotube particles in a water-in-oil microemulsion template." *Chemistry of Materials* 24.14 (2012): 2635-2644;
- 101 Zhang, Haijun, and Naoki Toshima. "Synthesis of Au/Pt bimetallic nanoparticles with a Pt-rich shell and their high catalytic activities for aerobic glucose oxidation." *Journal of colloid and interface science* 394 (2013): 166-176;
- 102 Zhang, Haijun, Jun Okuni, and Naoki Toshima. "One-pot synthesis of Ag–Au bimetallic nanoparticles with Au shell and their high catalytic activity for aerobic glucose oxidation." *Journal of colloid and interface science* 354.1 (2011): 131-138;
- 103 J. Turkevich, P. C. Stevenson, J. Hillier, *Disc. Farad. Soc.*, vol. 11, p. 55, 1951
- 104 K. C. Grabar, K. J. Allison, B. E. Barker, R. M. Bright, K. R. Brown, R. G. Freeman, A. P. Fox, C. D. Keating, M. D. Musick, M. J. Natan, *Langmuir*, vol. 12, no. 10, p. 2353, 1996
- 105 Chen, X. Y., J. R. Li, and Long Jiang. "Two-dimensional arrangement of octadecylamine-functionalized gold nanoparticles using the LB technique." *Nanotechnology* 11.2 (2000): 108.
- 106 Wojdyr, Marcin. "Fityk: a general-purpose peak fitting program." *Journal of Applied Crystallography* 43.5-1 (2010): 1126-1128.
- 107 Collins, Tony J. "ImageJ for microscopy." *Biotechniques* 43.S1 (2007): S25-S30.
- 108 Brynestad, Iron and Nickel Carbonyl Formation in Steel Pipes and Its Prevention - Literature survey, Oak Ridge, Tennessee, USA: National Technical Information Service, U.S. Department of Commerce, 1976.
- 109 Ackermann, R. J., and CHARLES A. Sorrell. "Thermal expansion and the high–low transformation in quartz. I. High-temperature X-ray studies." *Journal of Applied Crystallography* 7.5 (1974): 461-467.
- 110 Dutta, B. N., and B. Dayal. "Lattice Constants and Thermal Expansion of Gold up to 878° C by X-Ray Method." *physica status solidi (b)* 3.3 (1963): 473-477.
- 111 Arblaster, J. W. "Crystallographic properties of platinum." *Platinum Metals Review(UK)* 41.1 (1997): 12-21.
- 112 Breßler, Ingo, Joachim Kohlbrecher, and Andreas F. Thünemann. "SASfit: a tool for small-angle scattering data analysis using a library of analytical expressions." *Journal of applied crystallography* 48.5 (2015): 1587-1598.
- 113 Vogel, Walter, B. Rosner, and B. Tesche. "Structural investigations of gold (Au₅₅) organometallic complexes by x-ray powder diffraction and transmission electron microscopy." *The Journal of Physical Chemistry* 97.45 (1993): 11611-11616.

-
- 114 Paterson, M. Sv. "X-ray diffraction by face-centered cubic crystals with deformation faults." *Journal of Applied Physics* 23.8 (1952): 805-811;
- 115 Warren, B. E., and E. P. Warekois. "Stacking faults in cold worked alpha-brass." *Acta metallurgica* 3.5 (1955): 473-479;
- 116 Velterop, L., et al. "X-ray diffraction analysis of stacking and twin faults in fcc metals: a revision and allowance for texture and non-uniform fault probabilities." *Journal of applied crystallography* 33.2 (2000): 296-306;
- 117 Johnson, Craig L., et al. "Effects of elastic anisotropy on strain distributions in decahedral gold nanoparticles." *Nature materials* 7.2 (2008): 120-124;
- 118 Ge, Mengke, et al. "Anomalous detwinning in constrained Cu nanoparticles." *Nanoscale* 12.27 (2020): 14831-1483;
- 119 Ferrando, Riccardo. "6 Kinetic aspects: nucleation, mixing." *Nanoalloys: From Fundamentals to Emergent Applications* (2013): 175;
- 120 Baletto, Francesca, and Riccardo Ferrando. "Structural properties of nanoclusters: Energetic, thermodynamic, and kinetic effects." *Reviews of modern physics* 77.1 (2005): 371.
- 121 Yuk, Jong Min, et al. "High-resolution EM of colloidal nanocrystal growth using graphene liquid cells." *Science* 336.6077 (2012): 61-64;
- 122 Liu, Pei, et al. "Reversible and concerted atom diffusion on supported gold nanoparticles." *Journal of Physics: Materials* 3.2 (2020): 024009;
- 123 Ingham, Bridget, et al. "How nanoparticles coalesce: an in situ study of Au nanoparticle aggregation and grain growth." *Chemistry of Materials* 23.14 (2011): 3312-3317;
- 124 Theissmann, R., et al. "Crystallographic reorientation and nanoparticle coalescence." *Physical Review B* 78.20 (2008): 20541;
- 125 Nelli, Diana, et al. "Structure and orientation effects in the coalescence of Au clusters." *Nanoscale* 12.14 (2020): 7688-7699;
- 126 Ma, Xiaoming, et al. "Unveiling growth pathways of multiply twinned gold nanoparticles by in situ liquid cell transmission electron microscopy." *ACS nano* 14.8 (2020): 9594-9604.
- 127 Xia, Yu, et al. "Shape control of size-selected naked platinum nanocrystals." *Nature communications* 12.1 (2021): 1-8;
- 128 Baletto, F., C. Mottet, and R. Ferrando. "Microscopic mechanisms of the growth of metastable silver icosahedra." *Physical Review B* 63.15 (2001): 155408;
- 129 Amodeo, Jonathan, Fabio Pietrucci, and Julien Lam. "Out-of-equilibrium polymorph selection in nanoparticle freezing." *The Journal of Physical Chemistry Letters* 11.19 (2020): 8060-8066;
- 130 Kaszkur, Zbigniew. "Nanopowder diffraction analysis beyond the Bragg law applied to palladium." *Journal of applied crystallography* 33.1 (2000): 87-94.

-
- 131 Young, N. P., et al. "Transformations of gold nanoparticles investigated using variable temperature high-resolution transmission electron microscopy." *Ultramicroscopy* 110.5 (2010): 506-516;
- 132 Bourgoin, J. C., and J. W. Corbett. "Enhanced diffusion mechanisms." *Radiation Effects* 36.3-4 (1978): 157-188;
- 133 Marks, Laurence D. "Experimental studies of small particle structures." *Reports on progress in physics* 57.6 (1994): 603;
- 134 Mei, Q. S., and K. Lu. "Melting of metals: role of concentration and migration of vacancies at surfaces." *Philosophical magazine letters* 88.3 (2008): 203-211.
- 135 Mei, Q. S., and K. Lu. "Melting and superheating of crystalline solids: From bulk to nanocrystals." *Progress in Materials Science* 52.8 (2007): 1175-1262.
- 136 Görecki, Tadeusz. "Vacancies and changes of physical properties of metals at the melting point." *International Journal of Materials Research* 65.6 (1974): 426-431;
- 137 Bras, Wim, and Halina Stanley. "Unexpected effects in non crystalline materials exposed to X-ray radiation." *Journal of Non-Crystalline Solids* 451 (2016): 153-160.
- 138 Nelli, Diana, and Riccardo Ferrando. "Core-shell vs. multi-shell formation in nanoalloy evolution from disordered configurations." *Nanoscale* 11.27 (2019): 13040-13050.
- 139 Braidy, Nadi, Gary R. Purdy, and Gianluigi A. Botton. "Equilibrium and stability of phase-separating Au-Pt nanoparticles." *Acta Materialia* 56.20 (2008): 5972-5983.
- 140 Peng, Lingxuan, et al. "Segregation in bimetallic nanoparticles." *Physical Chemistry Chemical Physics* 17.42 (2015): 27940-27951.
- 141 Pedrosa, Maria Clara Guimarães, et al. "Chemical surface modification and characterization of carbon nanostructures without shape damage." *Materials Research* 23 (2020).
- 142 Kharchenko, D. O., V. O. Kharchenko, and A. I. Bashtova. "Self-organization of an ensemble of vacancies under the spinodal decomposition of binary systems at continuous irradiation." *Ukrainian Journal of Physics* 61.3 (2016): 265-265.